

**Design, characterization, and implementation of lightweight and
energy-efficient electroadhesive clutches for robotics**

Submitted in partial fulfillment of the requirements for
the degree of
Doctor of Philosophy
in
Mechanical Engineering

Stuart B. Diller

B.S., Mechanical Engineering, University of Virginia

M.S., Mechanical Engineering, Carnegie Mellon University

Carnegie Mellon University
Pittsburgh, PA
December, 2018

© Stuart B. Diller 2018.

All Rights Reserved

Acknowledgements

Thank you Carmel and Steve for guiding me through the past 5 years. I'm so grateful for your insights, guidance, and encouragement, and for pushing me to achieve great results.

Thanks to Sarah, Ralph, and Doug for your input as members of my committee, and for helping to guide my work in impactful directions.

Thank you to Dr. Robinson, Chris, Bobbi, Ginny, Li, Jon, Ed, Jim, Larry, Ryan, Diana, and the rest of the MechE administration and staff for your professionalism and effort, which propelled my work forward.

Thank you to my collaborator Erez Krinsky for your dedicated work on the electronics design and implementation for the energy recycling actuator.

Thanks to Bugra, Andy, James, Lauren, Mike, Mo, Wanliang, Tong, Sean, Chengfeng, Tess, Yun, Terri, Zisheng, Eric, Steven, Navid, Vivek, Loren, Hesham, Jiahe, and all the other past and current members of SML for all of your help and good humor.

Thanks to Kirby, Josh, Rachel, JJ, Myunghee, Pieter, Evan, James, Kyle, Mailing, Philippe, Katie, Vince, Patrick, Gwen, Stefan, Thu, Rong, Erez, and all the past and current members of EBL for your camaraderie.

Thank you to Emily, Christiana, Jacob, Kyle, Brendan, Phil, Betty, Alastair, Elena, Mark, and the other past and current members of the Pittsburgh Compline Choir for your friendship and great music.

Thanks to Jeff, Will, Abs, Jen, Matt, Amanda, Evan, Kristen, Nate, Nathan, Christina, Cesar, Dave, Mike, Chris, Kristin, and other the Upper Roomers for supporting and sticking with me.

Thanks to Liz, Derick, Jude, the Florians, the Veys, and the rest of my family in Pittsburgh for welcoming and caring for me.

Thanks to Nate and Peter for encouraging my engineering thinking.

My sincerest thanks to Mom and Dad for all of your support and love.

Doctoral committee:

Dr. Carmel Majidi (co-chair), *Carnegie Mellon University*

Dr. Steven Collins (co-chair), *Stanford University*

Dr. Sarah Bergbreiter, *Carnegie Mellon University*

Dr. Ralph Hollis, *Carnegie Mellon University*

Dr. Douglas Weber, *University of Pittsburgh*

Funding Sources:

I would like to acknowledge and thank my funding sources: Carnegie Mellon University Department of Mechanical Engineering, Nike Inc., the National Science Foundation under grant no. CMMI 1355716, the John and Clair Bertucci Graduate Fellowship, and the Carnegie Mellon University Innovation Fellowship.

Abstract

Despite decades of academic and industry effort, achieving efficient and dynamic movement of robots remains a significant challenge. Many robots, particularly humanoid robots and wearable robots such as exoskeletons and prostheses, are quite limited in their versatility and usefulness because of the force and speed limitations of actuators. Weight and power consumption are particularly important factors in determining the operating range and effectiveness of these devices. Geared electric motors are most commonly used in these applications, but often result in slow, stiff, and halting operation. Other options include hydraulic actuators, pneumatic actuators, electroactive polymer actuators, and shape memory materials, but none of these are able to achieve the combination of high power output, high efficiency, and low weight that would enable dynamic movement of untethered robots.

Many proposed solutions to this problem involve using clutches to improve the efficiency and capability of actuation systems. However, conventional clutches such as electromagnetic and magnetorheological clutches are themselves too heavy and power-hungry to be practical. This thesis presents an electroadhesive clutch that has $10\times$ lower weight and $1000\times$ lower power consumption than conventional clutches. To inform a variety of possible implementations, I extensively characterized the effects of design choices on the holding force, responsiveness, and power consumption of the electroadhesive clutch. Next, I investigated the use of the clutch in a walking assistance exoskeleton, demonstrating the reliability and advantages of the electroadhesive clutch in a challenging robotics application. Finally, I studied the use of electroadhesive clutches to harvest, store, and return mechanical energy with rubber springs, and used multiple of these units in parallel to create a force controllable energy recycling actuator. My aspiration is that the work in this dissertation will lead to improved robotic hardware that enables exciting new capabilities in next generation robotics.

Contents

Acknowledgments	iii
Abstract	v
1 Introduction	1
1.1 Motivation	1
1.2 Actuators for Robotics	2
1.3 Clutches for Improved Actuator Efficiency and Versatility	3
1.4 Previous Electroadhesive Devices	4
1.5 Electroadhesive Clutch Design and Operating Principle	5
1.6 Problem Statement	6
1.7 Thesis Outline	7
2 Effects of electroadhesive clutch design on performance	8
2.1 Introduction	9
2.1.1 Experimental Design	11
2.1.2 Theoretical Model	12
2.2 Fabrication	13
2.3 Experimental Characterization	15
2.3.1 Holding Force	15
2.3.2 Release Time	21

2.3.3	Engage Time	25
2.3.4	Power Consumption	30
2.3.5	Fatigue Life	33
2.4	Data Analysis	35
2.4.1	ANOVA and Linear Regression Fitting	35
2.5	Discussion	39
2.5.1	Optimal Design Values	39
2.5.2	Comparison of the Empirical Model to Classic Electrostatic Theory . .	39
2.5.3	Design Example	42
2.5.4	Applications	45
2.5.5	Future Work	49
2.6	Conclusions	50
3	An electroadhesive clutch and spring for exoskeleton actuation	51
3.1	Motivation	52
3.2	Methods	53
3.3	Results	54
3.4	Discussion	55
3.5	Conclusions	57
4	Design, Control, and Characterization of Energy Recycling Actuator	58
4.1	Introduction	59
4.2	Double-Clutched Spring Characterization	60
4.2.1	Introduction	60
4.2.2	Methods	63
4.2.3	Inefficiency Model Derivation	65
4.2.4	Results	67
4.2.5	Discussion	69

4.3	Energy Recycling Actuator Design Optimization	70
4.3.1	Introduction	70
4.3.2	Methods	71
4.3.3	Results and Discussion	75
4.4	Controller Optimization in Simulation using CMAES	76
4.4.1	Introduction	76
4.4.2	Methods	76
4.4.3	Results	78
4.4.4	Discussion	81
4.5	Actuator Characterization	82
4.5.1	Introduction	82
4.5.2	Methods	82
4.5.3	Results	87
4.5.4	Discussion	88
4.5.5	Future Work	90
5	Conclusions and Future Work	91
A	Appendix	93
A.1	Control Circuits	93
A.2	Fatigue Testing Control	94
A.3	Coefficient of Friction Testing	95
A.4	Custom Circuit Board Layout	96

List of Tables

2.1	Recorded Parameter Statistical Significance.	35
2.2	Fitted Holding Force Model Coefficients	37
4.1	Output Values of Actuator Design Optimization	75
4.2	Mass of Energy Recycling Actuator Components	87

List of Figures

1.1	Types of Clutches	4
1.2	Electroadhesive Clutch Components	6
2.1	Actuator Configurations Using Clutches.	10
2.2	Comparison of Clutch Mass and Power Consumption	11
2.3	Maximum Holding Force Profile	16
2.4	Maximum Holding Force Results	17
2.5	Clutch Holding Force as a Funtion of Time	18
2.6	Environmental Scanning Electron Microscope Images	19
2.7	Release Time Test Force Profile	22
2.8	Release Time Results	23
2.9	Release Time and Holding Force	24
2.10	Engage Time Test Force Profile	27
2.11	Engage Time Results	28
2.12	Clutch Discharge Profile	31
2.13	Power Consumption Results	32
2.14	Fatigue Testing Results	34
2.15	Maximum Holding Force Empirical Models	36
2.16	Normalized Emperical Model Results	38
2.17	Design Flowchart for Electroadhesive Clutch Implementation	42
2.18	Clutch Length Diagram	42

3.1	Clutched Spring and Exoskeleton Components and Construction	53
3.2	Clutched Springs in Parallel	54
3.3	Ankle Angle, Measured Torque, and Exoskeleton Power During the Gait Cycle	55
4.1	Double-Clutched Spring Operation	61
4.2	Force Control with Double-Clutched Springs in Parallel	62
4.3	Handoff Inefficiency Characterization Methods	63
4.4	Inefficiency Model Boundary Conditions Diagram	65
4.5	Quasi-static Full Cycle Efficiency	68
4.6	Full Cycle Efficiency as a Function of Handoff Overlap Time	68
4.7	Model of Handoff Displacement Inefficiency	69
4.8	1-DOF Robot Arm Schematic	71
4.9	Parameter Schematic and Heuristic Illustration	72
4.10	CMAES Optimized Low-Level Control Terms in Simulation	79
4.11	CMAES Controller Performance Improvement	80
4.12	Diagram of Double Clutched Spring Construction	83
4.13	Energy Recycling Actuator Construction	84
4.14	Electronics and Control Hardware for Energy Recycling Actuator	85
4.15	Stretchy Fabric Sensor Calibration	86
4.16	Energy Recycling Actuator Force Tracking	88
A.1	Circuit Diagrams	93
A.2	Coefficient of Friction Testing	96
A.3	Custom High Voltage Control Circuit Schematics	97

Chapter 1

Introduction

1.1 Motivation

Human-safe mobile robots could have great usefulness in human environments by performing tasks such as delivery and in-home care. Many challenges stand in the way of the realization of these robots, including sensing, controls, manipulation, and safe human-robot interaction [1, 2]. However, the challenge of simply moving the robot safely, dynamically, and efficiency is still an unsolved problem and central obstacle [3].

The actuators on a robot need to support the weight and inertia of the robot, while also performing mechanical work on external objects and its surroundings. When the on-board actuators and power supply make up a large percentage of the robot's mass, the frame mass and total robot mass must be sized up, and the robot becomes heavy, weak, and slow. Because of this problem, one of the central goals of actuator designers becomes achieving high output force and power relative to actuator mass energy consumption [4].

Creating actuation systems that are lightweight, efficient, and powerful is an important research goal that I and many other researchers are striving for. In the following sections, I will discuss previous efforts toward this goal.

1.2 Actuators for Robotics

Many kinds of actuators have been implemented in robotic systems. Conventional robot arms have relied primarily on geared electric motors and hydraulics [5, 6]. Geared motors have been effective for large industrial robot arms because they can produce high torque and instantaneous power output with good position control [7]. Because large industrial arms are fixed in place, they are not limited by factors such as high power consumption, the need to store energy on-board, or the need to safely interact with humans. This application is also very advantageous for hydraulic actuators, because the on-board mass can be very low when the compressor is located off-board. However, for lightweight and mobile applications, the high mass and power consumption of full conventional motor and hydraulic systems become much more problematic [8]. This has driven substantial research into other actuator strategies for human-scale mobile robots.

Pneumatic Artificial Muscles (PAMs) have been explored in wearable robots, mobile robots, and robotic end effectors [9, 10, 11]. The pneumatic muscle can be quite lightweight and produce large forces [12]. It also has inherent elasticity and backdrivability, which is advantageous in many cases, particularly during human interaction [13]. However, pneumatic muscles are driven by compressed air, requiring a heavy accompanying compressor and valve system [14]. Additionally, the actuation bandwidth of PAMs is quite low, and precise control is difficult to achieve [11, 13]. These factors have significantly hindered designers, and PAMs have been unable to show better performance than motors for most tasks.

Electroactive Polymer Actuators (EPAs) have similar performance as PAMs, but are activated electrically rather than pneumatically. They are composed of stacks of electrodes and thin polymer films, and operate by applying large voltages to the electrodes, causing electrostriction of the polymer layers. [15]. These actuators can be lightweight and efficient, but they have been unable to achieve forces and strokes high enough to use in most high-performance robotics applications [16, 17]. Hydraulically amplified dielectric elastomer ac-

tuators have shown exciting performance improvements, but still rely on large high voltage power supplies [18].

Shape memory actuators can be activated with a variety of mechanisms, including heat, water, light, and other chemical stimuli [19]. They can also achieve very high power to weight ratios [20]. Their main limitations are low activation bandwidth and difficulty achieving precise control. Most of these materials have cycle times in excess of 10s, and can have very large hysteresis and history-dependent properties [21]. As with the other approaches, this solution has not achieved performance that satisfies the requirements of most robotic applications.

1.3 Clutches for Improved Actuator Efficiency and Versatility

Rather than exploring fundamentally different actuation mechanisms, some researchers have focused on using variable transmissions, parallel springs, and series elastic elements to improve the performance and efficiency of existing actuators [26].

Clutched springs can offload substantial amounts of work from the actuator, decreasing its required size and power consumption [27, 28]. The simplest implementations have very limited behavior, but more complex systems can allow energy to be stored and even transmitted between multiple joints [29, 30]. Variable transmissions can help an actuator achieve a wider range of torque-displacement profiles [31]. Such implementations rely on linkages [32], electroactive polymers [33], conventional clutches, and other solutions that are highly configuration dependent or come with the same drawbacks (high weight, power, etc.) that these efforts are trying to mitigate in the actuators.

Benchmark tests and simulations have shown that significant savings are theoretically possible [34], but existing clutch technologies present their own challenges. Electromagnetic and magnetorheological clutches have only slightly lower mass and power consumption than

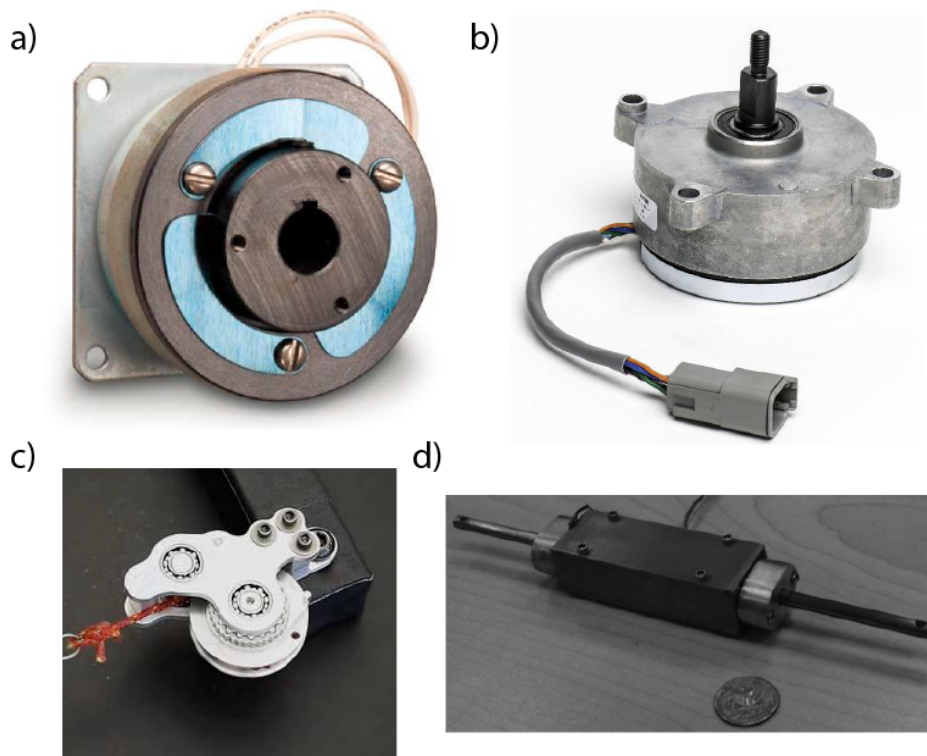


Figure 1.1: Types of Clutches. a) Electromagnetic clutch. b) Magneto-rheological clutch. c) Mechanical locking clutch. d) Linear Magneto-rheological clutch. Images reproduced from: a) Inertia Dynamics, [22] b) Lord, [23] c) Nature, [24] d) Sage, [25]

the actuators they are supposed to assist (Fig. 1.1a,b,d) [35, 27]. Pneumatic layer jamming devices and thermally activated shape change devices can achieve high forces [36, 37], but are hindered by high energy consumption and slow response. Mechanical locking clutches can be very light and consume no power, but are not electrically controllable (Fig. 1.1c) [24]. The lack of efficient, lightweight, and controllable clutches is the main obstacle to implementing these strategies in real-world use cases.

Given the great potential impact of creating a viable clutch technology for lightweight robotics, I focused my effort on creating a clutch that operates using electroadhesion.

1.4 Previous Electroadhesive Devices

Electroadhesive devices have many of the characteristics desired in a clutch for robotics. Very little material is needed to produce the effect, and the power consumption of the devices

is extremely low. Electrode adhesion has been used primarily in grippers and wall-climbing robots [38, 39]. These devices typically use comb-shaped electrodes to adhere to a variety of surfaces and operate using 1000s of volts [40]. However, very high adhesion has been demonstrated with continuous electrodes at voltages lower than 100 V [41].

A few previous attempts to create clutches using electroadhesion were successful in generating large forces with low device weight, but had limited success in implementation because of force hysteresis and slow control response times (~ 1 s) [42, 43]. These unwanted effects arose mainly because of the materials used and overall design of the devices. After investigating many materials candidates and iterating on my design, I created an electroadhesive clutch that embodies the high force and low power consumption of previous electroadhesive devices, while also achieving very fast response times and high reliability [44].

1.5 Electroadhesive Clutch Design and Operating Principle

The novel electroadhesive clutch I created is composed of two separate clutch plates (Fig. 1.2a-c). Each plate is an aluminum-sputtered polymer electrode coated with a high-dielectric insulator (Luxprint, Dupont). The plates are flexible, so the necessary structure and load distribution are achieved by attaching them to stiff carbon fiber bars with thin double-sided acrylic tape. The two clutch plates are oriented such that their dielectric layers are in contact, and small rubber bands serve as tensioners to maintain the correct configuration in any orientation. Applying a voltage across the electrodes causes opposite electric charges to accumulate on the electrode surfaces. As the charge increases, an electrostatic attraction develops at the interface and the plates adhere to one another. When the carbon fiber attachments of each clutch plate are pulled away from one another, the adhesion and friction at the interface of the clutch plates cause a shear force that resists relative motion. Dis-

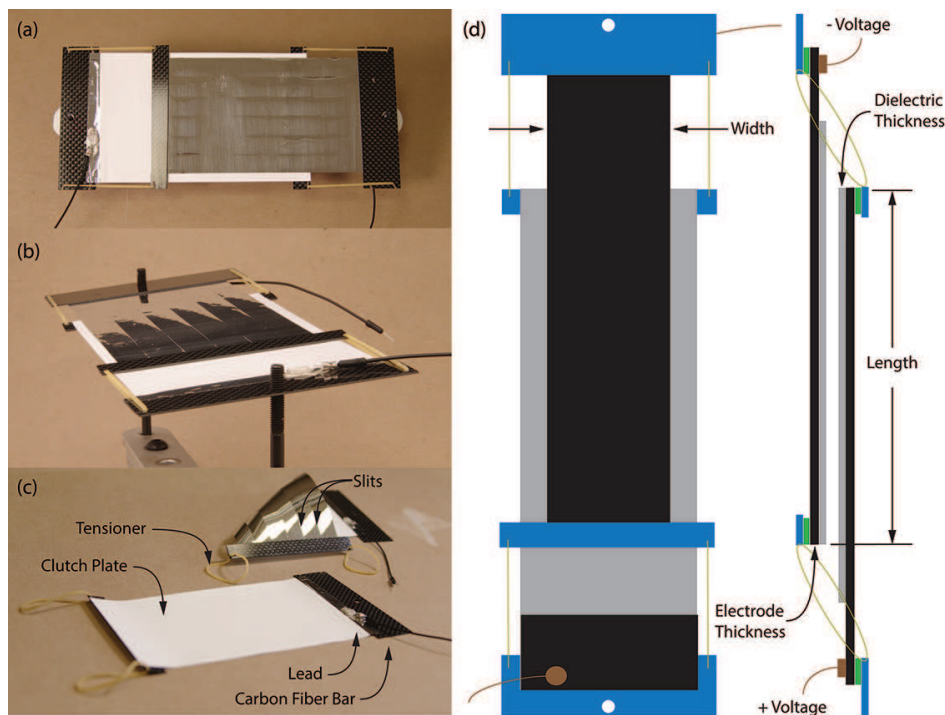


Figure 1.2: Electroadhesive Clutch. a-b) The clutch in its operating configuration. c) Clutch components. The clutch is composed of two clutch plates attached to carbon fiber bars, and held in place by small tensioners. d) Diagram of clutch parameters. In this study, the width, length, electrode thickness, dielectric thickness, and voltage are systematically varied.

charging the electrodes eliminates the electrostatic attraction at the interface of the clutch plates, allowing them to release and slide freely. This design embodies the high performance of electroadhesion in a reliable clutch architecture.

1.6 Problem Statement

Incorporating clutches and springs into an actuation system can increase the maximum power and force output while reducing overall energy consumption. However, existing clutches have relatively high mass and power consumption, which precludes their use in lightweight robots. As a result, many robots struggle to achieve their high-level performance goals because of the limits of their actuators.

My objectives in this thesis are to:

- Create new clutch hardware with sufficiently high force to weight and force to power

consumption ratios to enable the use of clutched actuators in lightweight mobile robots.

- Identify and characterize the most important performance metrics of the new clutch hardware to inform the design choices of potential clutch users.
- Evaluate the use of the new clutch hardware and control strategies to offload actuator work and recycle energy in robotic systems.

1.7 Thesis Outline

This thesis describes the approach I have taken to improving the performance and capabilities of robots using electroadhesive clutches. In Chapter 2, I present an experimental study of electroadhesive clutch holding force, responsiveness, and power consumption as a function of design decisions. I then compile this knowledge into a design guide that informs a broad range of future implementations. I also perform a fatigue life test that demonstrates effective long-term use. In Chapter 3, I describe the design and control of an ankle exoskeleton that uses an electroadhesive clutched spring to assist walking. In Chapter 4, I present a design and controls approach for high-efficiency energy recycling using electroadhesive double-clutched springs. I perform experiments to identify the best design and operating parameters of the clutch-spring units. Using this knowledge, I design and build an actuator that uses many clutch-spring units to controllably harvest and return energy. Finally, I show the efficacy of an optimization-based control strategy in simulation and preliminary experiments.

Chapter 2

The effects of electroadhesive clutch design parameters on performance characteristics

Abstract

Actuators that employ clutches can exhibit mechanical impedance tuning and improved energy efficiency. However, these integrated designs have been difficult to achieve in practice because conventional clutches are typically heavy and consume substantial power. In Chapter 2, I describe a lightweight and low-power clutch that operates with electrostatic adhesion, and achieves order-of-magnitude improvements in performance compared to conventional clutches. In order to inform appropriate design in a variety of applications, I experimentally determined the effect of clutch length, width, dielectric thickness, voltage, and electrode stiffness on the holding force, engage and release times, and power consumption. The highest performance clutch held 190 N, weighed 15 g, and consumed 3.2 mW

This chapter appears as a research article in: S.B. Diller, S.H. Collins, and C. Majidi, "The effects of electroadhesive clutch design parameters on performance characteristics," *Journal of Intelligent Materials Systems and Structures*, vol. 29, no. 19, pp. 3804-3828, 2018

of power. The best samples released and engaged within 20 ms, as fast as conventional clutches. I also conducted a fatigue test that showed reliable performance for over 3 million cycles. I expect electroadhesive clutches like these will enable actuator designs that achieve dexterous, dynamic movement of lightweight robotic systems.

2.1 Introduction

Roboticians use clutches to reduce the energetic cost of actuation and achieve more versatile behavior by controlling how force and mechanical energy are transmitted in a system [26]. Many actuator designs improve energy efficiency by selectively engaging springs that use passive mechanics to exert force (Fig. 2.1a) [24, 45, 46, 27, 28]. Clutches also enable hybrid actuation schemes that can operate in multiple torque and speed regimes, for example by employing motors with dramatically different gearing ratios (Fig. 2.1b) [47, 48]. Alternatively, they allow for a single actuator to actuate many degrees of freedom with a one-to-many architecture (Fig. 2.1c) [49, 50]. Discrete stiffness tuning has been demonstrated with clutches to control mechanical interaction with humans in haptics applications (Fig. 2.1d) [51, 52, 53]. However, designers are challenged by the relatively high mass and power consumption of traditional active clutches that rely on solenoids, such as electromagnetic or magnetorheological clutches [27, 35]. Electrorheological clutches activate with directly applied voltage instead of a solenoid, but require thousands of volts and struggle to achieve high forces [54, 53, 55]. Passively locking devices eliminate the need for power input, but come with kinematic and control limitations and typically need to be customized for each application [24, 50]. Hydraulic layer-jamming devices achieve high forces with low weight and low theoretical power consumption, but take seconds to change states and require an accompanying compressor [36]. Fluidic matrix composites can quickly change stiffness, but require valves to operate and have relatively high off-state stiffness [56]. While the potential benefits of actuators that employ clutches are appealing, implementation with available

clutches remains challenging.

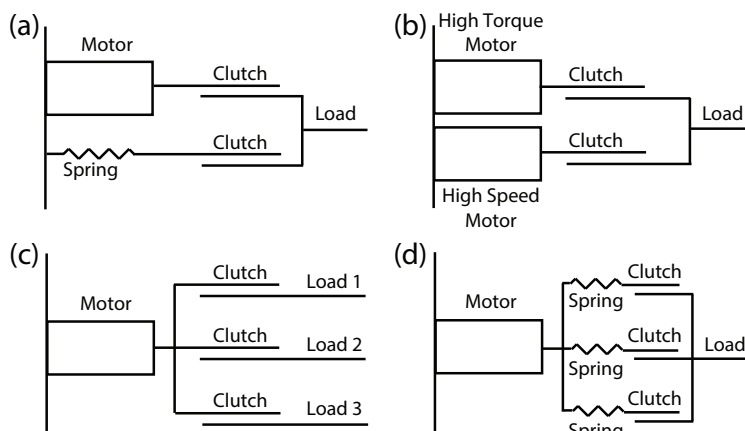


Figure 2.1: Actuator Configurations Using Clutches.

Controllable electrostatic adhesives display promising characteristics for translation into a clutching device. Compared to other clutching materials, electroadhesive films can be very lightweight and require very little power in order to form strong bonds with other surfaces. [38, 57]. Holding forces over 100 kPa have been reported [41], and reliable adhesion to various substrates has been demonstrated [40, 58, 39]. However, these devices are designed to adhere to substrates, as in applications such as robotic wall-climbing, and additional mechanisms and hardware must be incorporated to achieve a self-contained clutch. Previous attempts to create clutches that employ electroadhesion had only limited success because of slow response times and significant force hysteresis [42, 43], which are due mainly to materials selection and mechanical design.

To improve on this work, I designed and demonstrated a novel electroadhesive clutch that produced high forces with much lower mass and power consumption than conventional clutches (Fig. 2.2), while achieving comparable response times and controllability. However, without also having a broad knowledge of the effects of design choices, generalization of electroadhesive clutches to many usage cases would be slow and difficult. For instance, knowing the effect of increasing clutch area or applied voltage on force and clutch responsiveness would enable me to make informed design decisions for an application requiring ten times higher force than what I have previously demonstrated.

In this chapter, I performed a systematic experimental investigation of electroadhesive clutch design in order to better inform implementation in future applications. My goal was to establish a comprehensive set of design principles that can be used to employ electroadhesive clutches in a broad range of applications, as well as to direct further improvement of clutch performance.

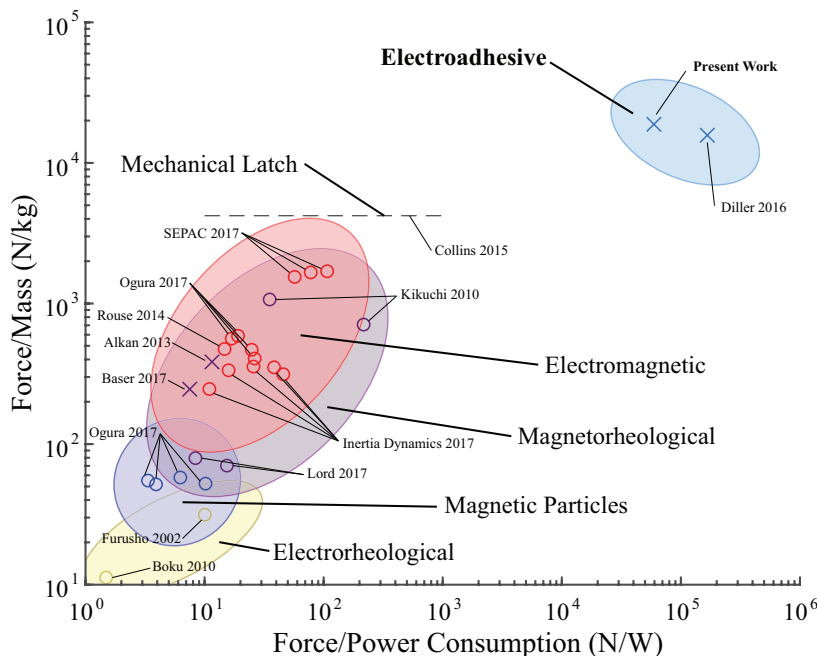


Figure 2.2: Comparison of mass and power consumption based on clutch mechanism. An 'x' indicates a linear clutch, and an 'o' indicates a rotary clutch. The torque of rotary clutches was converted to force by dividing by the radius of the clutch plate. Active clutches were only included if the force (or torque), mass, and power could be calculated or estimated from empirical data. The mechanical latch is shown as a dashed line because it consumes no power, but is not electrically controllable. The electroadhesive clutch achieves orders-of-magnitude improvements in performance compared to traditional clutches.

2.1.1 Experimental Design

The aim of this study is to gain answers and insights into the following design questions:

- Can clutch area be effectively scaled up or down for various applications, and what are the effects of changing its size?
- How much dielectric and electrode material are needed, and will less material necessarily achieve better holding force to weight ratios?

- How does operating voltage affect the holding force and power consumption?
- What factors contribute to reliable and fast release and engage?
- How long can electroadhesive clutches last under constant operation?

To answer these questions, I conducted an extensive characterization of clutch performance as a function of the design parameters. Using these results, I endeavor to provide practical guidelines and confidence to designers considering using electroadhesive clutches in their actuation schemes. Each experimental results section will lead the reader through the definition of a performance outcome, interpretation of the data, and how the results inform future designs. Next, I present an empirical model of clutch holding force derived from my experimental data and compare it to predictions from theory. Finally, I provide a design example and discuss the suitability of electroadhesive clutches for applications in robotics and beyond.

The design parameters varied in this study are illustrated in Figure 1.2d. Clutches have various widths, with one clutch plate slightly wider in order to prevent shorts across the edges of the electrodes. ‘Clutch length’ refers to the overlapping length between the two clutch plates, and is adjustable by changing the distance between the bolt attachment points before activation. The dielectric thickness and electrode thickness are varied independently, in order to separately investigate the effect of the separation distance between electrodes and the overall thickness and stiffness of the clutch plates. Finally, I vary the magnitude of the voltage applied across the electrodes of the two clutch plates.

2.1.2 Theoretical Model

A common theoretical model for predicting the maximum shear force in electroadhesive devices is given by the equation

$$F_x = \frac{\mu \cdot \epsilon \cdot \epsilon_0 \cdot A \cdot V^2}{2 \cdot d^2} \quad (2.1)$$

where μ is the coefficient of friction, ϵ is the relative permittivity of the dielectric, ϵ_0 is the electric constant, A is the interface area, V is the voltage, and d is the thickness of the dielectric [41]. I chose the design parameters to encompass most of the variables in this equation in order to facilitate a meaningful evaluation of the applicability of this theory to the performance of the device.

In the following section, I report measurements of the maximum holding force, release time, engage time, and power consumption of electroadhesive clutches as a function of clutch length, width, dielectric thickness, electrode thickness, and applied voltage. The maximum holding force is determined in a materials testing machine by increasing tension in the clutch until slipping occurs. I measure release and engage time by observing the changes in force and stiffness as the clutch is activated and deactivated under load. I determine the power consumption by measuring the capacitance and leakage current of the clutches at high voltage. Finally, I show the results of a fatigue life test conducted by repeatedly activating and loading the clutches.

2.2 Fabrication

The clutch plates were created by coating layers of an insulating ceramic-polymer composite (Luxprint 8153, Dupont Microcircuit Materials, Research Triangle Park, NC) onto aluminum-sputtered BOPET (Bi-axially Oriented Polyethylene Terephthalate) film, which served as the electrode. The 25 μm and 100 μm thickness films were sourced from Nielsen Enterprises (Kent, WA), and the 50 μm and 125 μm thickness films were sourced from McMaster-Carr (Aurora, OH). The McMaster-Carr films were generally higher quality, but were only available in 50 μm and 125 μm thicknesses. The aluminum coating of the BOPET served as the conducting surface for the electrode, while the polymer portion of the BOPET served as a backing to the aluminum and transmitted force from the interface of the two clutch plates to the carbon fiber bars. Changing the thickness of the BOPET was accom-

plished by changing the polymer backing thickness, and had no effect on the ability of the aluminum layer to provide an electrically conductive electrode surface. Instead, the thicker electrodes provided a stiffer connection between the clutch interface and the carbon fiber, and made the overall clutch plate thicker and stiffer. While only the surface aluminum layer conducts electricity, I refer to the entire aluminized BOPET film as the electrode in this paper. To coat the uncured Luxprint onto the conductive aluminum BOPET surface, one edge of a 15" square BOPET film was taped onto an 18" square first surface flatness mirror (First Surface Mirror LLC, Toledo OH), such that the entire BOPET film rested on the mirror. Uncured Luxprint was deposited along a line near the taped edge, and a 13 μm , 20 μm , or 27 μm profile rod (Zehntner GmbH Testing Instruments, Sissach, Switzerland), depending on the desired coating thickness, was pulled across the surface away from the taped edge. The coated film was immediately baked in a 1.9 cubic foot ventilated oven (Across International, Livingston, NJ) at 130° C under vacuum for 2 hours. The film was then removed and cooled at room temperature. After waiting at least 5 hours, the film was put back into the oven to bake for two more hours under the same conditions. The resulting thickness of the dielectric layer was approximately 10 μm , 18 μm or 25 μm , depending on the profile rod used and the speed and pressure applied during spreading of the uncured Luxprint. To create dielectric layers thicker than 25 μm , the coating process was repeated on top of the previously baked dielectric layers, until the desired thickness was achieved.

The coated electrodes were cut to size using a rotary cutter (Fiskars, Helsinki, Finland). If the sample did not have any uncoated surface of the BOPET for electrical contact, acetone was used to remove Luxprint from a small area. The electrodes were then attached to carbon fiber shims using a polyacrylate adhesive (VHB, 3M, Maplewood, MN). Silver particle-based conductive epoxy (MG Chemicals, Burlington, Canada) was used to make electrical contact between ring terminals and the conductive BOPET surface. The epoxy was cured by placing the entire clutch in the oven at 65° C for 1 hour under atmospheric pressure. Tensioning rubber bands (Pale Crepe Gold, Alliance, Hot Springs, Arkansas) were fitted into slots cut

in the carbon fiber and glued in place on the electrode side using cyanoacrylate glue. For every clutch, both BOPET electrodes were coated with Luxprint, so that the total dielectric thickness was the sum of the thicknesses of the coatings on each electrode. The alignment springs were attached via slots to the other clutch plate, such that the dielectric coatings contacted one another. One coated electrode was cut to be 1 cm wider than the other, to prevent shorting between the edges of the electrodes. An overview of the fabrication process can be viewed in the ‘Electroadhesive Clutch Fabrication’ video.

2.3 Experimental Characterization

2.3.1 Holding Force

Holding Force Methods:

The maximum clutch force before slip as a function of clutch width, length, dielectric thickness, electrode thickness, and voltage was determined using a materials testing machine (Instron 5969, Instron, Norwood MA). For each test, the clutch was loaded into the testing machine and voltage was applied using a high-voltage power supply (Model PS375, Stanford Research Systems, Sunnyvale, CA) to initiate adhesion. After waiting for one second to ensure full engagement, the testing machine strained the clutch at $10 \text{ mm}\cdot\text{min}^{-1}$ until at least two slips occurred (Fig. 2.3). The highest force value observed was recorded as the maximum holding force. In the vast majority of cases, the maximum holding force was observed just before the first slip. In the remaining cases the first slip occurred at a lower force because of a short through the dielectric layer. Pilot testing showed that the maximum holding force reached a steady state value after about 3 consecutive tests. Based on this result, I conducted 6 consecutive tests on each clutch at each condition, with about 10 seconds between tests. The maximum holding forces from only the last 3 tests were included in the dataset. With the exception of the multi-parameter dielectric thickness and voltage sweep,

three separate clutches were tested at each condition. Because the final dielectric thickness was difficult to precisely control during fabrication, I decided to test many clutches with many distinct dielectric thicknesses for the 2D dielectric thickness and voltage sweep, as opposed to making 3 identical clutches at each of a few dielectric thicknesses. The thickness of the dielectric coating of each clutch plate was measured four times at each corner using a micrometer (Mitutoyo IP65, Mitutoyo, Kawasaki, Japan) that has a resolution of $1\ \mu\text{m}$. The reported dielectric thickness of each clutch was calculated by adding the thicknesses of the dielectric coatings on the two electrodes to find the total thickness of dielectric material separating the electrode surfaces. The clutches tested in the sweep of area had $50\ \mu\text{m}$ thick electrodes, dielectric thickness of $36 \pm 2.9\ \mu\text{m}$, and were activated with 250 V. The clutches tested in the sweep of dielectric thickness and voltage had $50\ \mu\text{m}$ thick electrodes, 10 cm overlap length, and 8 cm width. The clutches tested in the sweep of electrode thickness and length had dielectric thickness of $36.6 \pm 3.9\ \mu\text{m}$, 8 cm width, and were activated with 250 V. Test order for all conditions on each clutch was randomized. Clutches were rested for at least 3 hours between measurements.

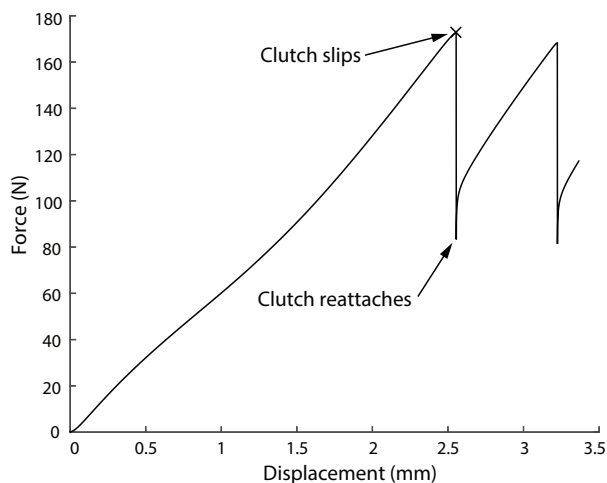


Figure 2.3: A representative maximum holding force test. After slipping, the clutch immediately reattaches at a lower force because the voltage is still being applied. The slipping force slowly decreases as more slips occur, because the clutch overlap length decreases by a small amount after each slip.

The maximum holding force was also tested as a function of time. For each test, the clutch was loaded into a materials testing machine (Instron 4469, Instron, Norwood MA,

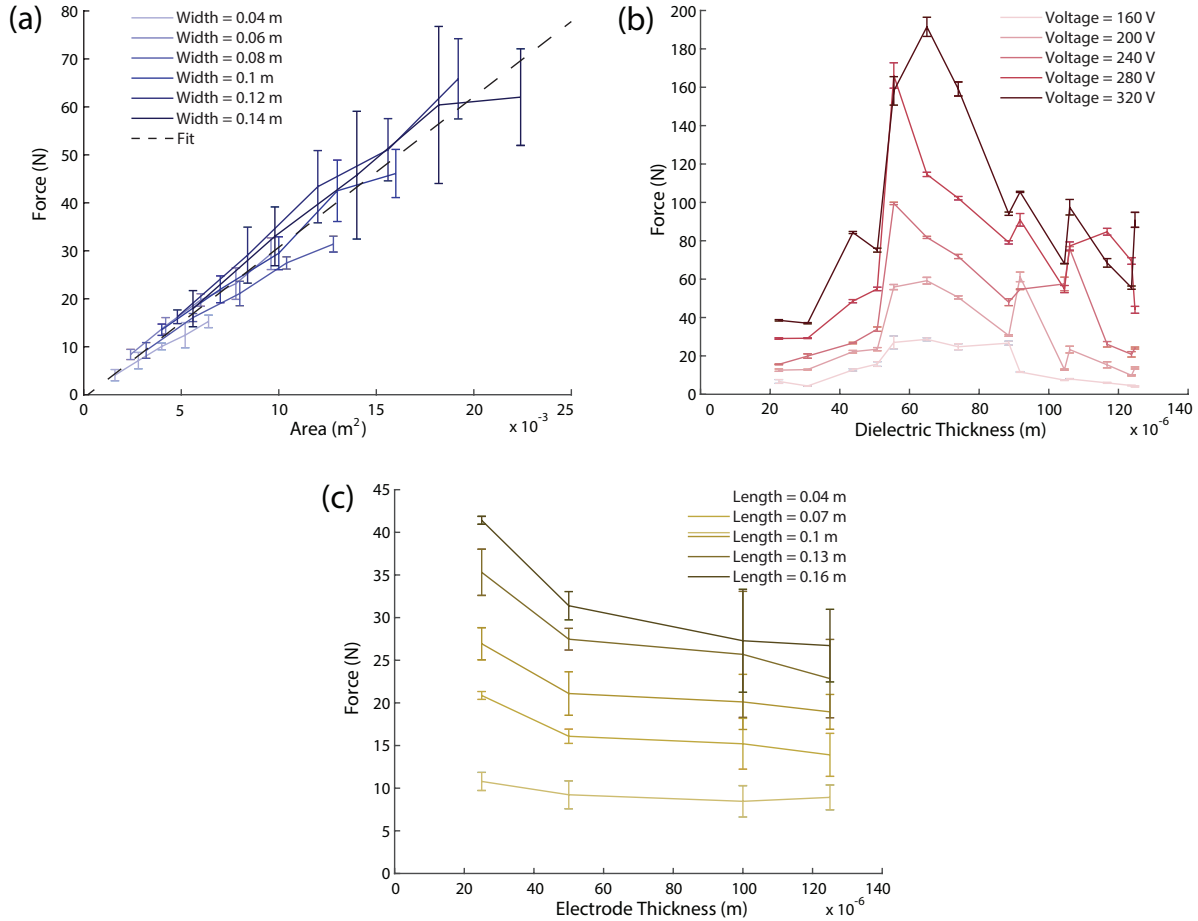


Figure 2.4: Maximum Holding Force Results. a) Maximum force as a function of area, with lines of constant width and applied voltage of 250 V. b) Maximum force as a function of dielectric thickness, with lines of constant voltage and 50 μm electrode thickness. c) Maximum force as a function of electrode thickness, with lines of constant length and applied voltage of 250 V.

MTS ReNew Upgrade, MTS, Eden Prairie, MN), and a voltage of 250 V was applied with the high voltage power supply. The clutch was left activated for a predetermined amount of time that was varied between tests. Then the clutch was displaced at $240 \text{ mm}\cdot\text{min}^{-1}$, causing the clutch to slip within 200 ms. The highest force value observed was recorded as the maximum holding force for that amount of activated time. I tested 6 clutches at 1 s, 3 s, 10 s, and 30 s activated time conditions. Each clutch was tested 6 times at each condition, and the last 3 tests were included in the dataset. The order of activation time conditions was randomized for each clutch. The clutches tested encompassed a range of clutch parameter values, including 25 μm and 50 μm electrodes, dielectric thicknesses between 22 μm and 92 μm , and overlap lengths of 8 cm and 14 cm. The maximum holding forces from all tests

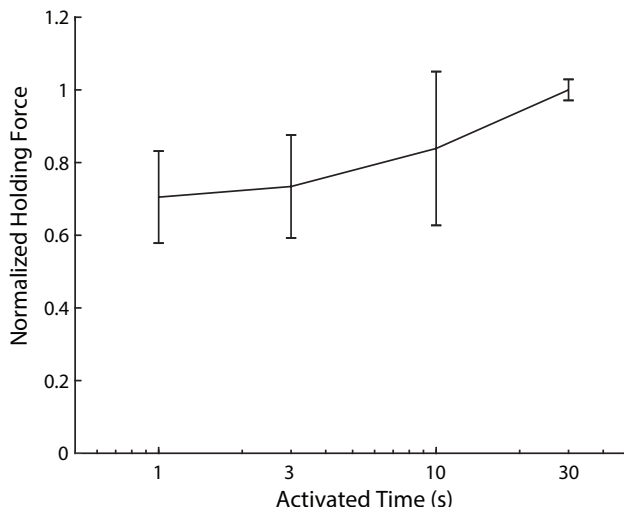


Figure 2.5: Normalized clutch holding force at 250 V as a function of the time between clutch activation and loading the clutch to slip. The clutch force is normalized to the slip force at the 30 second condition.

of each clutch were divided by the average maximum holding force of the 30 s activated time condition for that clutch. These normalized values were averaged, and the error bars indicate the standard deviation of the combined set of normalized values from all 6 clutches.

Holding Force Results:

Maximum clutch holding force increases approximately linearly with area for a large range of areas and aspect ratios (Fig. 2.4a). Dielectric thickness has a non-monotonic influence on maximum holding force (Fig. 2.4b). Holding force peaks in the 50 μm - 80 μm region, with large drop-offs as the thickness becomes larger or smaller. Across all dielectric thicknesses, holding force rises dramatically as applied voltage is increased. The maximum holding force rises moderately as electrode thickness decreases (Fig. 2.4c). Increasing length causes a linear increase in force independent of electrode thickness. The maximum clutch holding force increases as the amount of time the clutch is activated increases (Fig. 2.5).

Holding Force Design Insights:

These results indicate that clutch force is maximized by clutch plates with 25 μm thick electrodes and dielectric thicknesses in the 50 μm - 80 μm range. Further decreasing the

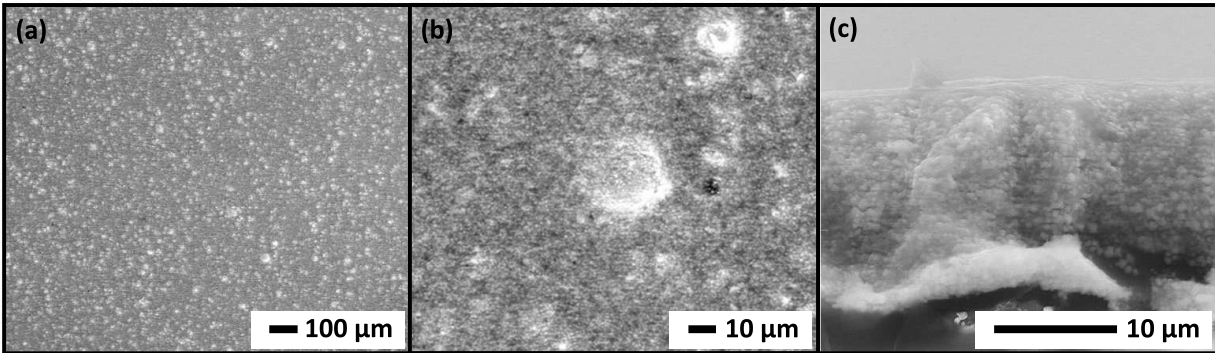


Figure 2.6: Environmental Scanning Electron Microscope images. a-b) Agglomerations of ceramic particles on the order of $10\ \mu\text{m}$ are visible on the dielectric surface. Energy-Dispersive Spectroscopy analysis confirmed that the agglomerations are made up of barium titanate and titanium dioxide. c) Cross-section of the dielectric layer. The individual ceramic particles are visible in the polymer matrix. All images were taken at 25 kV using a Quanta 200 (Thermo Fisher Scientific, Hillsboro, Oregon, USA).

electrode stiffness could increase maximum holding force. However, the yield strength of the BOPET material may begin to restrict the operating force of the clutch. For example, an 8 cm wide clutch with $25\ \mu\text{m}$ electrodes is expected to begin to yield at approximately 200 N given a yield strength of 100 MPa [59] at room temperature, which is only slightly larger than the measured slipping force of some clutches with 10 cm overlap length. Force can be expected to scale up or down linearly with the clutch overlap area, although clutch area has a strong effect on other performance outcomes, as is discussed in the Release Time section. For all of the clutch designs tested in this paper, the clutch slipped at the electroadhesive interface rather than experiencing a yielding failure in the materials or structure. Because the stress in the BOPET film and at the VHB interface scales inversely with clutch width for a given film thickness and overlap area, the clutch aspect ratio should be controlled during the design process by increasing width and decreasing length until the expected stress in the BOPET film is below the yield stress. Increasing voltage also increases clutch force, but has a strong affect on force hysteresis and power consumption, as discussed in the next subsection on Space Charge and a later section on Power Consumption.

The holding force of clutches activated for 1 second is approximately 70% of the holding force after being activated for 30 seconds. The holding force does not appear to plateau

after 30 seconds of activation time, implying that even higher forces may be reached with longer activation time. This result also shows that the electroadhesive clutch is capable of transmitting large holding forces within 1 second of activation. This time-dependent effect likely added some bias into the greater holding force parameter sweep experiment. Because the tests in the main holding force study were meant to be quasi-static, I tested at a low displacement rate. This meant that tests of parameter values that held large forces took up to 15 seconds longer than parameter values with low force capability, potentially causing a further relative difference in force transmitting capability. Additional tests of the interaction of displacement rate, activated time, and other clutch parameters such as voltage could give additional insight on the fundamental mechanisms underlying this effect.

Space Charge:

I also note several factors that affect performance but that I have not systematically investigated in this work. One such factor is that increasing voltage to 320 V and beyond begins to have detrimental effects on clutch performance. Specifically, I observe unwanted adhesion due to space charge, or electric charge that is forced into the insulating layer and remains even after the voltage is removed [60, 61]. Unwanted adhesion can be problematic when the clutch is in the off state, because the clutch plates buckle under very small compressive loads and consequently do not slide relative to one another. Quantifying the presence of space charge has proven to be a challenge. A remaining voltage is only observable with a voltmeter when the electrodes are slid relative to one another, and the transient nature and strong history dependence of space charge make it difficult to systematically investigate its interaction with the performance outcomes. I have seen cases where suspected space charge induced by large voltages seems to temporarily slow release time and decrease maximum holding force. Further investigation into techniques of measuring space charge in the system and counteracting its effects are warranted.

Materials:

Our selection of materials is vital to achieving good performance. Using aluminum-sputtered polymer film as the electrode provides the right combination of out-of-plane flexibility and high in-plane stiffness. The dielectric material choice is critical, and I use Luxprint, which is a fluoropolymer embedded with barium titanate and titanium dioxide, because it displays high breakdown strength and a high dielectric constant of approximately 20-30. Additionally, this dielectric is not tacky and does not have inherent adhesion, meaning that the clutch can automatically release and reliably slide in the off state. The diameter of the ceramic particles is reported by the supplier to be less than $5\ \mu\text{m}$, but I believe the drop-off in performance at thicknesses less than $50\ \mu\text{m}$ may be due to agglomerations of the particles on the order of $\sim 10\ \mu\text{m}$ (Fig. 2.6). The presence of these agglomerations would lead to localized electric charge accumulation that could cause shorting and a lower bulk dielectric constant. Using a composite with smaller particles or chemical modification to prevent agglomeration could dramatically improve the performance of thinner layers and allow much lower applied voltage and higher force transmission.

2.3.2 Release Time**Release Time Methods:**

The release time testing was also conducted using the Instron materials tester, but the force was measured using a load cell (LC201-100, Omega, Norwalk, CT) placed in series with the clutch and recorded at 5000 Hz by a separate control hardware system (DS1103, dSPACE, Wixom, MI). A microcontroller (Arduino Uno, Somerville, MA) was used to control the clutch state and simultaneously send control state signals to the control hardware system. I chose not to use the Instron measurements because of embedded filtering, which prevents measurements on the millisecond scale, and because of software delays on the order of 10 ms. During each test, the clutch was activated, loaded to 80% of the measured or estimated

maximum force, and released (Fig. 2.7). At each condition, clutches were tested six times, with about 10 seconds between tests. Pilot testing did not show any change in performance over consecutive tests, so all 6 tests contributed to the dataset. The force signal was zero-phase 250 Hz low-pass filtered to eliminate background noise. I defined the release time as the time needed for the force to drop by 90% relative to the steady state force after release. All clutches used in the force testing were also tested for release time under the same conditions, with the exception of the set of samples in which electrode thickness was varied. Rather than testing the interaction of electrode thickness and length as in the maximum holding force study, these samples were tested for the interaction of electrode thickness and voltage. The electrode thickness sweep samples were tested at an overlap length of 10 cm. Clutches were rested for at least 3 hours between measurements. Real-time and high-speed video of release time testing can be viewed in the ‘Electroadhesive Clutch Release and Engage Time Testing’ video.

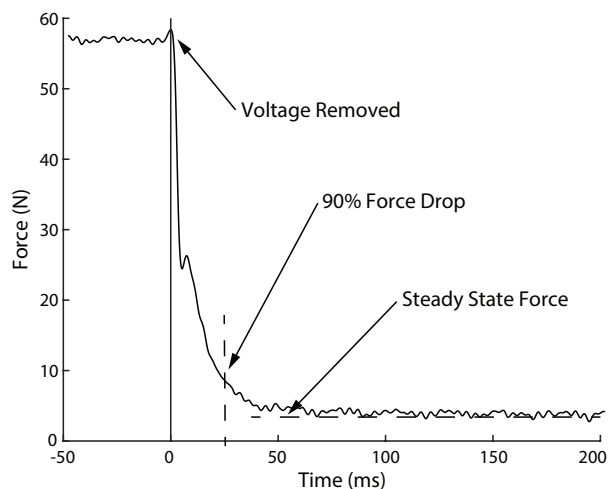


Figure 2.7: A representative force profile during release. After the voltage is removed from a clutch under load, the force rapidly drops to a steady state value dependent on the force in the tensioning springs. We define the release time as the time required to drop to within 10% of the steady state value. About halfway through the release, an inflection in the force profile occurs. This occurs in most releases, and can vary significantly in its magnitude of force.

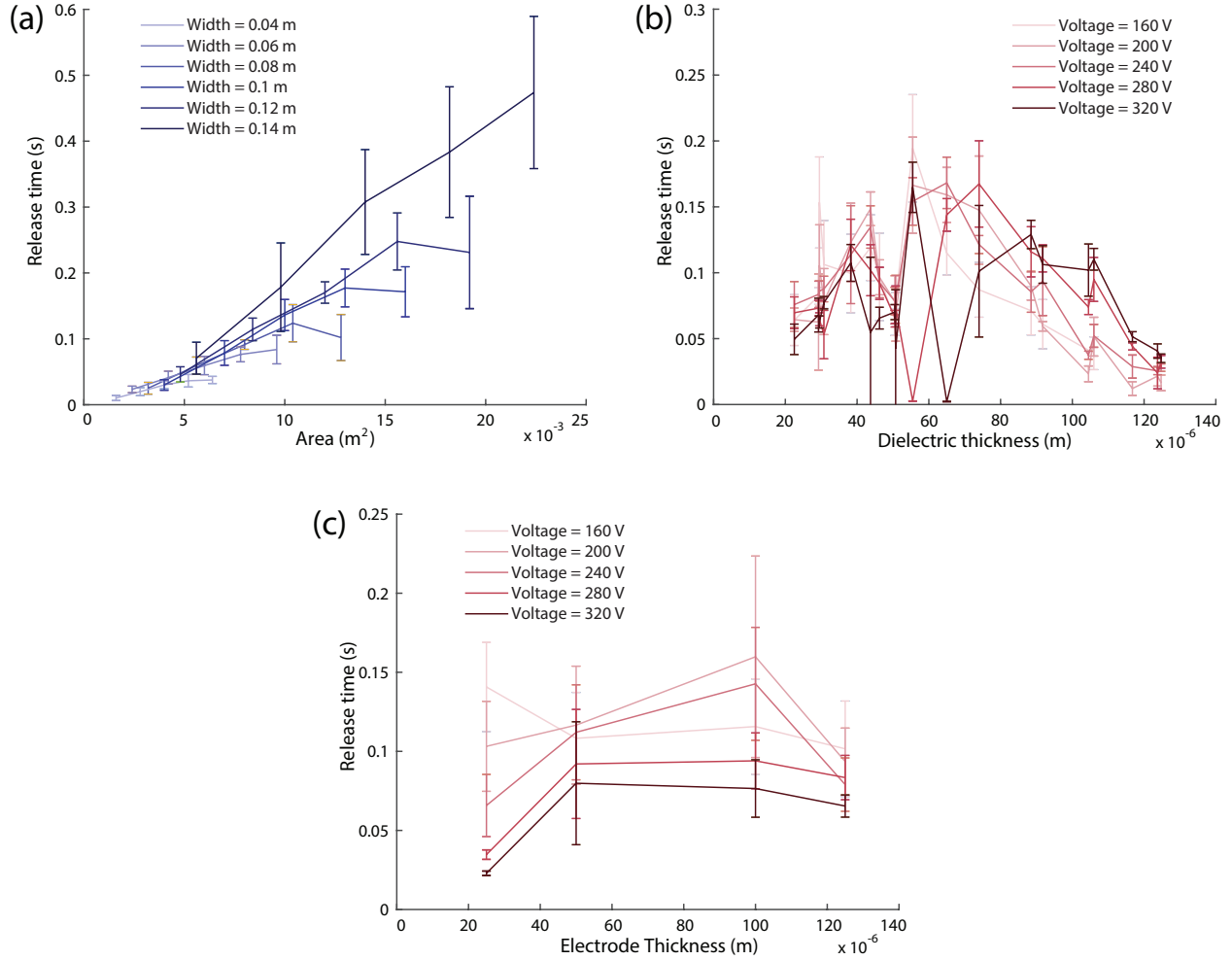


Figure 2.8: Release Time Results. a) Release time as a function of area, with lines of constant width. b) Release time as a function of dielectric thickness with lines of constant voltage. c) Release time as a function of electrode thickness, with lines of constant voltage.

Release Time Results:

Release time slows as area increases, and increasing clutch width increases the release time more sharply than increasing clutch length (Fig. 2.8a). For dielectric thicknesses $\geq 80 \mu\text{m}$, release time becomes faster as dielectric thickness increases and applied voltage decreases (Fig. 2.8b). The samples used in the sweep of electrode thickness have dielectric thickness of $36.6 \pm 3.9 \mu\text{m}$. With this in mind, considering Fig. 2.8b and c, the opposite trend appears to occur for thin samples with dielectric thickness $\leq 40 \mu\text{m}$. For this region, release time becomes faster as dielectric thickness decreases and applied voltage increases. For intermediate dielectric thicknesses, there is no clear relationship between release time

and dielectric thickness or voltage. The outlying data in this region that show very fast release time occur because of my definition of release time, and for practical purposes release at similar speeds to the other data at those dielectric thicknesses. The outliers occur because the small inflection at approximately 25 N in Fig. 2.7 is much taller, and actually dips below the 90% force drop value before rising and following the typical force profile. Future work is warranted to investigate the mechanics behind this feature of the force drop curve. Electrode thickness does not seem to have an effect on release time (Fig. 2.8c), although the fastest release in this subset of clutches occurred for the 25 μm thick electrode at 320 V.

Release Time Design Insights:

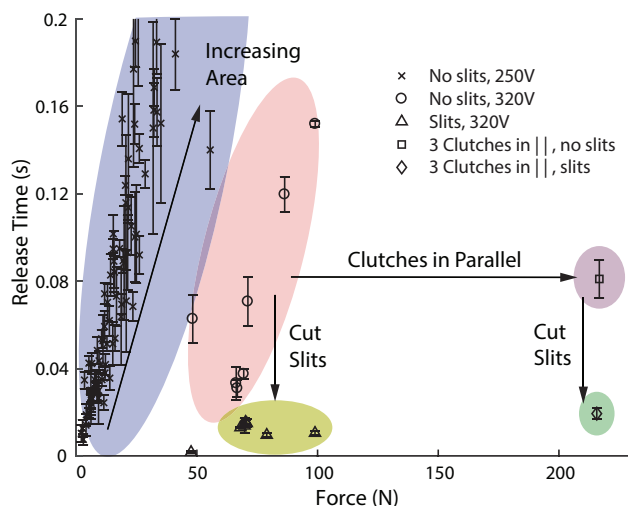


Figure 2.9: Release Time and Holding Force. Scaling force by increasing area dramatically slows release time. Increasing voltage and using multiple smaller clutches in parallel scales force without sacrificing responsiveness, and cutting parallel slits in the clutches dramatically decreases release time.

Based on the findings in Fig. 2.8, the clutch area is the dominant design parameter in determining the release time. These findings imply that clutches with large continuous area or width cause slow release and should be avoided. This result leads me to consider other ways of scaling force while maintaining fast release time.

Increasing the continuous area of the clutch to increase force causes a corresponding increase in the time needed to release (Fig. 2.9). The finding that width has a particularly

strong effect on release time inspired an experiment in which I placed multiple clutches in parallel. When 3 clutches are loaded to 220 N and released, the release time is approximately the same as their individual release times when released at 70 N. This result implies that the continuous area of each clutch dominates release time, and additional clutch area and holding force can be added without penalty as long as it is not continuous area on a single clutch. To further explore this strategy, I cut slits along the length of one of the two clutch plates to decrease the continuous width to 1.3 cm, and find that this dramatically reduces the release time of individual clutches as well as multiple clutches in parallel. This result leads to the important design insight that continuous area in the clutch plates should be minimized in order to achieve fast release in clutches that can hold large forces.

2.3.3 Engage Time

Engage Time Methods:

The engage time was calculated by comparing a linearized baseline force-displacement curve to ‘dynamic engage’ tests. During the dynamic engage test, the clutch was activated while being displaced at a constant rate (Fig. 2.10). The amount of extension after the voltage was applied and before the clutch was fully engaged was determined by shifting the reference force-displacement curve until the force profile coincided with the dynamic engage curve. This extension shift correlated to a time value, because the dynamic test was conducted at a constant velocity. This time, which I called the engage time, is essentially the time needed for the stiffness of the engaging clutch to match its baseline stiffness.

Engage time measurements were also made with the Omega load cell and dSPACE system. In addition, the displacement was measured by dSPACE using the analog output of the Instron, which I separately verified did not have filtering or software delays. To determine the baseline force-displacement curve, the clutch was activated and loaded to 20 N at a rate of $100 \text{ mm}\cdot\text{min}^{-1}$. This test was repeated three times for each condition, and the final two tests were fit with a linear curve. The dynamic engage tests were performed by initiating

an extension velocity of $100 \text{ mm}\cdot\text{min}^{-1}$ while the clutch was deactivated. Once constant velocity was reached, the microcontroller simultaneously engaged the clutch and signaled the measurement system, indicating the time and displacement at clutch activation. Voltage was provided by the high voltage power supply, and a $4.7\mu\text{F}$ capacitor was placed in parallel with the power supply to provide a responsive current source. The force and extension signals were both zero-phase low-pass filtered at 20 Hz. This filtering did not adversely affect my ability to measure fast engage times because I was not measuring an impulse-like behavior that would be masked by a low-pass filter. Instead, I measured the stiffness at a time well past the initial engage, and this part of the curve is very smooth. Additionally, because I used a two-way filter, the curve was not delayed relative to the activation time. The dynamic engage test was performed four times per clutch at each condition, and all four tests contributed to the dataset. Parameter sweeps of length, width, electrode thickness, and voltage were conducted for engage time, with 3 clutches tested at each condition. The clutches in the sweep of width had a mean dielectric thickness of $36 \pm 2.7 \mu\text{m}$, length of 13 cm, electrode thickness of $50 \mu\text{m}$, and applied voltage of 280 V. The clutches in the sweep of length had a mean dielectric thickness of $37 \pm 2.6 \mu\text{m}$, width of 8 cm, electrode thickness of $50 \mu\text{m}$, and applied voltage of 280 V. The clutches in the voltage sweep had a mean dielectric thickness of $31 \pm 0.9 \mu\text{m}$, overlap length of 13 cm, width of 8 cm, and electrode thickness of $50 \mu\text{m}$. The clutches in the electrode thickness sweep had a mean dielectric thickness of $36 \pm 3.9 \mu\text{m}$, overlap length of 13 cm, width of 8 cm, and applied voltage of 280 V. The order of conditions was randomized for each clutch. Real-time and high-speed video of engage time testing can be viewed in the ‘Electroadhesive Clutch Release and Engage Time Testing’ video.

Engage Time Results:

Engage time decreases moderately as clutch width increases (Fig. 2.11a). I believe that clutches with more area engage faster because there is a higher likelihood that some portion

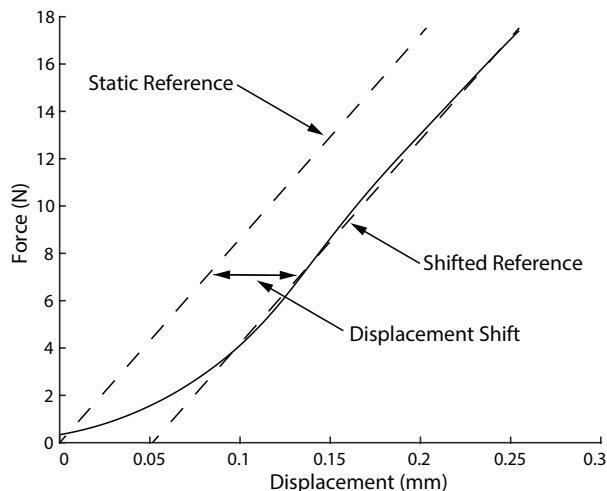


Figure 2.10: A representative force profile during engage. The voltage is applied at time zero, and the static reference line shows the expected force-displacement profile of a fully engaged clutch. By shifting the reference curve to the right until the curve coincides with the dynamic test, we determine the amount of displacement lost before the clutch is engaged. Because the velocity is constant, this displacement corresponds to a time value, which we call the ‘engage time.’

of the clutch plates will be in contact before activation to serve as an initiation point for zipping on. The engage time is quite dependent on the overlap length (Fig. 2.11a), with the 10 cm and 16 cm conditions engaging most quickly. I believe this effect is due more to the clutch configuration and tensioners than to the absolute overlap length. The clutches used to test various lengths were created in two sizes, with maximum designed overlap lengths of 10 cm and 16 cm, and these clutches were activated in lengthened configurations to produce the 4 cm, 7 cm, and 13 cm conditions. However, these configurations have higher tensioner force than the 10 cm and 16 cm conditions, which I believe decreases the likelihood of initial contact and hinders the zipping on effect, leading to slower engage times. Clutches engage much faster as the applied voltage increases (Fig. 2.11b), which is likely due to higher attractive forces at higher electric field strengths. Engage time occurs faster as the electrode thickness decreases, with the exception of the 100 μm clutches (Fig. 2.11c). This outlier is most likely due to noticeable curvature in these samples resulting from residual stresses in the electrodes.

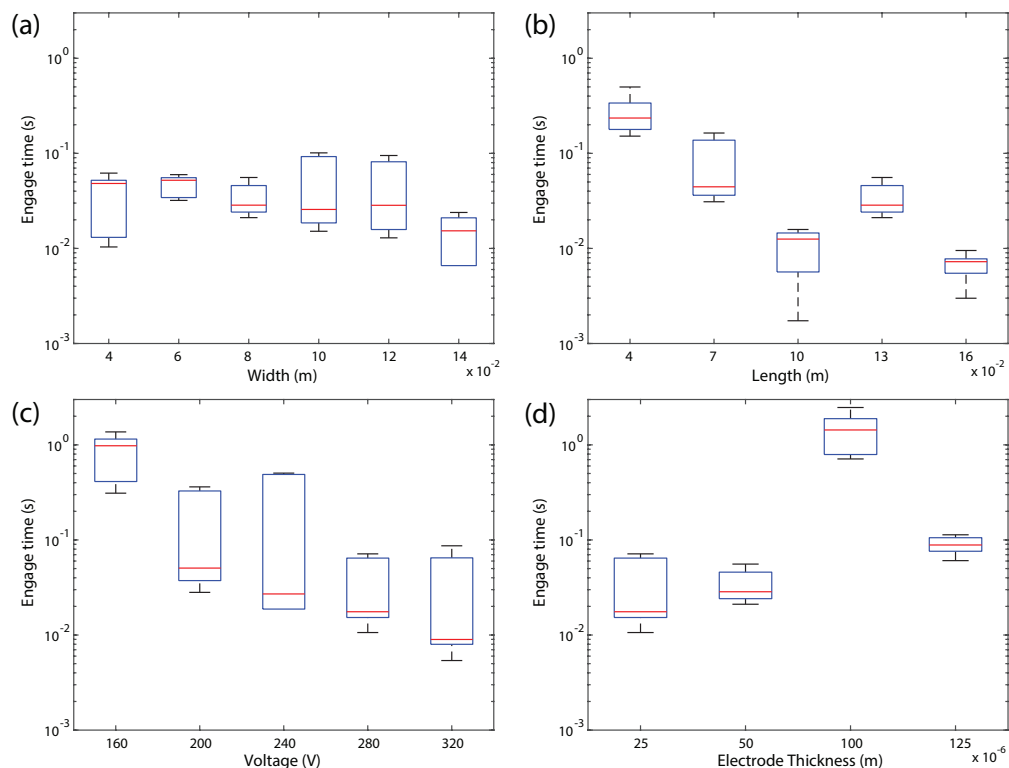


Figure 2.11: Engage time results. These box-and-whisker plots show the median in red, the 25th and 75th percentiles with the blue box, and the most extreme data points with the whiskers. a) Engage time as a function of width. b) Engage time as a function of length. c) Engage time as a function of voltage. d) Engage time as a function of electrode thickness.

Engage Time Design Insights:

Clutch engage occurs faster for clutches with more area, potentially placing this performance measure at odds with the release time, which becomes slower as continuous area increases. However, engage time tests of clutches with slits show that they can engage within 30 ms, meaning that both fast engage and release can be achieved by employing slits. Using higher voltage and thinner electrodes benefits engage time, a result that meshes well with the force and release time results for these parameters.

The electrode thickness and length outliers in the engage time data illustrate the dependence of engage time on the curvature of the electrodes and the force from the tensioning rubber bands. The residual curvature in the clutches develops during fabrication and results from the thermal mismatch between the electrodes and insulating material, as well as uneven cooling rates after baking. Residual curvature induces elastic restoring forces

in the films that cause the centers of the electrodes to be pushed away from one another. This can prevent the clutch plates from having any initial contact area, which is necessary for the electrodes to initiate adhesion. These effects were particularly pronounced in the 100 μm electrodes, perhaps due to the methods and processing performed by the BOPET manufacturers. This negative effect is exacerbated when vertical slits are cut for all electrode thicknesses, because the length-to-width ratio of the continuous patches dramatically changes, and the carbon fiber backing cannot as effectively constrain the electrode to be flat. I find that sliding the electrodes over a sharp edge before attaching them to the carbon fiber backing is an effective method to remove curvature. In fact, using this method to bias the curvature to the other direction is actually beneficial in guaranteeing some initial contact area for engagement, allowing the electrodes to quickly zip on and conform to one another.

The force in the alignment tensioners also plays a role in determining the initial contact area of the clutches. If the force is too low, the electrodes can go slack and buckle away from one another. Alternatively, if the force is too high, the electrodes can be too taut and not contact one another at all. One way to ensure relatively constant tensioner force over the whole operating range is to use springs with fairly low stiffness and a significant pretension. Both the curvature and tensioners should be carefully designed in each implementation of the clutch. Fast engage time is also aided by supplying a good current source, which I achieve by placing a high-voltage capacitor into the circuit. The capacitor slowly charges from the low-power voltage transformer, and is capable of providing very high instantaneous current to the clutch, allowing full charging in milliseconds. Because the capacitor has orders-of-magnitude higher capacitance than the clutch, the overall voltage decrease resulting from charging the clutch is very low. These tension, curvature, and charging effects all significantly influence the speed and reliability of clutch activation and need to be carefully considered in each implementation.

2.3.4 Power Consumption

Power Consumption Methods:

I determined capacitance and power consumption of the clutches by charging and discharging clutches while measuring electrical current. Current was calculated by measuring the voltage drop across a 100 k Ω shunt resistor placed in series with the clutch, using two high impedance voltage dividers (see *Control Circuits* in the Appendix). The electrical charge in the clutch was determined by numerically integrating the current during discharging (Fig. 2.12). The clutch was considered to be discharging until the voltage across the capacitor had dropped by 99% of the applied voltage. The capacitance was then calculated as

$$C = \frac{Q}{V} \quad (2.2)$$

where Q is the total charge and V is the applied voltage. The leakage current during the charged state was also observed using this circuit. The power consumption was calculated using the measured capacitance and leakage current as

$$P = I_{\text{leak}} \cdot V \cdot D + \frac{1}{2} \cdot C \cdot V^2 \cdot f \quad (2.3)$$

where I_{leak} is the leakage current, D is the fraction of time the clutch is activated, C is the capacitance of the clutch, and f is the frequency of activation. For my calculations, I assumed an activation frequency of 1 Hz and an activation time fraction of 0.5.

Power Consumption Results:

While varying clutch width, dielectric thickness, and electrode thickness, power consumption scales approximately linearly with maximum holding force (Fig. 2.13a). This result makes intuitive sense for varying width, as both force and capacitance scale linearly with clutch width. This is a surprising result, however, for varying dielectric thickness, as these

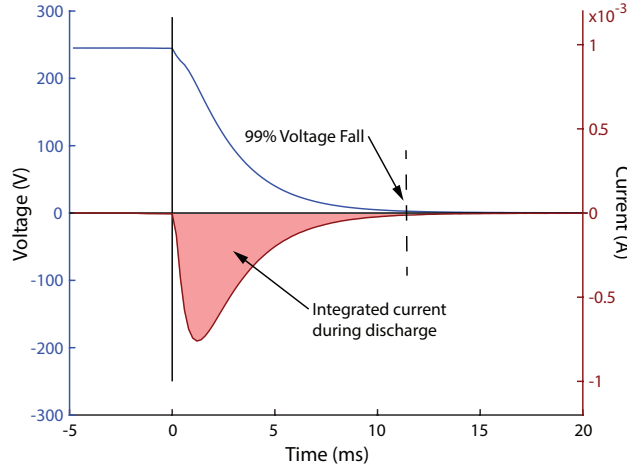


Figure 2.12: A representative clutch discharge curve. The voltage drops to 1% of its initial voltage within 12 ms. The current during discharge is integrated to determine the charge contained in the activated clutch.

results imply a linear relationship between capacitance and holding force that is not predicted by the friction-controlled electrostatic model, as described in the Comparison to Classic Electrostatic Theory section. For these clutches, leakage current accounts for 22% of total power consumption on average, making it a relatively small cost compared to charging the clutches during activation.

The power consumption of a small subset of clutches was measured as a function of voltage (Fig. 2.13b). Power consumption increases dramatically with increasing voltage, scaling as $V^{4.2}$, which is much higher than the prediction of V^2 from Eq 2.3. This result can be explained by the dependence of clutch capacitance on clutch voltage (Fig. 2.13c). Because the electrostatic pressure is higher at larger applied voltages, more of the air gap at the interface of the clutch plates is eliminated, effectively increasing the dielectric constant and decreasing the dielectric thickness. Additionally, the high electric field strength may cause a nonlinear relationship between applied field and dielectric polarization that could contribute to this effect.

Power Consumption Design Insights:

Because of the relatively flat and linear data in (Fig. 2.13a), power consumption does not require strong consideration when selecting the width, dielectric thickness, and electrode

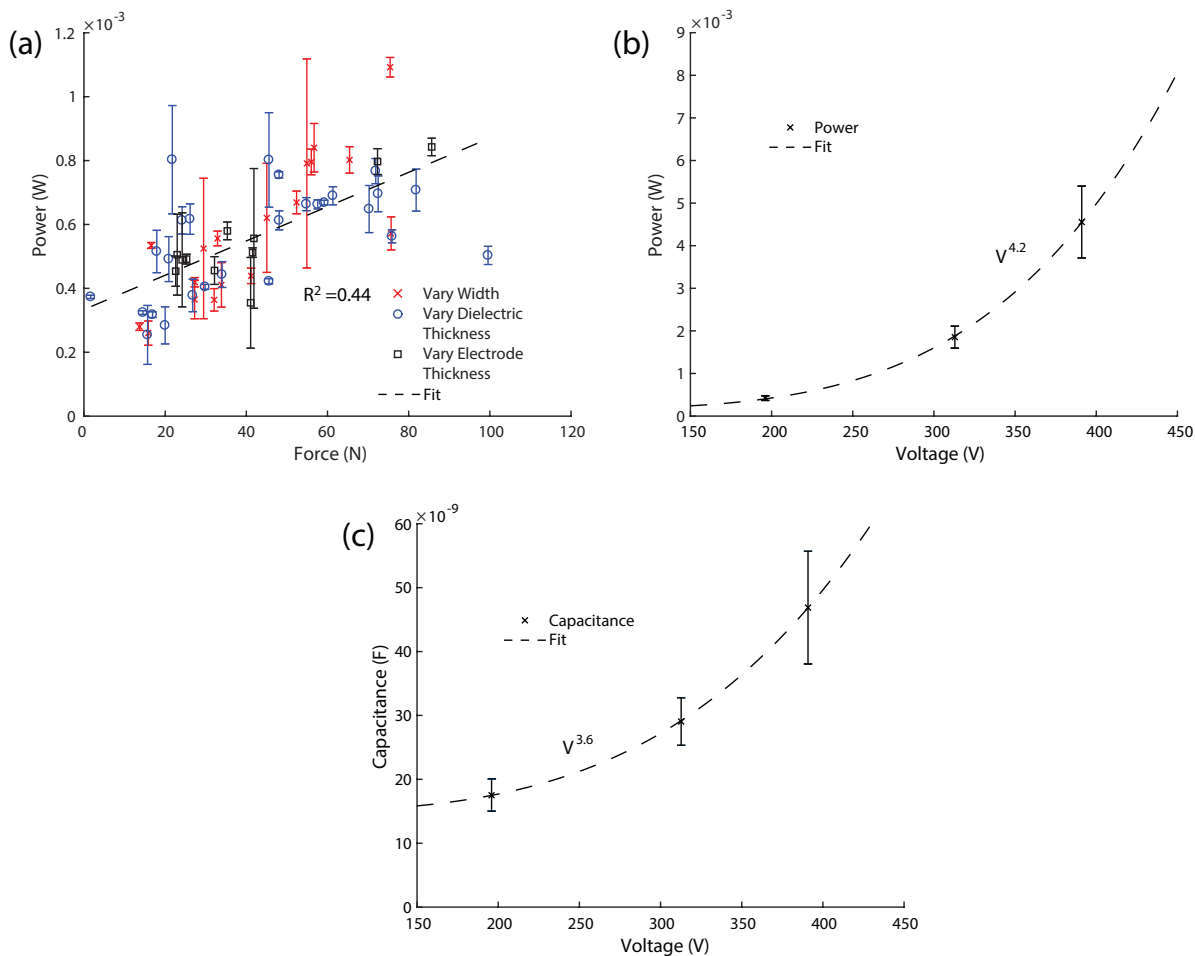


Figure 2.13: a) Power consumption and maximum holding force. The 'Vary Width' dataset includes clutches of various widths that have constant dielectric thickness and electrode thickness. The other two conditions follow the same pattern. b) Power consumption as a function of applied voltage for three similar clutches. c) Capacitance as a function of applied voltage for the same three clutches from (b).

thickness of a design. Although using higher voltages quickly increases power consumption, the power consumption is not a hindrance to the implementation or practicality of the clutch. The estimated power consumption of the $65 \mu\text{m}$ clutch at 320 V is 3.2 mW, which is still very low compared to traditional clutches.

2.3.5 Fatigue Life

Fatigue Life Methods:

Fatigue tests were conducted by repeatedly loading and unloading the clutch. Each cycle was composed of a phase in which the clutch was activated, loaded, and then unloaded, followed by a ‘free-sliding’ phase during which the clutch was displaced while the voltage was off, in order to ensure full disengagement of the clutch. The clutch was attached to a fixture with the Omega load cell in series, and a Kollmorgen (KM-180 E61960) servomotor displaced the free end. The dSPACE control system controlled the clutch activation circuit, and the high voltage power supply provided voltage, with a parallel capacitor acting as a current supply. The direction of applied voltage was alternated on each cycle. A controller was implemented to keep peak on-state force constant on each loading cycle (see *Fatigue Testing Control* in the Appendix). The maximum force during the off-state free-sliding cycle was also recorded, in order to investigate the unwanted residual adhesion as a function of cycle number. The off-state force was filtered to remove background noise, because a maximum value rather than an averaged value was recorded. Video of fatigue life testing can be viewed in the ‘Electroadhesive Clutch Fatigue Testing’ video.

Fatigue Life Results:

The fatigue testing results for one clutch are shown in Fig. 2.14. The clutch performs more than 3.3 million loading cycles, with the clutch temporarily losing functionality 34 times, corresponding to approximately one loss in functionality per 100,000 cycles. The unwanted remaining adhesion of the clutch observed during the free-sliding phase starts at 0.5 N, but rises slowly during the course of the fatigue test, to a maximum value of 7 N. The clutch is able to restart within 5 seconds of a loss in functionality. Short rests of less than 5 minutes do not seem to affect the unwanted off-state residual force upon restarting the test. However, a two week rest corresponded to a notable drop in residual adhesion of 4 N. The clutch

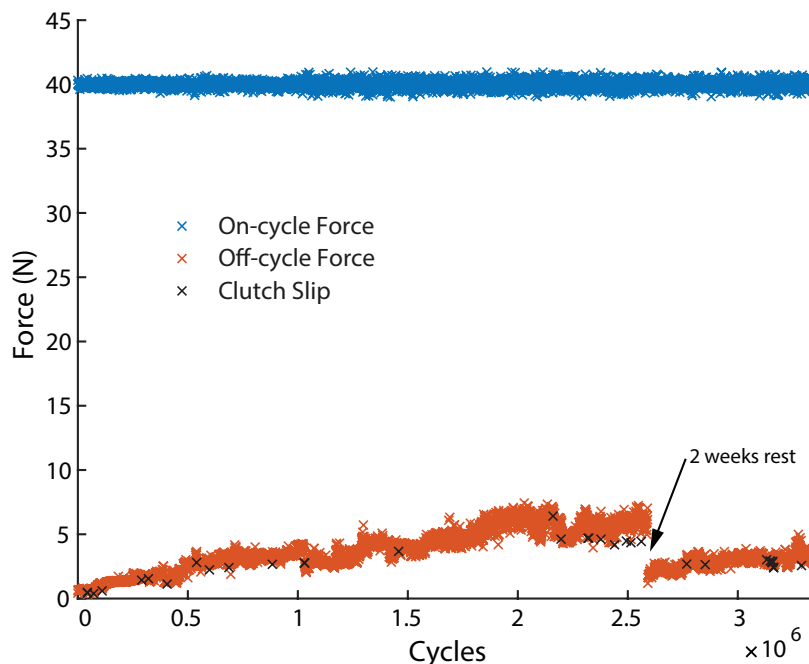


Figure 2.14: Fatigue testing. The maximum holding force and residual off-state force are plotted as a function of fatigue cycle number. The slip events are also indicated, overlaid on the off-cycle force of the cycle preceding the slip event. A two-week break in testing is indicated with the arrow.

shows very reliable operation for an extended usage time comparable to the requirements of many possible applications, and demonstrates that there is no fundamental mechanism limiting the lifetime of electroadhesive clutches. However, further investigation is warranted to understand the failure mechanisms, the rise in residual adhesion, and how clutch life is related to fabrication methods. Additionally, other performance outcomes including response time and power consumption should also be measured during fatigue testing.

Fatigue Life Design Insights:

To address residual adhesion in the off state for applications sensitive to this issue, the designer should consider replacing clutches after a few hundred thousand cycles, depending on their specific requirements. Further investigation could also inform techniques to delay or eliminate the rise in residual adhesion. Designers should include redundancy in the form of multiple parallel clutches to mitigate the loss in functionality when one clutch experiences a slipping failure. Including two clutches in parallel decreases the likelihood of a complete loss of force transmission to one in ten billion.

2.4 Data Analysis

2.4.1 ANOVA and Linear Regression Fitting

Model Derivation Methods

To extract key parameters and trends, I conduct an ANOVA analysis (Table 2.1). I find that clutch length, width, voltage, dielectric thickness, electrode thickness, and age have significant effects, while temperature, humidity, and test order do not. Clutch age is defined as the time between the last baking of the dielectric and the beginning of force testing. Temperature and humidity were not systematically varied during testing, and typically stayed within 20°C-22°C and 20%-50% humidity. Test order was randomized. I used linear regression to determine exponent coefficients for a model including the statistically significant parameters described by the equation

$$F_x = \exp(c_1) \cdot l^{c_2} \cdot w^{c_3} \cdot t_d^{c_4} \cdot t_e^{c_5} \cdot V^{c_6} \cdot age^{c_7} \quad (2.4)$$

where l is the length of the clutch overlap area in meters, w is the width of the clutch overlap area in meters, t_d is the total dielectric thickness in meters, t_e is the thickness of each BOPET electrode in meters, V is the applied voltage in Volts, and age is the clutch age in days (Table 2.2).

Table 2.1: Recorded Parameter Statistical Significance.

Parameter	P-value
Length	4×10^{-8}
Width	2×10^{-4}
Dielectric Thickness	3×10^{-11}
Electrode Thickness	1×10^{-4}
Voltage	5×10^{-30}
Age	1×10^{-8}
Temperature	0.3
Humidity	0.4
Test Order	0.7

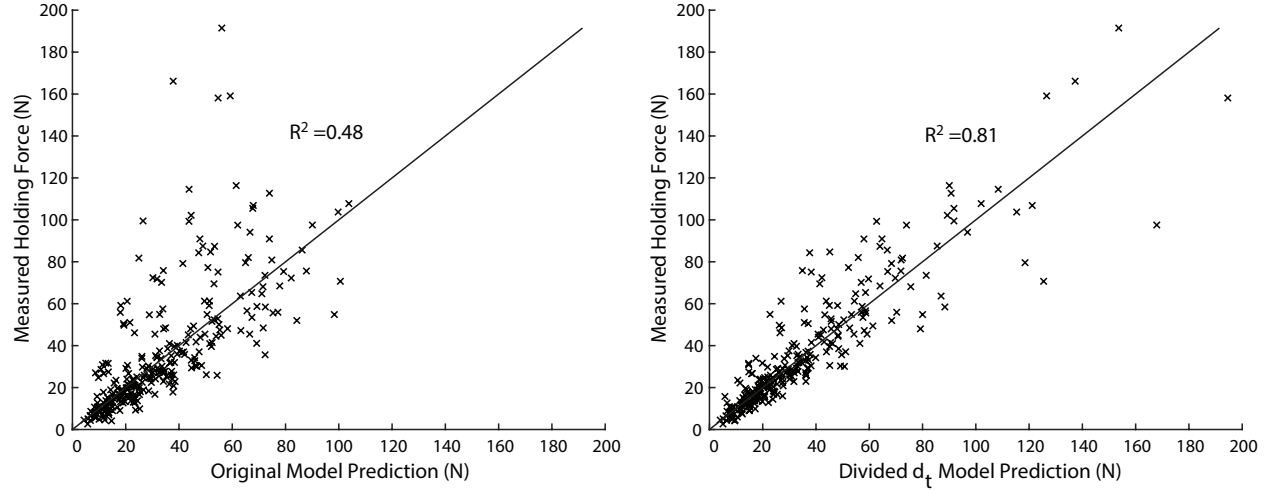


Figure 2.15: Maximum holding force model prediction vs. measured data. a) The model based on Eq. (2.4). b) The model based on Eq. (2.8), with data divided by dielectric thickness. Partitioning dielectric thickness substantially improves the model prediction.

The coefficients were determined using a linear regression with $x = A^{-1}b$ where

$$A = [1 \quad \ln(l) \quad \ln(w) \quad \ln(t_d) \quad \ln(t_m) \quad \ln(V) \quad \ln(age)] \quad (2.5)$$

$$b = [\ln(F)] \quad (2.6)$$

$$x = [c_1 \quad c_2 \quad c_3 \quad c_4 \quad c_5 \quad c_6 \quad c_7]^T \quad (2.7)$$

From inspection, and consistent with findings from other electroadhesive force studies [41], I identify two regions of behavior in dielectric thickness (Fig. 2.4b). I divide the data into thick dielectric and thin dielectric groups and alter Eq. (2.4) to include a distinct dielectric thickness term and constant multiplier for each group, where the cutoff thickness is selected to minimize the combined residual error of the model. The cutoff thickness is 53 μm . The new equation, which also includes distinct constant multipliers for the two groups of dielectric thickness, is

$$F_x = \left\{ \begin{array}{c} \exp(c_1') \\ \exp(c_1^*) \end{array} \right\} \cdot l^{c_2} \cdot w^{c_3} \cdot \left\{ \begin{array}{c} (t_d')^{c_4'} \\ (t_d^*)^{c_4^*} \end{array} \right\} \cdot t_e^{c_5} \cdot V^{c_6} \cdot age^{c_7} \quad (2.8)$$

where c_1' and c_4' are the constant multiplier and dielectric thickness coefficient for the thin subset (t_d'), and c_1^* and c_4^* are the constant multiplier and dielectric thickness coefficient for the thick subset (t_d^*). The linear regression is performed in the same fashion as in Eqs. (2.5)-(2.7), with an additional two columns in the A matrix and two additional coefficients in the x matrix. In the new A matrix, the values in the columns corresponding to c_1' and c_4' are set to 0 for the thick subset data, and the values in the columns corresponding to c_1^* and c_4^* are set to zero for the thin subset data. This formulation separates the effects of dielectric thickness for the two groups and provides a necessary additional degree of freedom for each subset in the form of the constant multiplier, while still considering the effects of all other parameters for both subsets as a single group. A prediction of holding force (in Newtons) for a particular set of design variables can be found by plugging the set of values into Eq. (2.8), ensuring that the units of l , w , t_d , and t_e are all meters, the unit of V is Volts, the unit of age is days, and that the appropriate c_1 and c_4 are selected, given the selected dielectric thickness relative to the cutoff thickness of $53 \mu\text{m}$.

Experimentally-Derived Model of Holding Force

Table 2.2: Fitted model coefficients for Eq. 2.8. The center column gives coefficients derived from the full dataset. The thin and thick subset columns give coefficients derived from the respective subsets of data.

Coefficient	Thin Subset	Full Dataset	Thick Subset
c_1', c_1^*	-14.79		-23.18
c_2		0.9055	
c_3		1.103	
c_4', c_4^*	-0.3829		-1.495
c_5		-0.3642	
c_6		2.612	
c_7		0.2901	

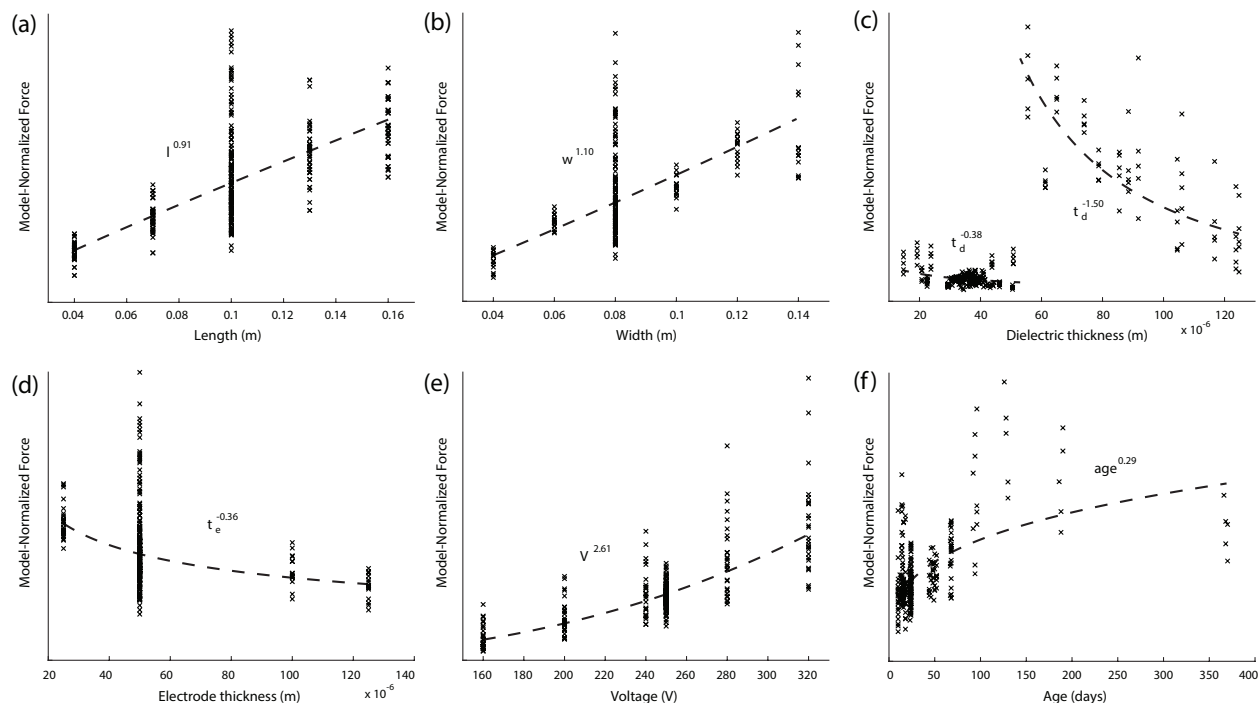


Figure 2.16: Maximum holding force normalized to each model parameter. In each plot, the y-axis value at the origin is zero. a) Force normalized to length. b) Force normalized to width. c) Force normalized to dielectric thickness. d) Force normalized to electrode thickness. e) Force normalized to voltage. f) Force normalized to age.

Providing the linear regression with additional degrees of freedom around dielectric thickness substantially improves the model prediction of holding force, increasing the R-squared from 0.48 to 0.81 (Fig. 2.15). The original model underpredicts the highest measured force data (Fig. 2.15a), an issue that is largely resolved in the modified model (Fig. 2.15b).

By normalizing maximum holding force by the model prediction for all variables but one, that variable's fit can be visualized while accounting for all other effects (Fig. 2.16). The model finds nearly linear increases in holding force as clutch length (Fig. 2.16a) and width (Fig. 2.16b) increase, with model coefficients of 0.91 and 1.1 respectively. Holding force scales as $(t_d^{-1.5})$ for the thick dielectric subset, while the thin dielectric subset is much flatter with respect to force, and is best fitted with $(t_d^{-0.38})$ (Fig. 2.16c). Increasing electrode thickness decreases force as $(t_e^{-0.36})$ (Fig. 2.16d). Clutch voltage has the most dramatic effect on holding force, scaling force as $(V^{2.61})$ (Fig. 2.16e). Finally, increasing clutch age causes a moderate increase in holding force, scaling as $(age^{0.29})$ (Fig. 2.16f). While additional unknown effects

likely contribute to the remaining error, this model does provide useful trends to inform design using the parameters investigated in this study.

2.5 Discussion

2.5.1 Optimal Design Values

Based on the results of the design study, I draw a few main design insights. Maximum holding force scales linearly with area, but increasing area, and width in particular, increases release time. Cutting slits to decrease continuous width greatly alleviates the release time penalty, and area can be increased without increasing release time by stacking smaller area clutches in parallel with one another. This is a critical design insight for applications requiring fast response, and I recommend keeping continuous area low by using slits and multiple clutches. Fast engage times are dependent on good alignment of the clutch plates, which is achieved by controlling clutch plate curvature during fabrication and selecting proper tensioners. Clutches perform best when the total dielectric thickness is between $50\ \mu\text{m}$ and $80\ \mu\text{m}$. I recommend using the $25\ \mu\text{m}$ electrode because it holds more force than the other thicknesses, while having the lowest mass and volume. Finally, applying larger voltages greatly increases force, but dielectric breakdown and space charge impose practical limits on the voltage. Voltages near $300\ \text{V}$ provide a good combination of high force, reliability, and responsiveness.

2.5.2 Comparison of the Empirical Model to Classic Electrostatic Theory

One interesting comparison to my experimentally-derived model is the electrostatic force theory for a parallel plate capacitor, given by Eq. (2.1). While this theory can describe some of the behavior I observed, it does not agree with many of my findings. The experimentally-

derived length and width scaling coefficients of 0.91 and 1.1 compare fairly well with the linear prediction of the electroadhesive clutch theory. A linear fit of the holding force vs. clutch area in Fig. 2.4a results in an R^2 value of 0.94. The slight deviation of these coefficients from a value of 1 may be due to geometric variations between clutches that become more detrimental as the clutch gets wider or longer, such as the position of attachment points. Such variations could impact load distribution, causing sub-optimal loading of regions near the edges of the clutch. The dielectric thickness coefficient of -0.38 for the thin subset deviates substantially from the theory prediction of -2 , indicating that the expected relationship between force and thickness is disrupted by other phenomena, such as breakdown, space charge, or non-uniformity on the micrometer scale. The scaling of dielectric thickness of -1.5 for the thick subset agrees better with theory, but is still lower than expected, potentially due to some of the same phenomena. The model finds a coefficient of 2.6 for voltage, which is somewhat higher than the theory prediction of 2. This deviation is likely caused by improved adhesion and elimination of the air gap between the clutch plates at higher voltages, which would decrease the effective dielectric thickness and increase the charge in the electrodes. This larger value may also be due to the longer activated time of tests with large holding force, as discussed in the Holding Force Design Insights subsection.

In a more pronounced disagreement with the model and data, the electrostatic theory underpredicts the overall magnitude of force produced in the clutch by a factor of ten. Fitting the thick dielectric data to electrostatic force theory with the coefficient ϵ as the free variable and the measured $\mu = 0.63$ (see *Coefficient of Friction Testing* in the Appendix) produces an unrealistic dielectric constant of about 270, compared to my measured dielectric constant values of 15-20. Additionally, the electrostatic force theory cannot account for the effects of electrode thickness and age. These disagreements between my experimental results and electrostatic force theory imply that this theory is not adequate for either qualitative or quantitative predictions of clutch performance, underscoring the importance of this and future experimental work.

The electrostatic force model relies on the assumption of dry Coulombic friction, which is inadequate for describing the adhesion interactions of thin polymer films. Other physical phenomena that may alter the critical shear force include van der Waals interactions, stiction effects, and geometric confinement [62, 63]. The impact of these other effects has been shown in previous work, including for electrostatic adhesion. [41] observe increasing critical shear force in their soft electroadhesives as the ratio of width to thickness increases, which agrees with my finding that force increases as electrode thickness decreases for a constant width. [41] also measure critical shear forces up to 3 times higher than predicted by electrostatic force theory for the thinnest geometries. The authors do find that for certain width-to-thickness ratios, the measurements agree with electrostatic force theory. However, these correspond to aspect ratios that are 100 to 1000 times smaller than the range tested in this paper. I am not able to make quantitative comparisons to this work because of differences in the materials, geometry, and methods, but this previous work finds similar trends to my findings. Given this set of previous work, it is not unreasonable and perhaps not even surprising that the clutch outperformed the electrostatic force theory.

Clutch Age:

The maximum holding force of the clutches increases as the clutches age. This may have to do with changes in the dielectric layer over time. One contributor may be continual evaporation of solvent that was not fully baked out of the dielectric during fabrication. It is possible the solvent decreases the overall dielectric constant of the insulating material, and makes the clutch more susceptible to space charge, which I have observed can also decrease the maximum holding force. Further investigation of this phenomenon could inform changes to the fabrication process to compensate for this effect and achieve better performance of the clutches immediately after fabrication.

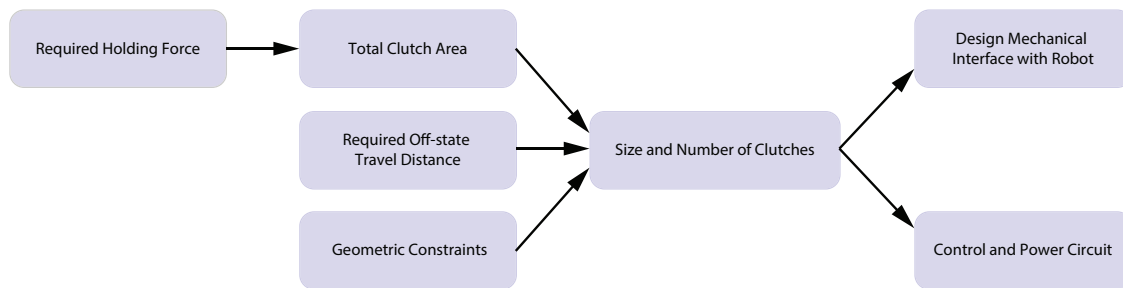


Figure 2.17: Design flowchart for electroadhesive clutch implementation.

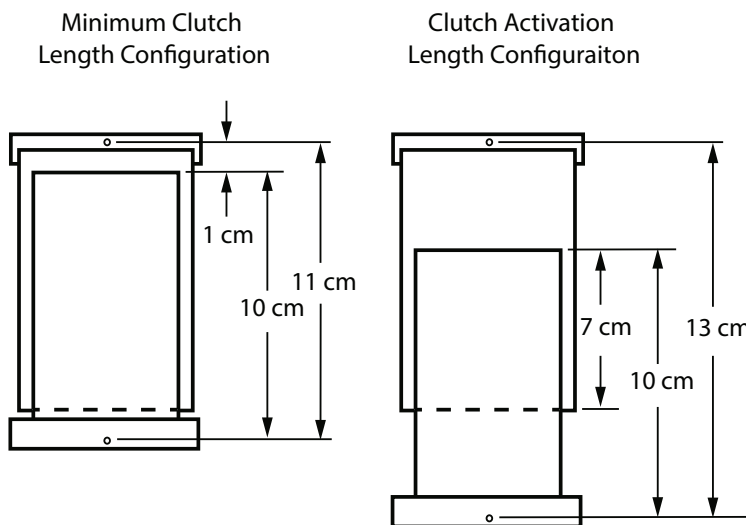


Figure 2.18: Clutch length diagram.

2.5.3 Design Example

Appropriate clutch parameters can be selected based on the required holding force, total clutch travel, and the available space (Fig. 2.17). First, the designers must determine the highest force that will be exerted by the clutch during operation. For example, in a lower-limb exoskeleton or legged robot application, the designers might place the clutch in series with a spring and stretch it to a maximum force of 1000 N. Using a factor of safety of 2, and the measured value of 23 kPa of shear pressure for a clutch with 65 μm dielectric thickness at 320 V, I calculate that 870 cm^2 of clutch area would be required. While this value may seem high, it can be accomplished in a compact device by stacking clutches in parallel with one another, as described later in this example. The next consideration is the required off-state travel distance of the clutch. In the hypothetical application, the designers might

require 3 cm of travel in each direction from the neutral configuration during the off state. Next, geometric constraints must be taken into account. For the hypothetical device, the total length between the clutch attachments in the neutral configuration might be 14 cm. This would mean the clutch must shorten to a length of 11 cm, and lengthen to a length of 17 cm. Factoring in 1 cm for the carbon fiber bars, this means the individual clutch plates could not be longer than 10 cm, or they would begin to buckle when the clutch is at its shortest length. Here I define the clutch plate length as the distance from the attachment point to the edge of the clutch, as shown in Fig. 2.18. In the hypothetical application, the designers may determine that they would typically want the spring to engage at a clutch length of 13 cm. The corresponding overlap length x can be determined using the equation

$$x = 2l_{cp} - L_t \quad (2.9)$$

where l_{cp} is the clutch plate length, and L_t is the total clutch length. Using clutch plates with individual lengths of 10 cm yields an overlap length of 7 cm. For the hypothetical application, the designers might assign an 8 cm wide space for the clutches. To allow space for tensioner spring attachments, the designers could then choose a clutch overlap width of 7 cm. This would correspond to an overlap area of 49 cm² per clutch, meaning that 18 clutches of this size would be necessary to transmit the required force.

To inform the sizing of electrical components, the designers could now estimate the steady-state power consumption of the clutches. If I assume the clutch is activated once per second with a duty factor of 50%, and the clutch has a dielectric thickness of 65 μm and an applied voltage of 320 V, the power consumption is about 17 μW per 1 N of force. Based on this scaling, the designers would estimate 34 mW of continuous power consumption. This means the designers would need to select a high-voltage transformer capable of outputting at least 34 mW continuously (for example the XPPower AG04N-5 DC-DC converter, which has a capacity of 1 W). Additionally, the designers should place a capacitor in

parallel with the transformer to reduce the peak current draw from the transformer and provide a good source for rapidly charging the clutches. The parallel capacitor should be relatively large compared to the total capacitance of the clutches (for example the Rubycon 400PX4.7MEFCTA8X11.5, which has a capacitance of $4.7 \mu\text{F}$). All of the clutches could be controlled by a single control circuit requiring two high voltage relays (for example the Toshiba TLP222G-2, which can switch at up to 350 V). Together with low voltage transistors, these electronic components would weigh less than 10 grams and occupy less than 5 cm^3 .

Finally, the mechanical interface of the clutches with the robot structure would need to be considered. In the example, two clutch plates could be placed on each carbon fiber bar, for a total of 9 bars per side. The bars could be 0.8 mm thick. Allowing for a 1 mm space between bars, the total thickness of the assembly would be 1.6 cm. It is important that the mounting allow for small rotations of the clutches during loading, as well as rotation about the mounting bolt to allow the clutches to self-align into a state of pure tension. The carbon fiber bars should not be compressed together, and each bar should be able to move through a small range freely and independently.

The designers could approximate the expected mass of the clutches with the measured ratio for this dielectric thickness and voltage, which is 0.052 grams per 1 N, resulting in an expected mass of 0.104 kg. The final assembly would have dimensions of $14 \text{ cm} \times 8 \text{ cm} \times 1.6 \text{ cm}$, corresponding to a volume of 179 cm^3 .

By comparison, a conventional clutch with comparable functionality for an exoskeleton or walking robot would have much higher weight and power consumption. An electromagnetic rotating tooth clutch capable of transmitting $108 \text{ N}\cdot\text{m}$ would weigh about 1.5 kg, occupy a volume of 250 cm^3 , and consume 30 W of power when active [64]. While the volume and responsiveness of this clutch would be comparable, it would weigh about ten times more and consume about five hundred times more energy than the electroadhesive clutch. Using a smaller clutch and a gearbox could also be problematic, because backdriving the gearbox would lead to undesirable torques due to the reflected inertia of the clutch and gearbox.

For example, using a 100:1 gearbox would require the deactivated clutch to accelerate 100 times faster than the robot joint, leading to a reflected inertia of 10,000 times the original clutch inertia. In addition, any damping in the clutch during the off-state would be greatly magnified. Finally, planetary gearboxes capable of outputting 100 N·m of torque commonly weigh on the order of 1 kg, and lighter alternatives such as lead screws are typically non-backdrivable. Achieving comparable functionality with a conventional electrically controllable clutch is simply not practical for most robotics applications, in terms of weight or energy consumption.

2.5.4 Applications

Electroadhesive clutches can provide many benefits while requiring only minimal added mass and power consumption. In their simplest implementation, clutches can lock degrees of freedom to reduce energy cost, enhance safety, or adjust passive dynamics. Many additional functionalities can be achieved by employing multiple clutches in various configurations [65]. By placing a clutch in series with a spring, a passive force element can be engaged when desired, with a controllable set point [29]. Adding more clutched springs in parallel provides adjustable stiffness [66]. An actuator can operate with adjustable gear ratios or series stiffness when placed in series with clutched gearboxes and springs [67]. Attaching multiple clutches to a single spring can enable strain energy storage, or provide a means to route energy between multiple degrees of freedom [30]. Even more complex systems of clutches, springs, and motors can provide many operation modes and functionalities [68, 69, 65]. These and other creative implementations could be applied to a broad range of applications, some examples of which I describe below.

Lightweight Mobile Robots:

A particularly advantageous use case for electroadhesive clutches is the actuation of bipedal walking and running robots. Many of these robots seek to achieve spring-like leg behavior,

with small amounts of energy injection or minor force profile variations for controlling balance [70, 71]. Because leg forces are high during stance, large motors or hydraulic pistons are commonly used [72], even though the energy requirements for steady walking on level ground can be quite low [73, 45]. Additionally, fast low-force movement during the swing phase is desirable, leading to low gear ratios and larger actuators [74] or reductions in peak speed when actuator limits are encountered [75]. One solution is to place a spring in parallel with the actuator [76], but this limits versatility and increases the difficulty of some movements [77]. Using clutches to engage parallel springs only during desired periods, such as the stance phase of walking or running, would offload active elements, reducing their size or improving overall performance. Traditional clutches are too heavy and power-hungry to be practical for this purpose. By contrast, electroadhesive clutches and springs weighing just hundreds of grams and consuming less than one Watt of electricity can produce thousands of Newtons force while storing and returning hundreds of Joules of mechanical work (extrapolating from [66]). In addition, many robots could potentially incorporate clutches with relatively modest design changes. This actuation strategy could dramatically reduce the power consumption of existing robots and minimize the size and weight of actuators in future designs.

Implementing effective control strategies is a significant challenge for mobile robots, and limitations in possible actuator behavior contribute significantly to this problem [78]. Actuators with stiff transmissions can achieve high precision movement, but are typically non-backdrivable and can be dangerous to humans [8]. Series elastic actuators, on the other hand, can execute torque control and interact with humans more safely, but sacrifice precision [79]. A variable stiffness transmission based on electroadhesive clutches could enable mode-switching between a stiff connection for precise position control and a selectable series elasticity for enhanced torque control [31, 80]. For example, a humanoid robot's arm could perform precision manufacturing tasks with high repeatability using a stiff connection and position control, and change modes to perform tasks in conjunction with humans

more safely and naturally under torque control. This transmission would be lightweight, and could change modes under load or in any configuration. Using a variable gearbox based on electroadhesive clutches could further enhance capability by expanding the possible torque/speed regime of the actuator, which can improve performance [48]. Lightweight and responsive clutch-based transmissions could thereby improve the efficiency and capabilities of many mobile robots.

Exoskeletons, Prostheses, and Wearable Devices:

For exoskeletons and prostheses, low weight is a critical factor in achieving good performance. Adding mass to distal locations on the body causes a substantial increase in metabolic energy cost [81]. Many existing devices have incorporated clutches or similar mechanisms in an attempt to reduce motor and battery size. For example, passive exoskeletons employing clutches and springs have assisted humans with walking [24, 82] and weight-lifting tasks [83]. Active exoskeletons and prosthetic limbs have incorporated variable stiffness joints and variable transmission ratios to adapt to user behavior [84, 85, 86]. Clutch-like adjustments in prosthetic foot stiffness have been used to make step-by-step adjustments in ankle torque to enhance balance [87], and in exoskeleton damping to aid rehabilitation [88]. Assistive devices have used springs and multiple clutches to harvest energy from one joint to return it later or transfer it to another joint [89, 90, 30, 91].

Energy-harvesting knee exoskeletons have used clutches to avoid interference during non-harvesting movements [92]. Clutches have been used as mechanical fuses, slipping when forces exceed a predetermined value to prevent a device from injuring the user [93]. In each case, electroadhesive clutches could help overcome limitations imposed by the mass and energy consumption of traditional clutches or the constraints on versatility and controllability of mechanism-based approaches.

As the field of robotics continues to expand into non-industrial settings, electroadhesive clutches could help shape the development of assistive robots worn by people. Devices us-

ing online optimization [94, 95, 96] might particularly benefit from the versatility of smart transmissions and actuators enabled by electroadhesive clutches.

Industrial Robotics:

Robots in manufacturing or other factory settings could also benefit from lightweight, low-power electroadhesive clutches. Many industrial robot arms require large actuators and high energy expenditure, in part to support their own weight. Attaching electroadhesive clutches and springs to joints could reduce the loads on actuators by providing gravity cancellation [97, 98]. More energy savings could be achieved by actively adjusting the gravity cancellation set point [99, 100]. Incorporating many clutched springs in parallel with another would provide adjustable stiffness, allowing the gravity cancellation to adapt to changing weight at the end effector as parts are picked up and placed. Offloading actuators in this way could significantly reduce energy consumption or motor size and cost [101]. Clutched springs could also store and return strain energy to quickly accelerate or decelerate a robot arm without requiring active actuator work [102, ?]. Electroadhesive clutches could be beneficial in gripping or manipulation tasks, where they would lock an end effector after grasping an object to hold it at very low energy cost [103, 42]. Introducing lightweight, low-power clutches to industrial settings could enable energy and cost savings with relatively minimal changes in hardware and manufacturing methods.

Applications Summary:

Incorporating electroadhesive clutches into actuator schemes would improve actuator performance and versatility while decreasing weight and power requirements. Electroadhesive clutches and springs can perform the energy-neutral portion of an actuation task, support body weight, or efficiently route force and energy across many degrees of freedom. Electroadhesive clutches can also expand actuator functionality through variable stiffness or variable mechanical advantage transmissions. By providing high force transmission and

responsiveness at a fraction of the weight and power requirements of traditional clutches, electroadhesive clutches dramatically expand the possibilities for implementing responsive and adaptive hardware in robotic actuators.

Limitations:

Our electroadhesive clutch design does have some drawbacks. The travel distance is constrained by the overall length and overlap length of the clutches, as well as the force in the tensioners in different configurations. Additionally, the clutch could short in wet environments, necessitating a water-resistant casing for some applications. The clutch also has a limited temperature range of operation determined by the materials, and likely has performance dependent on temperature and humidity, although I did not investigate such a dependence in this study. While these factors hinder use in some implementations, I expect electroadhesive clutches will be an excellent option for a wide range of robotic applications.

2.5.5 Future Work

Future investigation of clutch performance should include different loading rates, such as impulse loading on one extreme and creep detection on the other. Surface characterization could contribute to understanding the friction characteristics and true surface contact area achieved. Additional experiments should be conducted to understand the different mechanisms of force development at the interface, for example by systematically varying the surface roughness of the dielectric layers. Further performance improvements could also come from investigation of the mechanism behind the clutch width's effect on force and release time. Finally, more systematic investigation of the effect of tensioner force and clutch curvature on clutch holding force and engage time should be conducted to produce quantitative design guidelines.

2.6 Conclusions

Electroadhesive clutches achieve orders-of-magnitude improvements in mass and power consumption compared to conventional clutches. In this work, I report a systematic investigation of electroadhesive clutch performance. The results of the study inform the design of clutches for a wide variety of usage cases according to their force, responsiveness, and power consumption requirements. Electroadhesive clutches have the potential to make hybrid actuation and passive actuation more feasible for robots in terms of weight, power consumption, and bandwidth.

Chapter 3

A lightweight, low-power electroadhesive clutch and spring for exoskeleton actuation

Abstract

In this Chapter, my goal was to demonstrate the versatility and reliability of the electroadhesive clutch in a challenging robotic application. I placed the clutched spring onto an ankle exoskeleton and controlled the clutch to provide assistive torques during stance and to disengage during swing. As a further demonstration, I showed the ability to electronically choose between many stiffnesses by placing clutched springs in parallel. The electroadhesive clutched spring showed significant improvements in force density and force per unit energy consumption compared to conventional clutches.

This work appears in: S. Diller, C. Majidi, and S. Collins, "A lightweight, low-power electroadhesive clutch and spring for exoskeleton actuation," in *Proceedings of the IEEE International Conference on Robotics and Automation (ICRA)*, 2016, pp. 682-689

3.1 Motivation

Exoskeletons worn on the ankle have been widely explored for tasks such as rehabilitation, locomotion assistance, and human load-bearing augmentation [104]. These devices can generally be divided into two groups: tethered and untethered exoskeletons. Tethered exoskeletons can keep actuators, controllers, and energy sources separate from the body, which dramatically reduces the weight and complexity of the end effector worn by the human [105, 106]. This allows researchers to focus on discovering appropriate control strategies, independent of the specific design of a real-world device [107]. These tethered systems have achieved dramatic reductions in the human metabolic cost of walking, and have served as important testbeds for control strategies and biomechanics experiments [108, 95, 109]. However, these systems are restricted to use in the lab. While they can inform the design of mobile devices, they cannot themselves be used in everyday life.

Translating these exciting results to untethered designs has proved challenging. Metabolic reductions have been shown in positive-work mobile exoskeletons [110, 111], but these devices are heavy and have limited range. As opposed to using positive-work actuators such as motors, incorporating a mechanical locking clutch and spring into an ankle exoskeleton gave a metabolic reduction and resulted in a device that is much lighter and uses no energy [24]. The behavior of this device was extremely limited, however, because the mechanical clutch and spring were optimal only for level-ground walking at a particular spring, and could not actively change their characteristics.

My goal was to replicate the functionality of this unpowered exoskeleton with a controllable electroadhesive clutch and spring that maintain the lightweight and low-power nature of the device. I also wanted to show that putting many electroadhesive clutched springs in parallel could allow a controller to choose between discrete stiffnesses on each loading cycle. An exoskeleton with many electroadhesive clutched springs in parallel could actively change its characteristics to optimally assist a variety of activities such as running and stair-climbing.

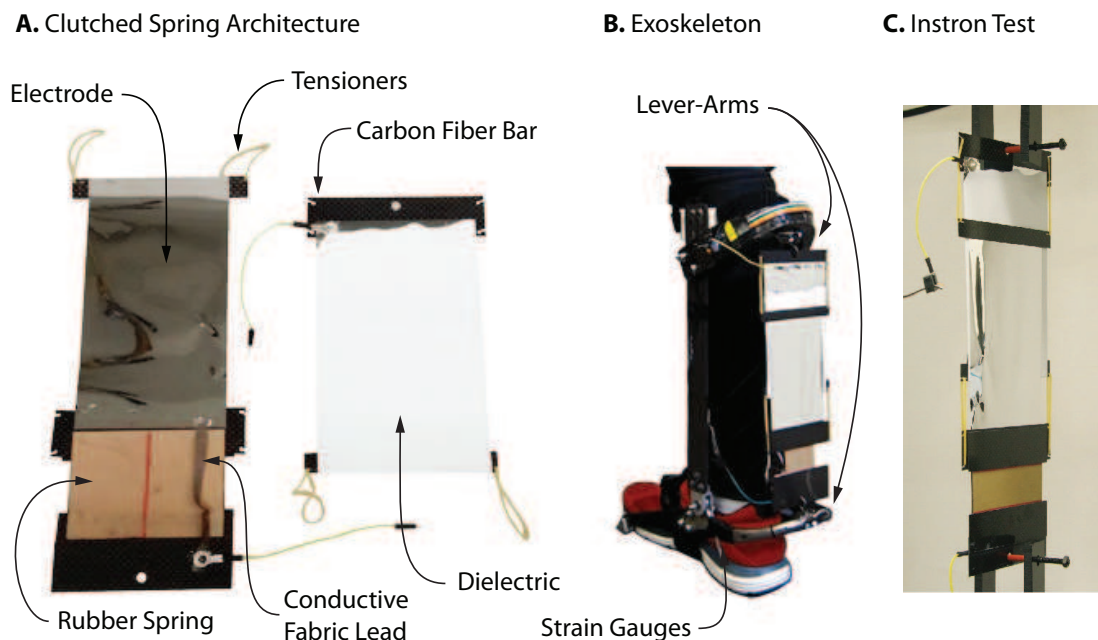


Figure 3.1: Clutched spring components and construction. a) The clutch develops force when a voltage is applied across the electrodes, which are separated by a dielectric insulator. b) The clutch is mounted in series with a rubber spring on the ankle exoskeleton. c) The properties of the clutched spring are measured using a materials testing machine.

3.2 Methods

The clutched spring was connected to the lever arms of the exoskeleton using eye hooks (Fig. 3.1). The exoskeleton was controlled by a dSpace control system (DS1103, dSPACE, Wixom, MI). A high-voltage power supply (Model PS375, Stanford Research Systems, Sunnyvale, CA) provided 240 V DC. At maximum plantarflexion during early stance, the controller recorded the ankle angle and activated the clutch. The clutch then transmitted force as the spring stretched and recoiled during the stance phase. Once the recorded ankle angle was reached during late stance, indicating that the slack length of the spring had been reached, the clutch was deactivated to allow free rotation of the ankle during swing. Walking tests were conducted on a treadmill at $1.25 \text{ m}\cdot\text{s}^{-1}$ with one subject. 150 consecutive strides were taken during which the clutch performed as desired. Data was divided into individual strides, beginning with exoskeleton-side heel strike. Performance characteristics, including torque, power, efficiency, work, and stiffness were calculated for each step,

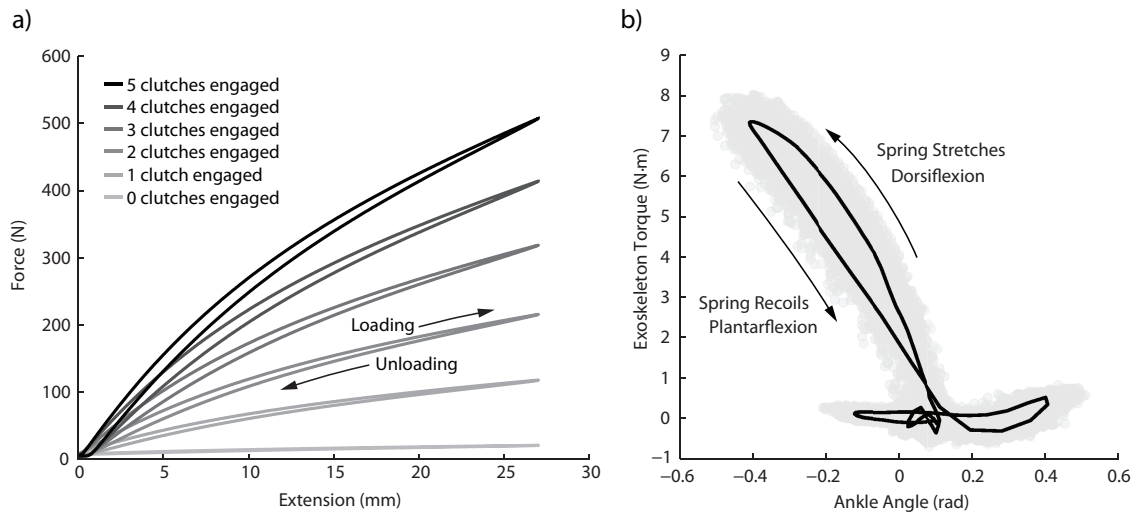


Figure 3.2: a) Placing five clutched springs in parallel allows the overall device stiffness to be selected each cycle. The maximum device stiffness is 36 times higher than the minimum device stiffness. b) The exoskeleton torque-angle curve during walking displays two distinct slopes, corresponding to the exoskeleton stiffnesses during the activated and unactivated clutch states. More energy loss was observed during walking than in benchtop tests, likely owing to acceleration of the ankle lever arm of the exoskeleton during plantarflexion.

then averaged. The stiffness selection demonstration was performed on a materials testing machine (Instron 5969, Instron, Norwood, MA). During each condition, voltage was applied to a fixed number of clutches throughout loading and unloading. The number of clutches activated was varied between conditions.

3.3 Results

The maximum torque exerted by the clutched spring on the exoskeleton during walking was 7.37 ± 0.04 N·m. The linearized exoskeleton stiffness was 14.7 ± 0.9 N·m·rad⁻¹. The efficiency of the clutched spring on the exoskeleton during walking was $81.9 \pm 3.6\%$. The maximum instantaneous power was 25.6 ± 2.4 W during push-off. The clutched spring performed 2.61 ± 0.33 J of negative work and 2.14 ± 0.29 J of positive work on each step. The fraction of time the clutch was activated during walking was $D = 0.524$, and the stride frequency was 0.873 Hz. This resulted in a power loss from leakage current of 0.05 mW, and an average total electrical power consumption of 0.59 ± 0.14 mW. Five clutched springs

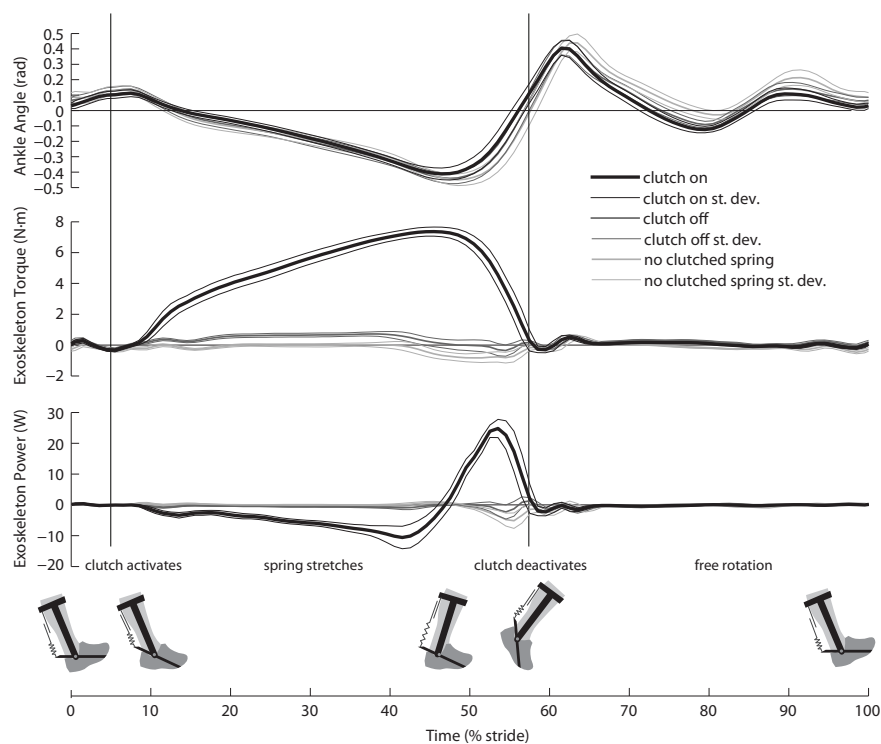


Figure 3.3: Ankle angle, measured torque, and exoskeleton power during the gait cycle. The “clutch on” data is from walking with the clutch activated during stance, between the vertical lines. The “clutch off” data is from walking when the clutch was deactivated throughout the gait cycle. Positive torque in this data is produced only by the tensioning springs and motion artifact from the inertia of the lever arm. The “no clutched spring” data is from walking in the exoskeleton without any clutch attached to the spurs.

placed in parallel produced a peak force of 501 N with all clutches engaged and a peak force of 14 N with no clutches engaged, or a factor of 36 change in stiffness. The efficiency of the clutch-spring devices in the materials testing machine was $94.7 \pm 0.1 \%$.

3.4 Discussion

Characterization of the clutch and spring demonstrated predictable and reliable behavior. The efficiency of the rubber spring was almost 95%, comparable to metal coil springs. The clutch displayed no distinguishable slipping, evident in force-displacement curves and in the match between clutched spring efficiency and the efficiency of the spring measured without the clutch. Stiffness was controllably changed by selectively engaging a subset of clutched

springs acting in parallel (Fig. 3.2). A stiffness ratio of 36 was demonstrated in a range useful for assisting walking, with very low power consumption of less than 1 mW. Improved resolution could be achieved using springs of differing stiffness, increasing exponentially with the number of clutched springs. For example, five springs with power-of-two ratios in stiffness would yield 32 evenly distributed stiffnesses. Using this approach with electroadhesive clutches could enhance performance and add functionality in applications using rigidity tuning devices [37, 112] or variable stiffness actuators [65, 113, 114, 115]. The clutched-spring exoskeleton performed well during walking. The clutch consistently engaged the spring during the stance phase, and disengaged during swing to allow free rotation of the ankle (Fig. 3.3). No slipping was observed during 150 continuous steps of walking. The observed variations in the torque vs stride curve are typical of natural step-to-step variations during walking. This result demonstrates that the electroadhesive clutch can operate reliably in a dynamic and challenging application.

The electroadhesive clutch achieved significant improvements in mass and power consumption compared to other types of clutches. Such comparisons are imperfect, because electromagnetic and magnetorheological clutches are usually rotary, so I have based comparisons on estimates of the mass and power required to provide similar functionality. High-performance electromagnetic clutches provide one point of comparison. The best reported performance for a similar application is found in [27], which describes a clutch in series with a spring in a lower-limb prosthesis. During the stance phase of walking the clutch held one end of the spring stationary, allowing it to passively produce torque. Comparable performance would be achieved by stacking electroadhesive clutched springs in parallel, adding a pair of electrodes to each spring, and doubling the spring thickness. The electroadhesive clutch system would produce the same torque with a third of the mass of the electromagnetic clutch system, and the power consumption would be 750 times lower. The electroadhesive clutch-spring system would also have the added benefit of discretely variable series stiffness. Another point of comparison are high-performance magnetorheological clutch systems. The

best reported performance is provided by [35]. The same torque would be produced with 32 g of clutches and 162 g total mass, corresponding to 30 times less mass. Power consumption would be 2.95 mW, a factor of 340 reduction. The magnetorheological clutch has the added benefit of controlled damping, which has not yet been demonstrated with this electroadhesive clutch. The electroadhesive clutch even achieves a weight savings compared to passive clutches. Similar functionality is described by [24], which presents a passive ratchet and pawl clutch connected to a metal coil spring on an exoskeleton. Comparable performance would be achieved with a three-fold mass reduction, and would come with the advantage of electrically controlled engagement and selectable stiffness. These comparisons illustrate the potential for the electroadhesive clutch to achieve significant weight and power savings while offering the ability to quickly and controllably change stiffness without interrupting operation.

3.5 Conclusions

My goal in this chapter was to demonstrate the use of a lightweight and low-power electroadhesive clutch in selectable stiffness and exoskeleton applications. The electroadhesive clutch tested here had a total mass of 11 g, transmitted 100 N of force, and consumed only 0.6 mW of electricity during walking. This is a three-fold improvement in weight and a factor of 340 improvement in power consumption compared to the best conventional clutches used in similar applications. Placing several clutch-spring elements in parallel allowed stiffness selection, enabling a 36-fold increase in stiffness. The electroadhesive clutch-spring device controllably and reliably produced torque on the ankle exoskeleton during walking. This technology could improve the performance of exoskeletons, prostheses, and walking robots by allowing the use of many separately-controlled clutches while achieving low mass and power consumption.

Chapter 4

Design, control, and characterization of an energy recycling actuator based on parallel electroadhesive double clutched springs

Abstract

Lightweight and high-efficiency energy harvesting actuators could dramatically reduce the overall power consumption of actuators for high-performance robots. In this chapter, I present a force-controllable energy recycling actuator based on electroadhesive double clutched springs. First, I detail the proposed energy harvest and return system and investigate the energy efficiency of single clutched spring units with a theoretical model and hardware experiments. I then describe the design heuristics and optimization I used to perform the detailed design of the full energy recycling actuator. Next, I investigate a control strategy for the actuator in simulation, and use an evolutionary optimization technique to tune the

This chapter is ongoing unpublished work performed in collaboration with Erez Krimsky.

control gain values. Finally, I characterize the actuator prototype and perform a preliminary test of force tracking with multiple double clutched spring units.

4.1 Introduction

When most actuators perform negative work movements, the energy is dissipated to heat and wasted. If this energy could instead be harvested [92], stored and returned to the actuator during positive work movements, the overall energy consumption of the system could be significantly reduced. In fact, zero net work tasks could in theory be performed with no required energy cost. For actuators that regularly perform negative work, incorporating energy harvesting and return could dramatically reduce the power use and size of actuators, leading to lower overall robot mass and power consumption.

Electric motors and electroactive polymer actuators are capable of both positive work actuation and negative work energy harvesting [4, 116]. By storing the energy in their existing batteries, these actuators can then output the harvested energy with any prescribed force-displacement profile. However, the full-cycle efficiency in real-world scenarios is generally below 50% [4, 116].

An alternative method is to use a clutched spring to harvest and return energy [24, 117]. During a negative work movement, the clutch engages the spring, which stretches and stores the energy in the form of strain energy. The spring can then return the energy during a positive work movement. The round-trip efficiency of a spring can be very high (>95%). However, when only one spring is used, the force-displacement profile during work input or output cannot be actively controlled. This configuration constraint is undesirable in many applications where precise control is necessary.

My goal in this chapter is to combine the generic energy input-output and controllability of the motor energy harvesting with the high efficiency, high energy density, and low monetary cost of rubber springs. By using many double clutched springs in parallel with one

another, energy can be harvested, stored, and returned with discrete force control and arbitrary force-displacement input-output profiles. The electroadhesive clutches are particularly enabling in this application, as all other actively controllable clutches are far too heavy, large, and power-hungry to create a compact and efficient set of double-clutched springs.

4.2 Double-Clutched Spring Characterization

4.2.1 Introduction

A significant limitation of current robotic actuation is that conventional energy regenerative systems are impractical for small, lightweight implementations. As a result, efforts to harvest and return energy have relied on custom hardware implementations that have configuration dependencies and a very limited range of behaviors. I envision an energy harvesting and return system that is as versatile as an automotive brake energy regeneration system and that is easily implemented in a variety of lightweight robotics applications. Using my lightweight, low-power electroadhesive clutches, I propose in this chapter a device that can harvest, store, and return movement energy with precise control and at high efficiency.

As illustrated in the legend of Figure 4.1, I can attach electroadhesive clutches to a rigid frame and moveable output, and connect both of these clutches to a single spring. When the spring is clutched to the output (Fig. 4.1a), changing the output position will have two effects. First, the force exerted by the spring will change, increasing if the output extends, and decreasing if the output contracts. Second, the energy stored in the spring will change. If the output extends, the spring will perform negative work on the output and store the strain energy. When the output contracts, the the spring performs positive work and returns the energy to the output. When the spring is clutched instead to the frame, the stretched spring can retain its energy while the output moves freely. With this configuration, the spring can be clutched to the frame, the output, both, or neither. During

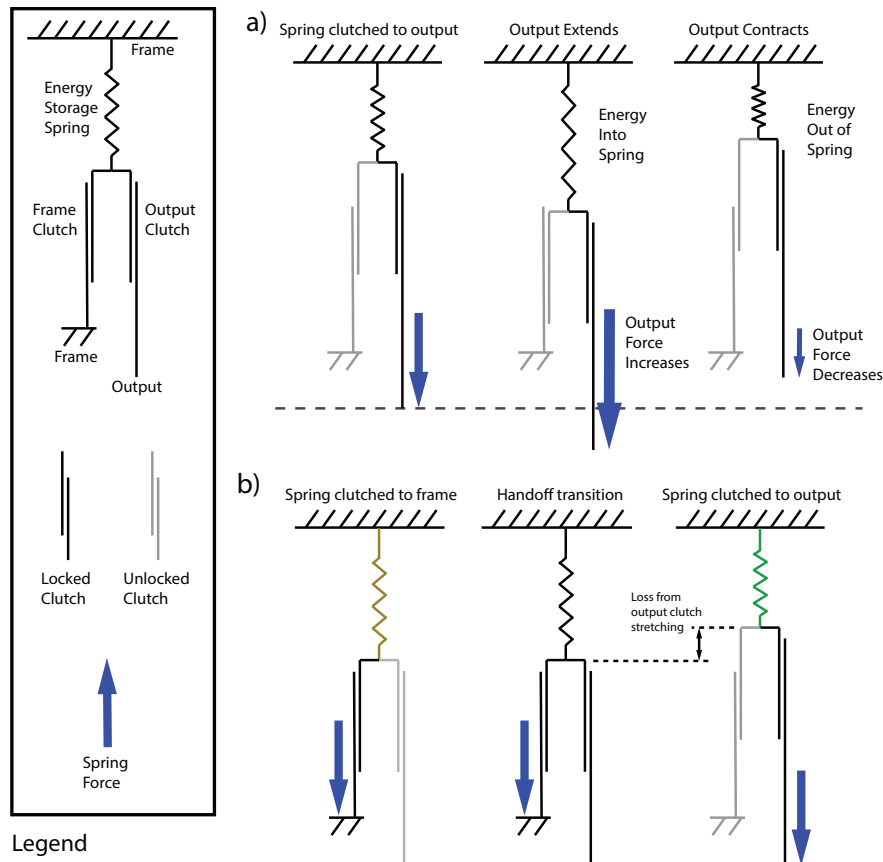


Figure 4.1: Double-Clutched Spring Operation. A rubber spring is attached on one side to a rigid frame, and on the other to two clutches, a frame clutch and an output clutch. The frame clutch is attached on the other side to the rigid frame, and the output clutch is attached on the other side to the output load. a) When the spring is clutched to the output, the output displacement is coupled with the spring, which will store and return mechanical energy. b) An illustrated handoff of the spring from the frame to the output. In the first panel, the spring is clutched to the frame with the output clutch off. During the handoff transition, the frame clutch remains on while the output clutch engages. Finally, the frame clutch turns off and the spring is clutched solely to the output.

functional operation, clutching to both or neither of the frame and output for significant periods of time is not useful, so I am only interested in switching between the spring being clutched to only the frame or only the output.

The real versatility of this configuration is realized when multiple double-clutched springs are placed in parallel with one another on the same frame (Fig. 4.2). When all of the springs have some stretch, the force exerted on the output can be controlled simply by switching the load path of each spring through the clutches between the frame and output. The possible force on the output is limited to one of a few discrete values, but the number of possible forces

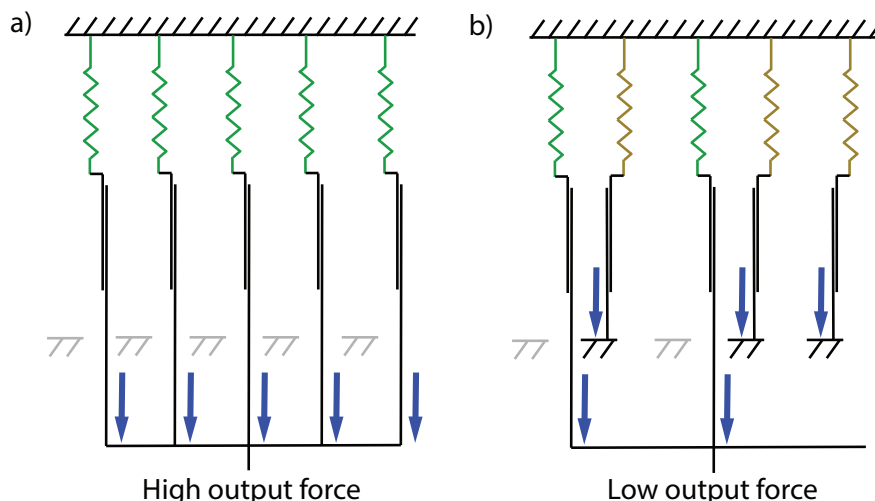


Figure 4.2: Force Control with Double-Clutched Springs in Parallel. a) When all of the pre-loaded springs are clutched to the output, the output observes the sum of their forces, which results a high force value. b) The force on the output can be quickly changed by handing off three of the springs to the frame, leaving just two springs exerting force on the output. With efficient handoffs, the force and energy in the springs are preserved while they are attached to the frame, to later be handed off back to the output.

increases dramatically as more parallel clutched springs at different forces are added, approaching continuous force control. A system with many clutched springs can theoretically produce any arbitrary force-displacement profile within its force and displacement limits, given that the profile is zero-net work on average. This condition encompasses many cyclic tasks, and a hybrid system including my energy recycling actuator and a positive work actuator could operate extremely efficiently.

However, operating even one double-clutched spring is a challenging task and merits experimental study. Specifically, handing a spring off between the frame and output is difficult when the spring is stretched, as its natural tendency would be to spontaneously recoil if the total force in the clutches falls below the spring force, even for an instant. This necessitates that both clutches be on for some time during a spring handoff between the frame and output in either direction, as illustrated in Figure 4.1b. This gives the activating clutch a chance to develop its load bearing capacity before the other clutch deactivates. I call this time the handoff overlap time. Additionally, there is an inefficiency during handoff due to the need to stretch the new clutch connection when establishing the new load path. My

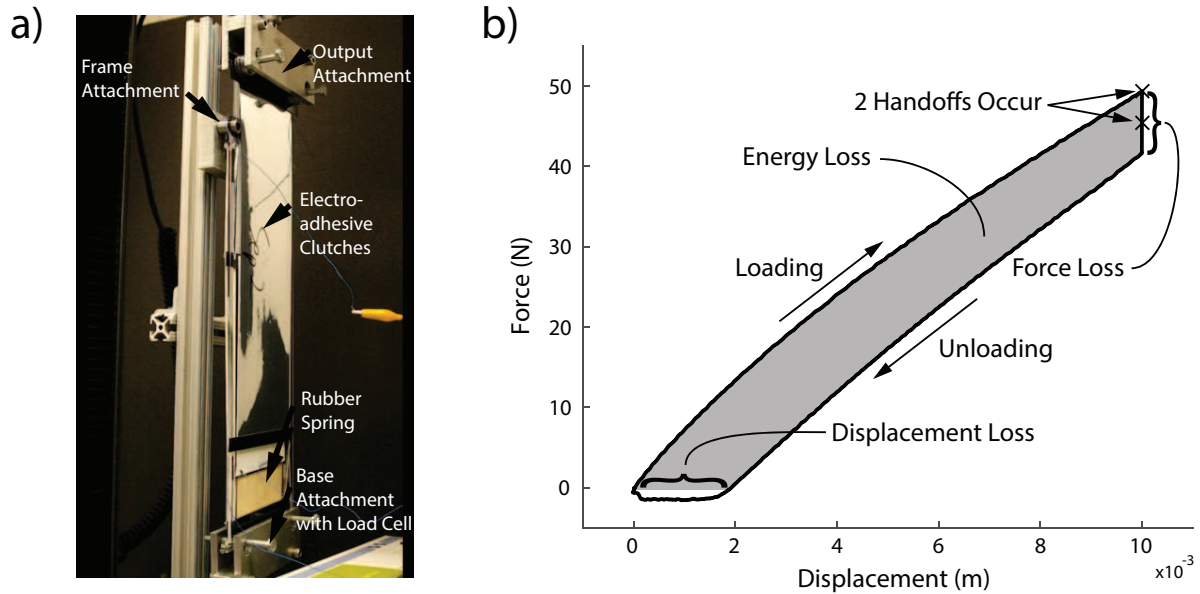


Figure 4.3: Handoff Inefficiency Characterization Methods. a) The double-clutched spring in the custom materials tester mounting. b) During handoff testing, the spring first is clutched to the output and extended. Then the spring is handed off twice, first to the frame and then back to the output while the output holds a constant position. The output is then returned to the original position. The handoff inefficiency due to clutch stretching can be characterized as a loss in spring force, a loss in spring displacement, or a loss in the spring's stored strain energy.

goal in this study is to understand the effect of design and operation decisions on the ability to reliably conduct handoffs and on the magnitude of this handoff inefficiency. During these tests, I varied the spring stiffness, handoff overlap time, and force magnitude during the handoff, and observed the resulting inefficiency and prevalence of clutch slipping. I also compared the results to the predicted behavior based on a theoretical model.

4.2.2 Methods

The clutches were fabricated using the methods described in Section 2.2. The rubber springs were made separately by laser cutting from a rubber sheet and gluing to carbon fiber shims. Bolt holes were drilled in the carbon fiber, and a small bolt was used to connect the spring to the clutches, allowing the stiffness of the clutched spring to be quickly changed by swapping out the spring.

The handoff efficiency tests were conducted on a materials testing machine (Instron

5969, Instron, Norwood MA) with custom-made clamps and frame structure (Fig. 4.3a). Displacement from the analog out of the materials tester and force from a load cell (LC201-100, Omega, Norwalk, CT) located at the base attachment were measured at 5000 Hz by a control hardware system (DS1103, dSPACE, Wixom, MI). The displacement and force data were both passed through a 10 Hz low-pass two-way filter in post-test processing. The high voltage was supplied by a high voltage power supply (Model PS375, Stanford Research Systems, Sunnyvale, CA), and the clutch control circuit was activated by the control hardware system.

To begin the handoff test, the output clutch was engaged, and the materials tester displaced the output connection at a rate of 180 mm/min (Fig. 4.3b). Once a predetermined displacement was reached, the first handoff was initiated by engaging the frame clutch. The controller then waited for the prescribed handoff overlap time to elapse before disengaging the output clutch. After waiting about 5 seconds, the controller then initiated the second handoff by re-engaging the output clutch. Once the handoff overlap time passed, the frame clutch was disengaged. After about another second, the materials tester returned the output to the original position at the same velocity.

The force drop was calculated by subtracting the force just before the output began to return to the starting position by the force just after the maximum displacement was reached after the initial travel. The energy loss was calculated by subtracting the integrated area under the unloading curve from the area under the initial loading curve. The full-cycle efficiency value was calculated by dividing the integrated area under the unloading curve by the integrated area under the initial loading curve. The displacement loss was determined by recording the zero-force crossing of the unloading curve, which corresponds to the displacement at which the spring went slack.

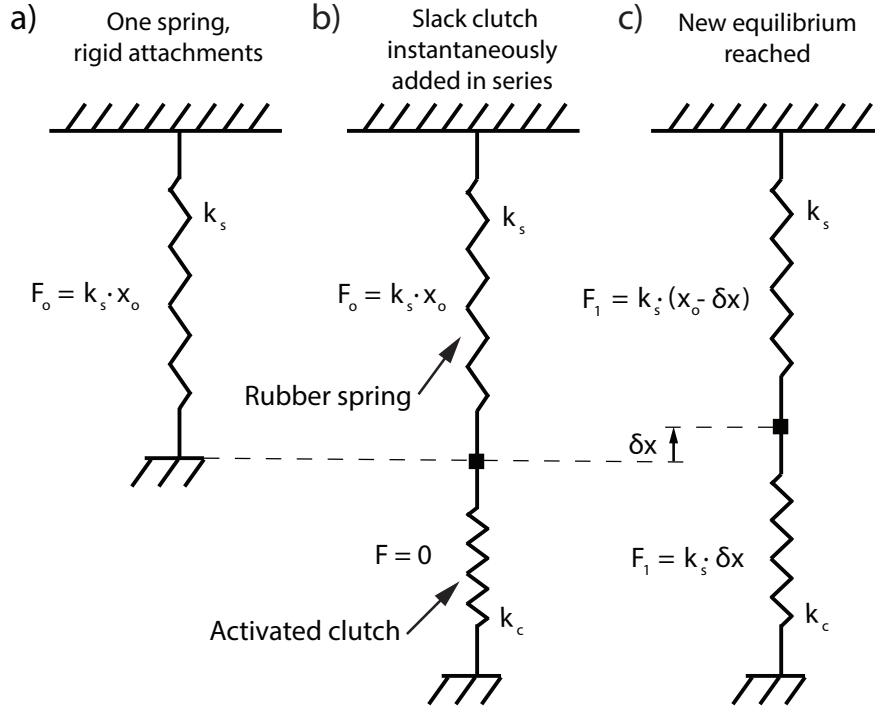


Figure 4.4: Inefficiency Model Boundary Conditions Diagram. a) The stretched rubber spring with stiffness k_s . b) The handoff is modeled by instantaneously adding a slack, activated clutch with stiffness k_c in series with the stretched spring. c) The connection point displaces until a new force equilibrium is reached. This results in a loss in the stretch of the rubber spring.

4.2.3 Inefficiency Model Derivation

I also derived a model for handoff efficiency as a function of spring and clutch stiffness based on the following equations. Beginning with a stretched rubber spring with a linear stiffness of k_s and a displacement of x_o from its slack length (Fig. 4.4a), I can calculate the stored strain energy as

$$E_o = 0.5 \cdot F_o \cdot x_o = 0.5 \cdot k_s \cdot x_o^2 \quad (4.1)$$

I assume that the spring is initially connected to perfectly rigid attachments on both sides. Next, I hand off one of the attachments of this spring to a slack activated clutch (Fig. 4.4b), which I treat as a spring with a linear stiffness of k_c . I assume the clutch is now attached to the rubber spring on one side, and to a perfectly rigid attachment on the other. In order to reach a stable equilibrium, the spring must spontaneously recoil through

a displacement δx until the new force F_1 in the spring and clutch are equivalent because the two are in series (Fig. 4.4c). Because the clutch and spring are attached, the clutch must experience the same displacement. This is expressed as

$$F_1 = x_1 \cdot k_s = \delta x \cdot k_c \quad (4.2)$$

$$x_1 = x_o - \delta x \quad (4.3)$$

where x_1 is the new spring displacement. The new spring strain energy is

$$E_1 = 0.5 \cdot k_s \cdot x_1^2 \quad (4.4)$$

Solving for δx and dividing by the displacement x_o gives the fraction displacement loss

$$\frac{\delta x}{x_o} = \frac{k_s}{k_c + k_s} \quad (4.5)$$

Because in my case $k_c \gg k_s$, I can simplify this to

$$\frac{\delta x}{x_o} \sim \frac{k_s}{k_c} \quad (4.6)$$

To find the handoff efficiency as a function of the spring and clutch stiffnesses, I can divide the spring energy after the handoff by the spring energy before the handoff. After substituting using Eqs (4.2-4.5) and simplifying, I find

$$\epsilon = \frac{E_1}{E_o} = \left(\frac{1}{\frac{k_s}{k_c} + 1} \right)^2 \quad (4.7)$$

For $k_s / k_c < 0.2$, this simplifies to

$$\epsilon \approx 1 - \frac{k_s}{k_c} \quad (4.8)$$

I also create a model prediction of displacement loss using the same method as in the derivation above, but with a Mooney-Rivlin model of the spring stiffness instead of the assumption of linear elasticity. The model does not have an explicit solution, and is computed by finding the maximum root of λ in the following equation

$$\left(\frac{k_c \cdot L_o}{A} + 2C_1\right) \cdot \lambda^4 + \left(2C_2 - \frac{k_c \cdot (L_o + x_1)}{A}\right) \cdot \lambda^3 - 2C_1 \cdot \lambda - 2C_2 = 0 \quad (4.9)$$

where A is the original rubber spring area, L_o is the rubber spring slack length, λ is the rubber stretch, and $2C_1$ and $2C_2$ are the Mooney-Rivlin coefficients of the rubber. I use experimentally determined values of 24 kN/m, 243 kPa, and 224 kPa for the clutch stiffness and Mooney-Rivlin coefficients respectively. I also add an additional 2% displacement loss due to the inherent damping of the rubber.

To investigate the effects of handoff force and clutched spring stiffness on efficiency for handoffs without clutch slip, I first performed quasi-static experiments with one second handoff overlap time, which is at least one order of magnitude larger than the measured clutch engage time. The clutched spring stiffness is changed only by changing the spring stiffness; the same clutches are used for each condition. The handoff overlap time is then varied for multiple force and stiffness conditions to investigate the interaction of these variables with the ability of the clutch to execute handoffs without slipping.

4.2.4 Results

The full cycle handoff efficiency increases slightly as the initial handoff force increases (Fig. 4.5a). As the spring becomes stiffer while the clutch stiffness remains constant, the full cycle efficiency decreases substantially (Fig. 4.5b).

The full cycle efficiency is constant at a low force of 30 N down to 10 ms handoff overlap time (Fig. 4.6a). At higher handoff forces of 50 N and 70 N, the efficiency drops off and the variability increases when the handoff overlap time shortens. This is the result

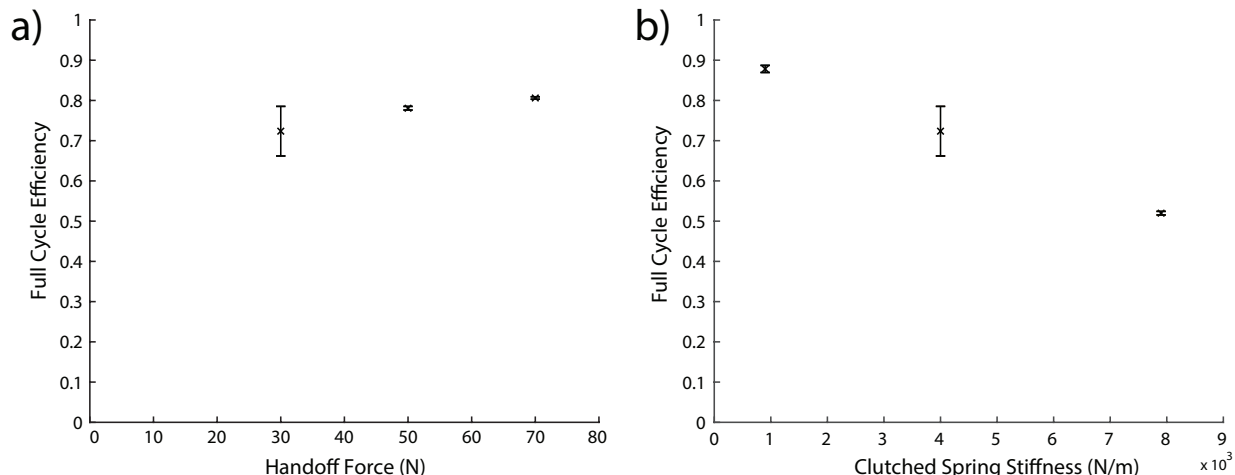


Figure 4.5: Quasi-static Full Cycle Efficiency as a Function of Handoff Force and Clutched Spring Stiffness. a) Efficiency as a function of the force in the spring prior to the first handoff for a constant clutched spring stiffness of 4 kN/m. b) Efficiency as a function of the clutched spring stiffness for a constant handoff force of 30 N.

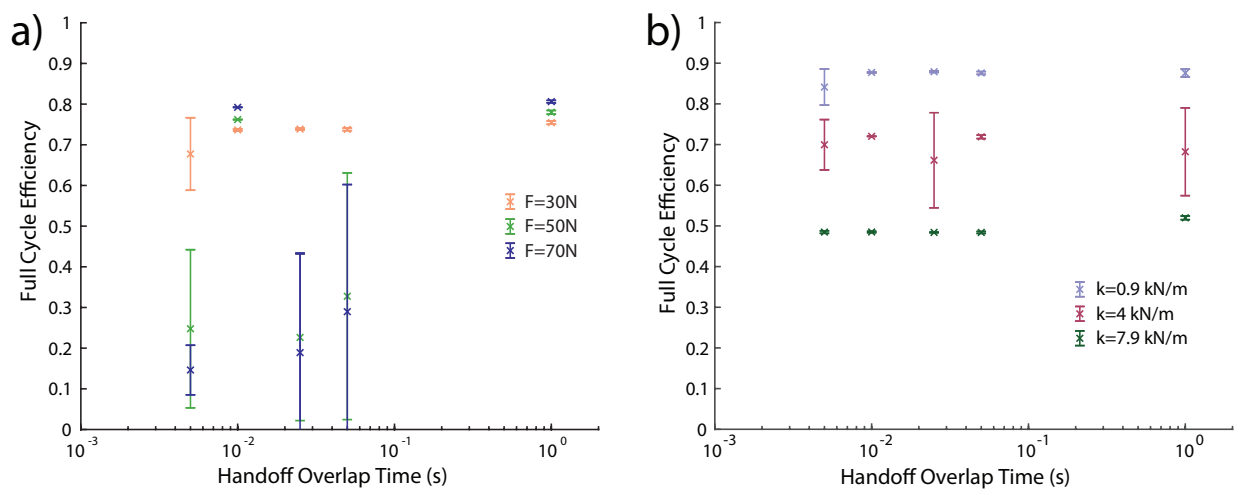


Figure 4.6: Full Cycle Efficiency as a Function of Handoff Overlap Time. a) Efficiency as a function of handoff overlap time at various handoff forces for a constant clutched spring stiffness of 4 kN/m. b) Efficiency as a function of handoff overlap time at various clutched spring stiffnesses for a constant handoff force of 30 N.

of the clutches slipping during handoff. The spring stiffness, however, has no interaction with handoff overlap time (Fig. 4.6b). At 30 N handoff force, the full cycle efficiency stays constant for each spring stiffness as the handoff overlap time decreases.

The fit of the model prediction of displacement loss to measured data has an R^2 value of 0.68 (Fig 4.7). The pictured data includes measurements from all of the quasistatic tests shown in Figure 4.5.

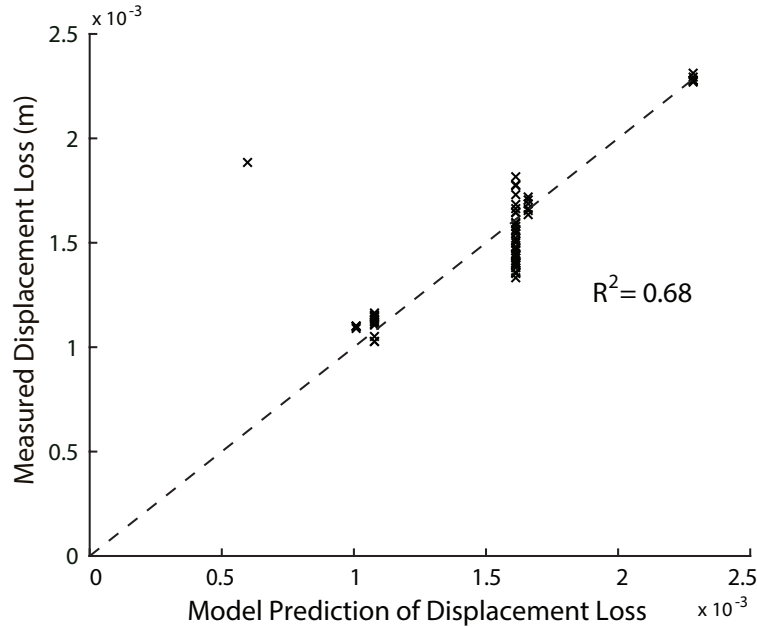


Figure 4.7: Model of Handoff Displacement Inefficiency.

4.2.5 Discussion

The results of the quasistatic handoff tests (Fig. 4.5) qualitatively agree with my expectations based on the simple model given in Eq. (4.8). While handoff force does not explicitly appear in this equation, a slight increase in handoff efficiency as force increases is expected because the spring stiffness decreases during the first $\sim 100\%$ strain of the rubber, which leads to a lower spring to clutch stiffness ratio. For a constant clutch stiffness and handoff force, increasing the spring stiffness leads to a dramatic decrease in handoff efficiency as this stiffness ratio increases.

In the tests of various handoff times, I observed large clutch slips during fast handoffs at high force (Fig. 4.6a), but saw no change in performance as handoff time decreased for all spring stiffnesses (Fig. 4.6a). This result was expected based on the results given in Figure 2.5 that indicate force transmitting capacity increases with time after activation. Practically, this translates to lower force limits for successful handoffs at very fast speeds. I believe the efficient handoffs at high forces and 10 ms handoff time in Figure 4.6a are due to ordering effects, and true operational values for this handoff time would be similar to the

surrounding data.

The displacement model from Eq. 4.9 has reasonable agreement with the measured quasi-static values (Fig. 4.7), even using a simple estimate of inherent spring losses. This result is sufficient for me to implement the inefficiency model in simulation to estimate the validity of proposed actuator designs and expected operation time.

From this experiment, I discovered multiple practical insights that inform control and actuator design. First, I learned that there exists an inherent trade-off between the maximum handoff force of a double-clutched spring and its best control speed and delay characteristics. This will practically limit the control speed based on the operating force of the clutched springs. However, the control speed is a characteristic that an energy recycling actuator could change in real time, for example in response to changes in the required force given a particular task.

I also learned that the most efficient double-clutched springs will have maximum on-state clutch stiffness and low spring stiffness. This motivates future efforts to make the electroadhesive clutches stiffer, or to create designs that apply a pre-stress to clutches prior to activation. I will also want to select spring materials and geometries that display low spring stiffness in my expected operating displacement region.

4.3 Energy Recycling Actuator Design Optimization

4.3.1 Introduction

After establishing design principles from testing individual double-clutched springs, I undertook the task of designing an energy recycling actuator prototype consisting of many electroadhesive double-clutched springs in parallel. While it's important to show high raw performance characteristics in benchtop tests, I also wanted to design a prototype that can also perform well in a challenging demonstration that approximates real-world use. To achieve this, I designed a 1 degree of freedom arm shown in Figure 4.8 and actuated by

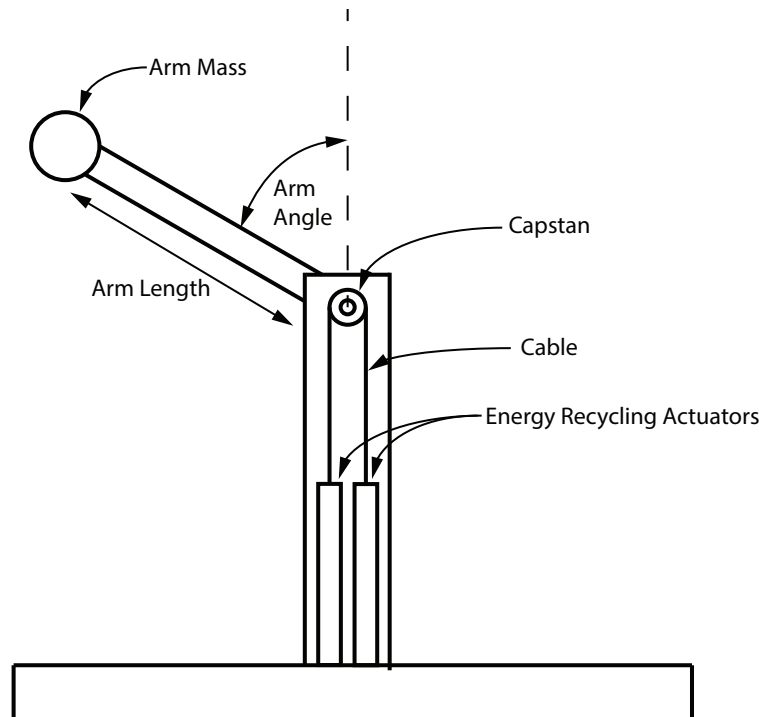


Figure 4.8: 1-DOF Robot Arm Schematic.

two energy recycling actuators. Each actuator is responsible for producing torque when the arm is on the opposite side. The arm can move through 1 full revolution, but is not capable of multiple continuous revolutions. While the general concept was set, the best specific design parameter values for the arm and energy recycling actuators were unclear. To address this challenge, I created a set of heuristic design requirements and constraints, and implemented a brute force optimization to identify the best design values for the arm and actuator designs.

4.3.2 Methods

The actuator design optimization was configured as a brute force optimization in which I evaluated every possible combination of the design parameters within predefined ranges. I made several simplifying assumptions. I assume that the rubber has a linear stress-strain response with an elastic modulus of $E = 500kPa$. I also assume that the mass of the clutches will scale linearly with the total maximum force capability of the actuator, at a rate

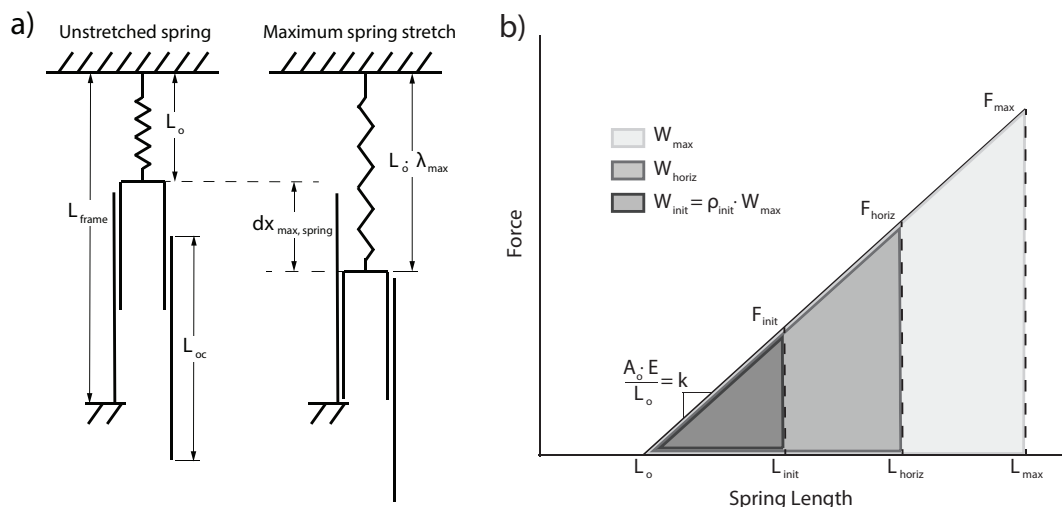


Figure 4.9: Parameter Schematic and Heuristic Illustration. a) A double clutched spring with design optimization parameters labeled. b) A spring force-displacement curve illustrating the relationships between the heuristics.

of 0.67 kg/kN . In order to reduce the size of the optimization, I assume that all of the energy storage rubber springs will be the same size, and that for this analysis they can be treated as a single large spring, neglecting any of the the control needed to distribute the energy across the springs during operation.

I used three heuristics to constrain the simplified design problem with the physical design parameters listed in Figure 4.9a. First, the springs must be able to store the potential energy of the entire active range, meaning the range of motion through which the actuator is expected to move the arm, as well as some predetermined amount of pre-charged energy. Second, the arm must be capable of accelerating the arm from rest with an acceleration of 9.98 m/s^2 when the arm is in the horizontal position. Third, each actuator is only responsible for exerting torque on one side of the arm travel, but the output must be able to travel through the distance required for the one full revolution of the arm.

To implement these heuristics, I first find the gravitational potential of the active range W_{motion} , which is

$$W_{motion} = m_{arm} \cdot g \cdot L_{arm} \cdot (\cos(\theta_1) - \cos(\pi)) \quad (4.10)$$

where θ_1 is the limit of the active range measured from the arm pointing straight up, and assuming that the active range extends down to the position of the arm at π , which is pointing straight down.

I define some pre-charged energy in the springs, so that the total energy W_{max} is

$$W_{max} = \frac{W_{motion}}{1 - \rho_{init}} \quad (4.11)$$

where ρ_{init} is the ratio of the pre-charged energy to the maximum energy. I then use the horizontal acceleration heuristic to determine the required actuator force F_{horiz} in that situation

$$F_{horiz} = \frac{2 \cdot m_{arm} \cdot g \cdot L_{arm}}{r_{capstan}} \quad (4.12)$$

Next, I find the energy stored in the actuator with the arm at rest in the horizontal position W_{horiz} using

$$W_{horiz} = W_{max} \cdot \rho_{init} + \left(\cos(\theta_1) - \cos\left(\frac{\pi}{2}\right) \right) \quad (4.13)$$

This fully defines the needed force-displacement curve of the sum of the springs (Fig 4.9b). Because the spring is linear, I can find the max force F_{max} in the springs when they are storing W_{max} using

$$F_{max} = F_{horiz} \cdot \sqrt{\frac{W_{max}}{W_{horiz}}} \quad (4.14)$$

Now I need to find the spring geometry necessary to satisfy the force and energy conditions. From the definition of linear elasticity, I can determine the necessary spring total area and slack length with

$$A_o = \frac{F_{max}}{E \cdot (\lambda_{max} - 1)} \quad (4.15)$$

$$L_o = \frac{2W_{max}}{F_{max} \cdot (\lambda_{max} - 1)} \quad (4.16)$$

where λ_{max} is the maximum stretch of the rubber, which I treat as an input design variable and set to 3.

I now define the equations that constrain the valid solution space. First, the active travel of the actuator must be at least as long as the designed travel of the springs $dx_{max,spring}$, or else it would not be possible to input all of the required energy into the springs during the course of the arm's movement. I define ρ_{travel} as the minimum ratio of active travel to spring travel, and enforce the following condition

$$r_{capstan} \cdot (\theta_1 - \pi) \cdot \rho_{travel} > dx_{max,spring}. \quad (4.17)$$

Our next constraint ensures that the output clutch plates do not extend beyond the bottom of the actuator. This simply means the output clutch plate length L_{oc} must be shorter than the length of the actuator frame L_{frame}

$$L_{frame} > L_{oc} \quad (4.18)$$

Similarly, the output clutch plates should not extend completely out of the actuator during operation, meaning that the output clutch plates must be longer than the travel through the full revolution of the arm.

$$L_{oc} > 2\pi \cdot r_{capstan} \quad (4.19)$$

I also require the sum of the frame length and total travel must be smaller than the length of the arm.

$$L_{arm} > 2\pi \cdot r_{capstan} + L_{frame} \quad (4.20)$$

As the designer, I can then set the allowable clutch shear pressure $\sigma_{max,clutch}$, the maximum actuator length, and the maximum number of clutched springs. The optimizer then evaluates all combinations of arm mass, arm length, ratio of energy precharge, and capstan radius, and eliminates the solutions that do not satisfy all of the constraints. The allowable solutions are evaluated in the following goodness function.

$$GF = 0.5 \cdot \log(m_{arm} \cdot L_{arm}/30) + 0.25 \cdot \log\left(\frac{W_{max}}{m_{act}}/100\right) + 0.25 \cdot \log\left(\frac{F_{max}}{m_{act}}/1000\right) \quad (4.21)$$

The terms the optimizer will maximize are the maximum arm torque, the energy storage density, and the force density. Each of these values are normalized by estimated minimum desired values to make the terms non-dimensional, and the log is taken to ensure that a low value in any particular term will have a large penalty, generally helping to prevent solutions with extreme combinations of high and low values. The terms are given weights of 0.5, 0.25, and 0.25 for the arm torque, energy storage density, and force density, respectively.

4.3.3 Results and Discussion

Many combinations of input constraints were evaluated, and this design was selected for its combination of high performance and practical inputs.

Table 4.1: Output Values of Actuator Design Optimization

Input Constraints	L_{frame}	n_{cs}	$\sigma_{max,clutch}$							
	0.36 m	20	7.8 kPa							
Output Values	m_{arm}	L_{arm}	$r_{capstan}$	ρ_{init}	W_{max}	F_{max}	L_{oc}	L_{sc}	L_o	A_o
	8 kg	0.6 m	0.04 m	0.27	130.6 J	3010 N	0.32 m	0.19 m	0.043 m	3.01 e^{-3} m ²

This optimization was a faster and more systematic alternative to designing this challenging system by hand. This technique could be expanded into more sophisticated problems, including multiple actuated degrees of freedom or hybrid actuation systems. The implementation could also be improved by switching to more sophisticated optimization

techniques such as gradient descent or stochastic evolutionary methods that could reduce the computation time.

4.4 Controller Optimization in Simulation using CMAES

4.4.1 Introduction

Using many double-clutched springs to achieve high-performance tracking in a robotic system presents a challenging and unconventional control problem. In addition to producing low force or displacement error, the actuator should stay strictly within its physical constraints and operate as efficiently as possible. In order to quickly evaluate many possible clutched-spring controllers, I created a simulation of the energy recycling actuator on the 1-DOF robot arm in which the controller attempts to produce a desired arm trajectory. I then implemented an evolutionary optimization algorithm that evaluates many possible controllers in the simulation and identifies the optimal set of control parameters that gives the best high-level performance.

This simulation also provided a way to verify the output of the design optimization and predict the performance of the energy recycling actuator prototype. By using the design inputs from Table 4.1, the simulation gave estimates of the best tracking accuracy and maximum operating time of the proposed actuator design for tracking various displacement profiles. This also provided initial controller parameter values for future use in hardware testing.

4.4.2 Methods

I created a simulation of the arm and a single actuator with the design described in 4.3.3 using MATLAB Simulink. The simulation was a forward integration using the ode5 solver and a fixed step of 20 ms. The arm physics were defined by the equation

$$\ddot{\theta} = \frac{(F_{act} \cdot r_{capstan} - m_{arm} \cdot g \cdot L_{arm} \cdot \sin(\theta))}{(m_{arm} \cdot L_{arm}^2)} \quad (4.22)$$

where F_{act} is the force exerted by the actuator.

I implemented a high-level PID arm position controller commanding force to a low-level clutch activation controller. A gravity offset term was also added to the high-level position controller. The low-level clutch activation controller functioned by evaluating all of the possible combinations of clutch activations on each control step and choosing the combination that minimized the cost function

$$CF = w_f \cdot |F_{des,i} - F_{act,i}| + w_c \cdot \sum_n |\vec{S}_i - \vec{S}_{i-1}| + w_p \cdot \sum_n \left(\frac{\vec{x}_{i+1,est} - x_{rmp}}{x_{rmp}} \right)^2 \quad (4.23)$$

where w_f , w_c , and w_p are the cost function weights, $F_{des,i}$ is the commanded force on the current timestep, $F_{act,i}$ is the expected force from the proposed combination of clutch activations, \vec{S}_i is a vector of ones and zeros representing the proposed combination of clutch activations and \vec{S}_{i-1} is the vector of clutch activations from the previous control step, $\vec{x}_{i+1,est}$ is the vector of anticipated spring positions on the next control step given the current output velocity and the proposed clutch activations, and x_{rmp} is the midpoint of the defined acceptable range of spring positions. A control step of 100 ms was used for the low-level clutch activation controller. Because the number of activation combinations scales with $2^{n_{clutchedsprings}}$, I restricted the maximum number of independent clutch controls to 10, meaning that the clutched springs were controlled in 10 groups of two. The handoff inefficiency model shown in Fig. (4.7) was included on each clutch state change. The force in the springs was calculated as a function of their stretch using the Mooney-Rivlin model with coefficients $2C_1 = 243kPa$ and $2C_2 = 224kPa$.

I performed simulations of the actuator moving the arm through a prescribed cyclic trajectory using my controller, and assigned grades to the performance based on the number of consecutive cycles completed within certain bounds on the acceptable root mean squared

position error e_{max} that I set at 25%, relative to the arm being held stationary at the mean position. The scores were determined by the following equation

$$score = n_{cyc} - \left(\frac{e_{mean}}{e_{max}} \cdot \frac{n_{cyc}}{1.5} \right) \quad (4.24)$$

where n_{cyc} is the number of consecutive cycles successfully within the error bound, and e_{mean} is the mean error during those cycles. The term in parentheses was added to distinguish between controllers that completed the same number of cycles, but with different tracking quality. The constant value in this term was selected by hand by iteratively updating them while observing the quality of the optimization output.

The optimization algorithm simultaneously optimized 5 control parameters, specifically the 3 PID gains and the clutch change w_c and position w_p terms in the low-level controller cost function. I set the force error weight w_c a value of one, because only the relative values of the low-level controller weights impact the optimization's decisions. After randomly selecting 10 parameter sets from a distribution and scoring them, the algorithm uses a covariance matrix adaptation evolution strategy (CMA-ES) [118, 95] to create a new sampling distribution and randomly select the next 10 parameter sets, or generation, to score. The goal of the algorithm is to find the set of parameters that maximizes the score, and thus the performance of the controller. In my testing, the algorithm evaluated 10 generations with 10 sets of parameters each.

4.4.3 Results

Figure 4.10 illustrates the impact of each of the low-level force control optimization terms on the spring displacements during the test. This figure was created by taking an optimized controller and documenting the effects of excluding low-level controller optimization terms, in order to illustrate their effects. The full optimized low-level controller (Fig. 4.10a-c) tracks torque as requested by the high-level controller and maintains all of the springs above the

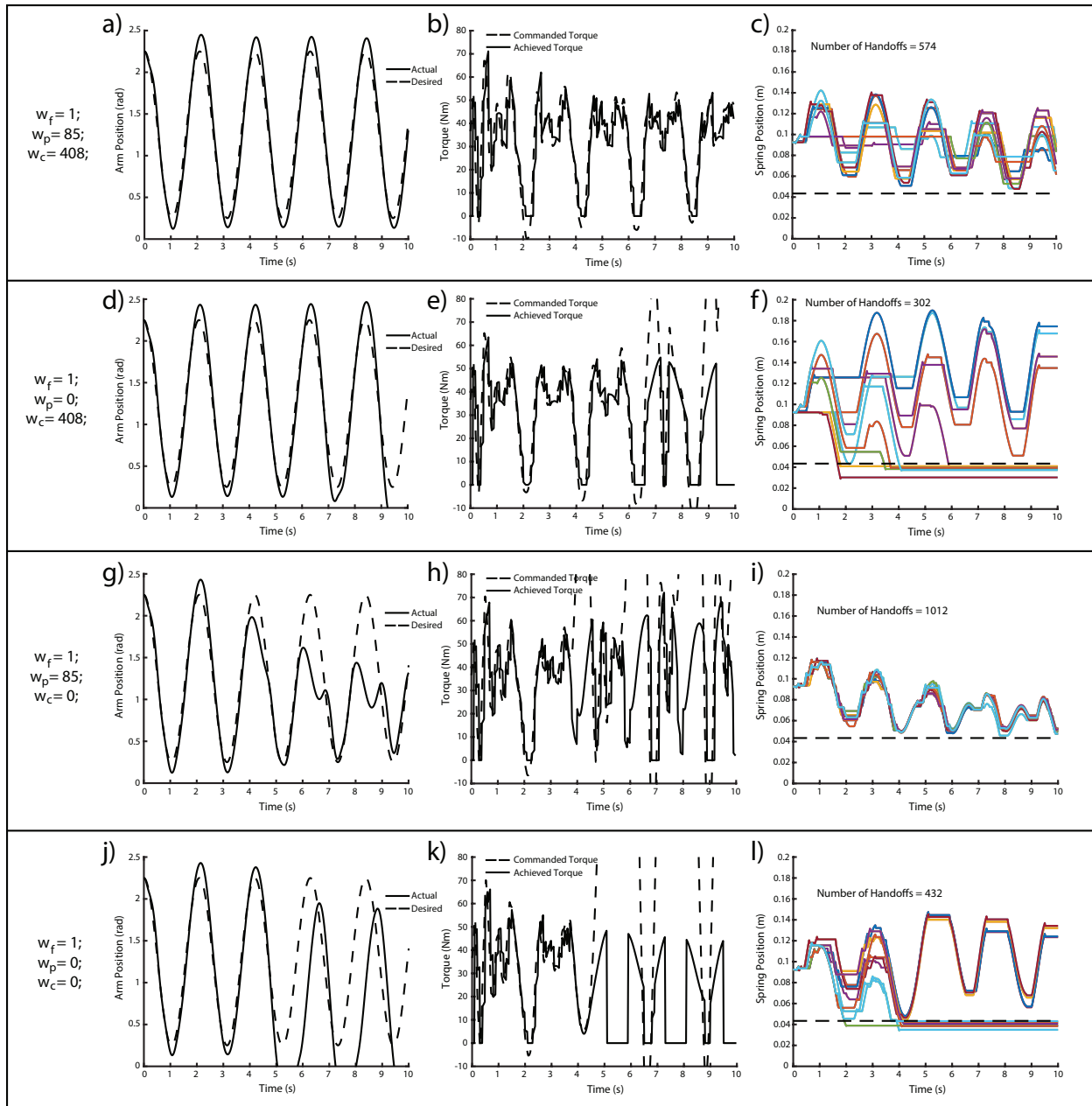


Figure 4.10: The Effects of CMAES Optimized Low-Level Control Terms in Simulation. Arm position, applied torque, and spring positions for: a-c) An optimized low-level torque controller with the modeled displacement inefficiency. d-f) The low-level torque controller excluding the spring deviation term. g-i) The low-level torque controller excluding the handoff minimization term. j-l) The low-level torque controller excluding the spring deviation and handoff minimization terms.

slack length with a moderate number of handoffs. When the position conditioning term weight is set to zero (Fig. 4.10d-f), the controller can initially achieve good torque tracking, but an increasing number of springs shorten past the slack length. Once a spring goes slack

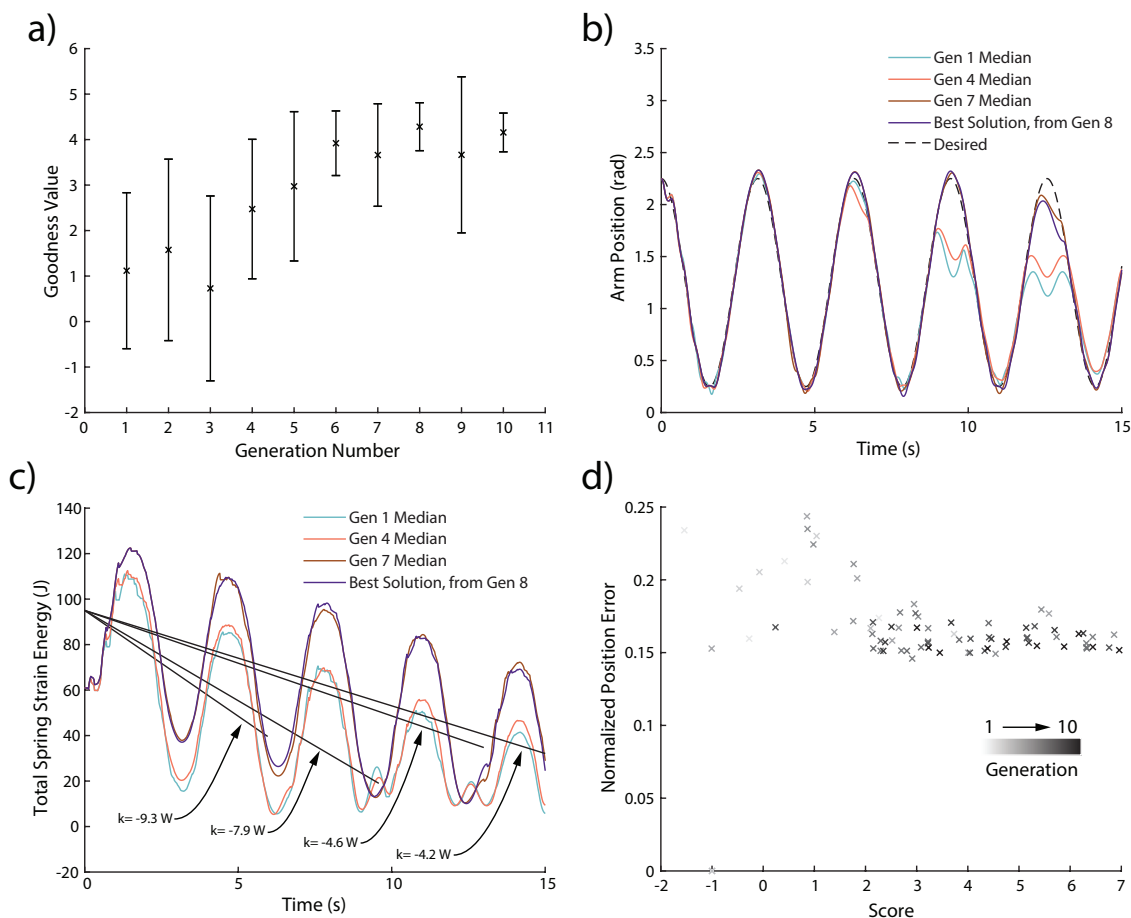


Figure 4.11: Improvement of Controller Performance as CMAES Algorithm Progresses. a) Average controller performance as a function of CMAES Generation Number. b) Simulated arm torque tracking for controllers taken from multiple optimization generations. In these plots, an arm position of 0 is defined as the vertical position pointing downward. c) Total spring strain energy as a function of time. The best controllers have the lowest average energy loss rate from the handoff inefficiency. d) Normalized error vs score for all generations. The darker data belong to later generations.

the spring force goes to zero, and the controller has no incentive to re-engage the spring to stretch it again. After a few cycles, too few clutched springs remain to produce enough torque to satisfy the request of the high-level controller. If the handoff minimization term is excluded instead (Fig. 4.10g-i), the total number of handoffs doubles, causing the system to lose energy to the inefficiency much faster. After a couple cycles, the springs no longer contain enough energy to move the arm to its highest position, and the desired position can no longer be tracked in high potential energy regions. Finally, when only the force error minimization term is used ((Fig. 4.10j-l), both the inefficiency losses and slack springs cause

the actuator to quickly lose its ability to track desired torque. Comparing the spring position plots for each condition ((Fig. 4.10c,f,i, and l) illustrates how the handoff minimization term and the position conditioning term balance one another to produce good torque tracking while keeping spring positions in a reasonable window with a low number of handoffs.

The results of a CMAES optimization of controller performance are shown in Figure 4.11. As the algorithm progress through multiple generations, the average solution quality increases and the standard deviation of the solutions decreases (Fig 4.11a). This can also be seen in the tracking profiles of solutions from different generations (Fig 4.11b), as the solutions from later generations are able to track the desired profile with lower error for a longer period of time. This longer tracking performance corresponds with a slower rate of energy loss (Fig 4.11c) due to the handoff inefficiency. The early generation solutions are unable to track the last cycles because their spring energy bottoms out before the arm is able to reach its highest potential energy position. The average tracking error does not increase for later generations (Fig 4.11d), showing that controllers that produce longer operation do not necessarily sacrifice accuracy.

4.4.4 Discussion

These simulation results show that an optimization-based low-level torque controller can be effective for the energy recycling actuator. Using this low-level controller with a high-level PID position controller produced reasonable tracking, but was susceptible to systematic errors such as position overshoot. More reliable position tracking could be achieved by implementing gain scheduling or iterative learning, or instead by switching to a model predictive control approach. Another notable result is that the discrete force control of the device can produce smooth motion in this system. This is because the arm is fairly large and massive, meaning that stepwise changes in applied torque do not produce sudden movements.

This simulation also confirmed that the heuristic design optimization produced a design capable of the force and energy storage required to manipulate the arm. As a result, I have

higher confidence that my physical implementation and controller will produce good results using the optimized controller parameters found in simulation.

This simulation could be an extremely useful tool for exploring the use of an energy recycling actuator in many other applications in much less time than would be required for physical implementations. This would be particularly advantageous for systems with multiple actuated degrees of freedom. Additionally, simulation tools such as this one are much better suited than physical testbeds for quickly evaluating many new controller options that include features such as energy transfer and control coordination between joints. Once the simulation results are confirmed by similar experiments using the physical prototype, the simulation can be used with high confidence to explore these more complex systems.

4.5 Actuator Characterization

4.5.1 Introduction

In the previous sections, I established double clutched spring design principles, optimized high-level design parameters, and demonstrated good actuator performance in simulation. However, many challenges still remained before successful prototype performance could be demonstrated. In this section, I cover the detailed design, assembly, calibration, and force tracking of the energy recycling actuator.

4.5.2 Methods

The construction of a double-clutched spring is illustrated in Figure 4.12. The series rubber spring is glued to carbon fiber battens on top and bottom, with one side fixed to the base using attachment pins. The top of the spring has two clutch plates attached to the carbon fiber battens, one clutching to the frame and the other to the output. These clutch plates are each tensioned by fishing wire connected to thin rubber tensioners, that in turn connect to the bottom carbon fiber batten. These fishing wires slide through grooves cut on the sliding

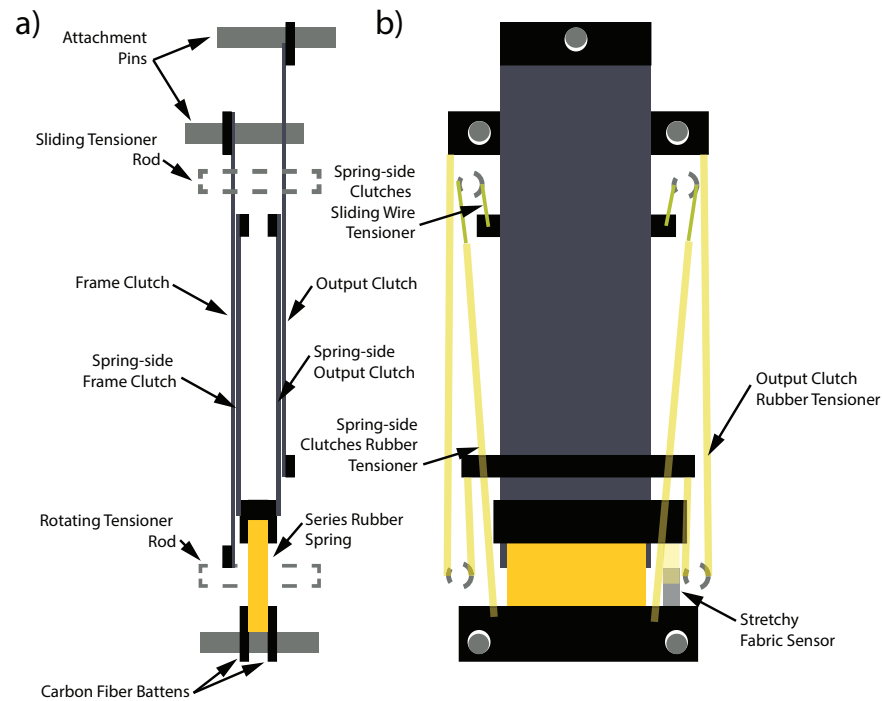


Figure 4.12: Diagram of Double Clutched Spring Construction. a) Side view. b) Front view.

tensioner rod. This sliding solution was implemented because the springs can be at different lengths during operation, meaning that the tensioners for various springs will require relative movement that could not be achieved with a rotating tensioner rod. The frame clutch is attached on the top to the frame attachment via another two attachment pins, and has small rubber tensioners that connect to the bottom carbon fiber batten. The output clutch is attached to the output attachment via another attachment pin, and is tensioned by thin strips of rubber that wrap around the rotating tensioner rod and attach to the frame carbon fiber batten. Because all of the output clutches move simultaneously, a rotating tensioner rod can be used in this case.

The tensioner rods are used to enable more constant tensioner forces and a more compact actuator design. The maximum stretch of the tensioning rubber is very high (approximately 6), but the output clutch travels through most of the total length of the actuator, which would require much a much larger stretch from a linear tensioner attached to the bottom carbon fiber batten. By wrapping the tensioner and connecting to a batten on the far side of the tensioner rod, the initial spring length can be much longer, which dramatically reduces

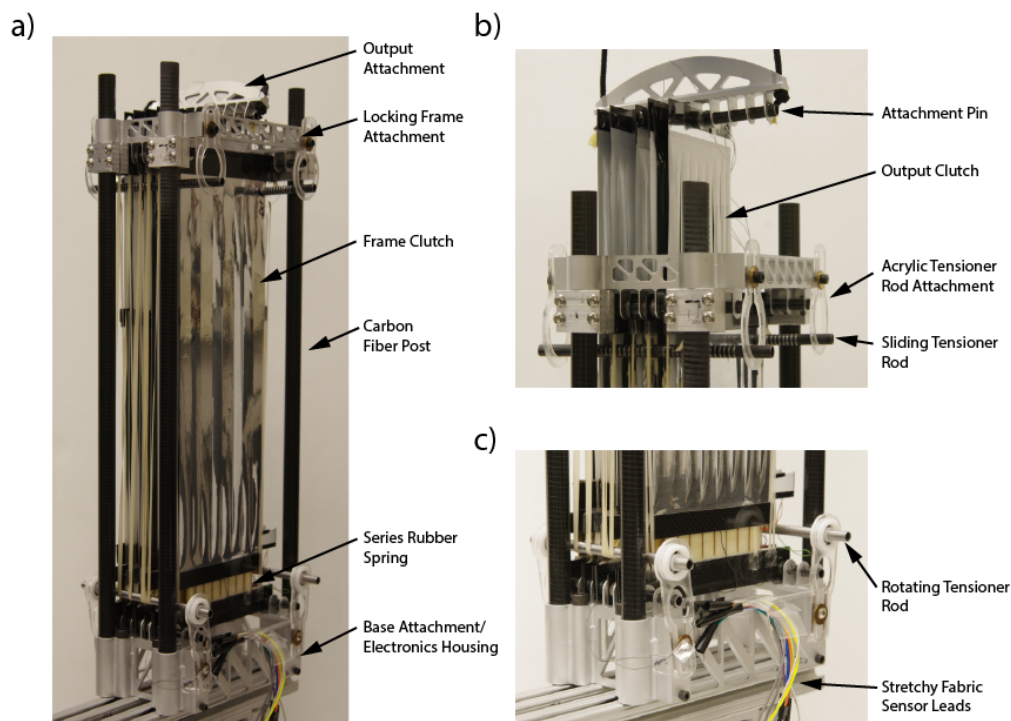


Figure 4.13: Energy Recycling Actuator Construction. a) Full actuator. b) Zoomed view of output and locking frame attachment. c) Zoomed view of base attachment.

the maximum stretch and the change in tensioner force as the clutch travels. This also results in more constant tension force throughout the range, which helps ensure reliable handoffs.

The stretchy fabric sensor is placed in parallel with the energy storage spring and attached to the same battens, so that its displacement corresponds to the displacement of the spring. I can then calibrate the capacitance output of the sensor to measure the displacement of the spring in real time. The sensors are composed of silver-coated conductive fabric adhered to either side of a thin layer of Ecoflex elastomer [119]. As the sensor is stretched, the elastomer layer separating the electrodes becomes thinner, causing an increase in capacitance. The sensors were fabricated according to the process provided in [119], which also details the relevant sensor properties. Because the maximum stretch of the sensor is approximately 2, I also connected two thin pieces of ecoflex in series with the sensor using Silpoxy (Smooth-On, Macungie, PA, USA). The resulting composite structure can stretch to a value of 4 without breaking the fabric sensor.

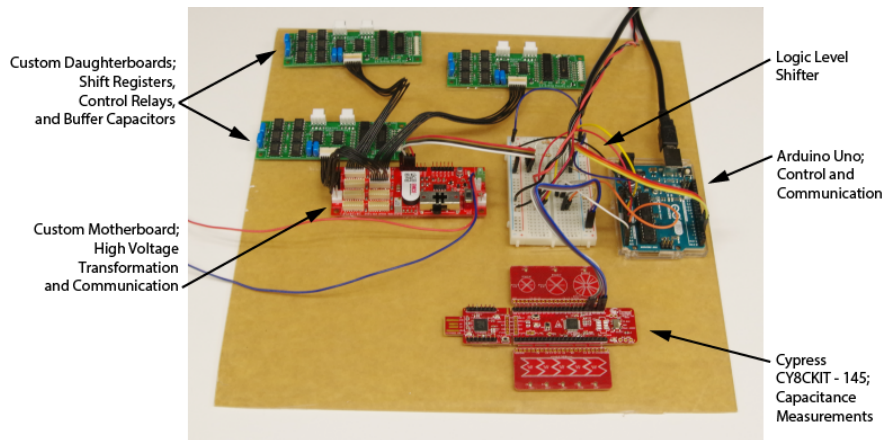


Figure 4.14: Electronics and Control Hardware for Energy Recycling Actuator. Credit - Erez Krimsky

The energy recycling actuator is shown in Figure 4.13, with multiple double-clutched springs. The base frame attachment provides structure for the attachment to the series energy springs and the rotating tensioner rods, as well as the four carbon fiber posts that are loaded in compression when tensioned springs are clutched to the frame. The number of double clutched springs was reduced to 16 for this prototype, to accommodate manufacturability challenges of the base frame attachment. The carbon fiber posts were adhered to the base attachment using epoxy (Scotch-Weld DP420-NS, 3M, St. Paul, MN, USA). The base is also sized to house the required electronics hardware. The locking frame attachment connects to the other end of the carbon fiber posts, and supports the frame clutch attachment pins and the sliding tensioner rods. Two-sided hub clamps were used to attach the locking frame to the carbon fiber posts, in order to provide height adjustability during initial testing. The output attachment transmits the load from the springs clutched to the ropes that will attach to the capstan of the arm.

The electronics hardware design and assembly was performed by my collaborator Erez Krimsky. Erez also performed most of the microcontroller programming used in the testing. The electronics were initially attached to an acrylic base (Fig. 4.14 rather than the electronics housing in the base attachment, to allow easy access during initial testing. The Arduino is programmed to perform the low-level clutch control and relay all of the measurements to a computer. A Cypress microcontroller measures the capacitance of the stretchy fabric

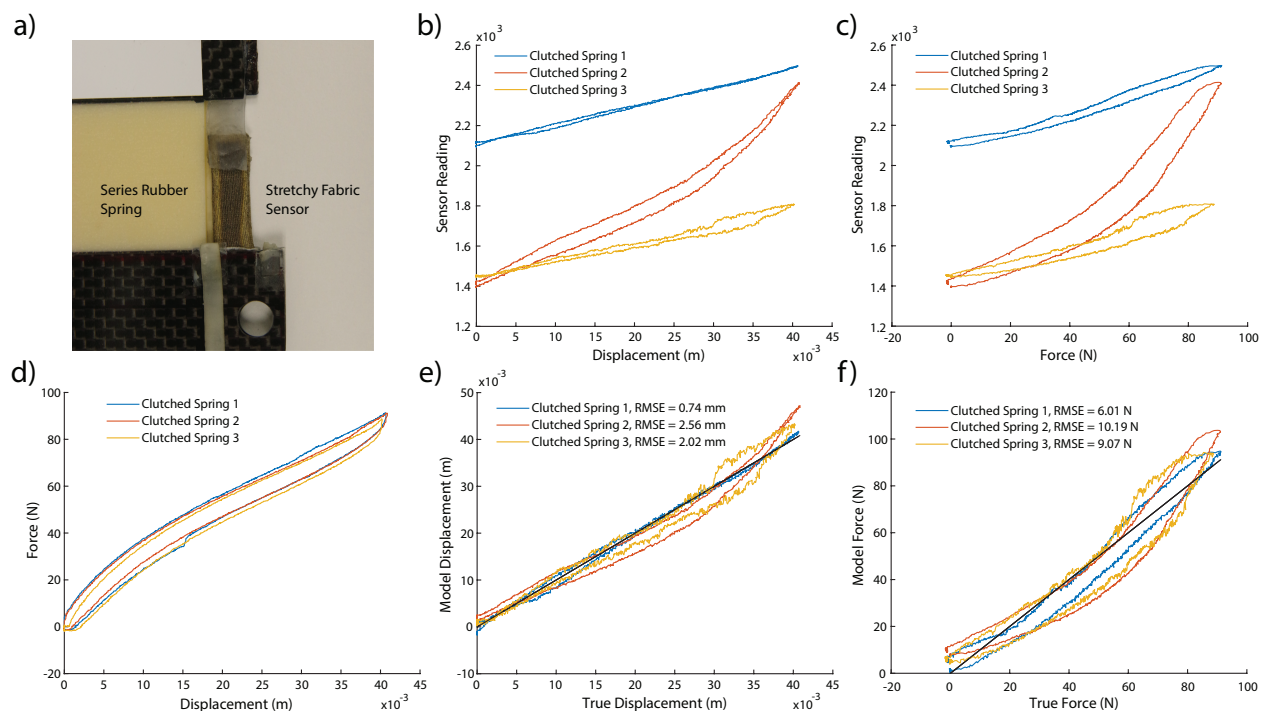


Figure 4.15: Stretchy Fabric Sensor Calibration. a) Image of sensor spanning spring length. b-c) Sensor output as a function of displacement and force. d) Force-displacement curves of the clutched springs. e-f) Models of displacement and force based on linear calibrations of the data in b-c.

sensors and relays them to the Arduino via an I2C connection. The custom motherboard receives clutch control signals from the Arduino through a logic level shifter, and controls the high voltage relays on the daughter boards using shift registers. The motherboard also transforms low voltage to 300 V DC, and provides this high voltage to the daughter boards, which connect to the electrical leads of the clutches. The detailed diagrams of the custom electronics hardware boards are provided in Appendix A.4.

To calibrate the stretchy fabric capacitance sensors, I attached the actuator base to the base of a materials testing machine (Instron 5969, Instron, Norwood MA) and the output to the moving head of the materials tester. I connected the analog force and displacement outputs of the materials tester to the Arduino, in order to sync the controls and external sensor readings. Because I have only one load cell in the materials tester, I needed to calibrate the sensors one at a time. To do this, I activated the output clutch of one clutched spring, and displaced the output while recording the force and displacement from the materials tester.

After calibrating the sensors, I conducted a force-tracking experiment using the low-level

controller implemented in the Arduino with three clutched springs using a control step of 300 ms and a handoff overlap time of 150 ms. First, all three springs were clutched to the output and the output was displaced by the materials tester. Then the control was activated and the low-level controller tracked a force profile in real time by controlling the clutch states.

4.5.3 Results

Table 4.2: Mass of Energy Recycling Actuator Components

Components	Mass (g)
Frames and Posts	567
Attachment Pins and Tensioner Rods	99
Double-Clutched Spring	47
Total with 16 Double-Clutched Springs	1418

The linear calibration of the stretchy fabric sensors (Fig. 4.15e) produced fairly low error of less than 3 mm, or less than 10% of the maximum displacement value. The linear calibration to force (Fig. 4.15f), however, produced up to 10 N of root mean squared error. This is consistent with the non-linear and hysteresis-prone relationship between force and displacement in rubber, as can be seen in Figure 4.15d.

Despite this error in the sensor calibration to force, the actuator was able to reasonably track the desired force during the actuator tracking experiment (Fig. 4.16). The summed force from the engaged spring sensors, or in other words the controller’s estimate of force on the output, was consistently lower than the true value measured by the materials tester. The clutches attached to spring 1 fail a handoff, leading to the spring losing most of its force. However, the sensor was able to detect this, and once the spring was slack the controller correctly did not continue engaging it to the output. The other two springs are successful in all of their spring handoffs, and the small drops in force due to the handoff inefficiency are visible after the clutch state changes occur. After spring 1 goes slack, the force in the

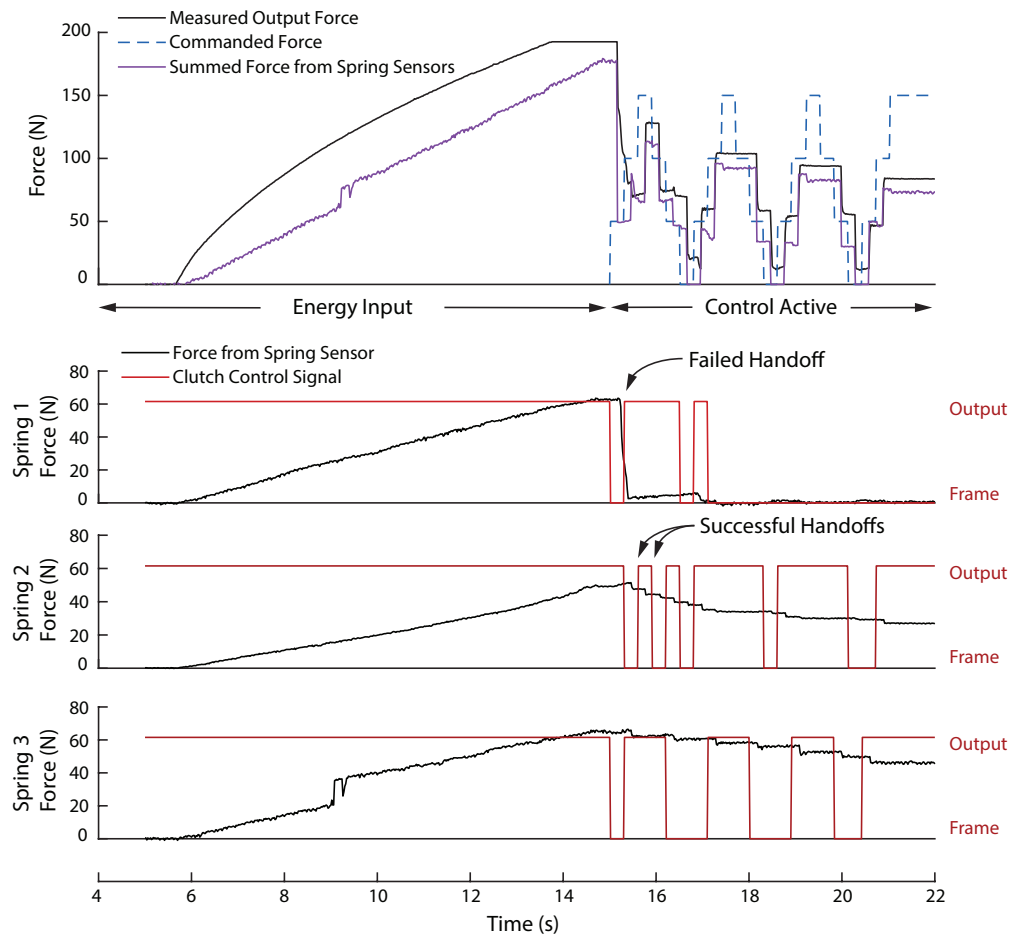


Figure 4.16: Energy Recycling Actuator Force Tracking. The x axis of all panels is shown at the bottom of the figure. The top panel shows the materials tester measured output force, the commanded force, and the summed force from the spring sensors. The bottom three panels show the each spring sensor's force measurement, with the control state imposed on top. The summed force from spring sensors data is equivalent to the sum of each of the spring force curves multiplied by their respective control state.

remaining springs is not enough to achieve the highest requested force, but the low-level controller is able to continue tracking the lower requested force values in spite of this.

4.5.4 Discussion

The force tracking test demonstrates that the integrated sensors, electronics hardware, low-level clutch controller, and double-clutched springs can successfully track commanded force in real time. Adding additional clutched springs will improve the accuracy of output force, and further testing could lead to improvements in the practical control implementation that

would reduce lag. This exciting early result proves the efficacy of the basic approach and double-clutched spring hardware, and justifies continued and expanded characterization.

The capacitance sensors provide a good measurement of displacement (Fig. 4.15e), but need improvement in their measurement of force (Fig. 4.15f). A simple way to achieve improved force readings would be to implement a Mooney-Rivlin calibration fit to account for the non-linear stiffness of the rubber. However, this will not address the error due to the force hysteresis of the rubber. One way to account for the force hysteresis would be to perform force-extension experiments with a variety of randomized movement frequencies and displacement magnitudes. This data could then be used to fit a high order model with polynomial terms or derivative and integrated terms. Alternatively, a machine learning model such as a neural network could use the experimental dataset as training data to produce a non-explicit model. In any case, the effectiveness of these approaches will be limited by the error in the displacement calibration, so additional design work is warranted to achieve the best displacement reading possible.

An alternative way to measure force would be to instrument each rubber spring with a separate force transducer in series. However, adding 10-20 traditional force sensors such as a strain-gauge based load cells, piezoelectric sensors, or hydraulic sensors would dramatically increase the overall weight and power consumption of the actuator. One potential solution is to redesign the carbon fiber battons to include a region for attaching a single strain gauge that is only excited for a small amount of time during each control cycle. A multiplexer could also be used to perform all of the measurements with a single amplifier and half-Wheatstone bridge circuit. This could potentially satisfy the requirements for low mass and power consumption as well as the size constraints of the clutched springs.

The actuator demonstrated force tracking that qualitatively matched the commanded force (Fig. 4.16). The delay between the commanded force and achieved output force is equal to the handoff overlap time. This is because it is only after the handoff overlap time has passed that the load paths are ‘updated’ to the new states and the output observes a

change. While spring 1 causes poor tracking initially because of a failed handoff, springs 2 and 3 each successfully execute multiple handoffs with high efficiency, as evidenced by the small drops in force observed after each state change. The commanded force is shown as a step function. This commanded force profile could actually represent a down-sampled triangle or sine wave, but has been shown in a square wave form to more clearly show the actuator's true tracking ability. Future implementations of this test with more clutched springs will show tracking of profiles that look much more continuous. Because the test was conducted with a fixed output, the spring length conditioning and handoff minimization terms were not required, but they will be included in future moving output tests. While this test represents a very preliminary result, it demonstrates the ability of the integrated physical system and electronics to produce the desired force and shows promise for future tests with more double-clutched springs.

4.5.5 Future Work

The most immediate future work will be to conduct additional fixed output force tracking tests with additional double clutched springs. Next, I will construct the robotic arm and demonstrate force tracking using the high-level position and low-level force optimization controllers. I expect this demonstration will set a benchmark for actuator system weight and required power consumption. For a direct comparison of required weight and power consumption, I will also separately implement a geared motor on an otherwise identical arm performing the same motion tasks. Finally, I will design and create a hybrid system consisting of the energy recycling actuator and a small motor to enable prolonged continuous operation and demonstrate it on the robot arm or another hardware system.

Chapter 5

Conclusions and Future Work

In this thesis, I presented the design, characterization, and implementation of electroadhesive clutches in robotics applications. Compared to conventional clutches, the electroadhesive clutch achieved order of magnitude improvements in weight and power consumption and demonstrated fast response times. In my first study, I thoroughly characterized the electroadhesive clutch's performance and produced a comprehensive design guide detailing how to size and incorporate the clutches for a wide range of potential applications. I also demonstrated an exoskeleton that used an electroadhesive clutched spring to assist walking, showing reliable control for hundreds of steps. Finally, I designed and fabricated a zero net work actuator using electroadhesive double-clutched springs that was capable of highly efficient energy recycling and force control.

I envision the impact of this thesis to be much broader than simply higher performance in wearable exoskeletons, or even the in field of mobile robotics. In this body of work, I provide the tools for researchers and industry designers to incorporate lightweight, low-power, reliable clutches in any application where the alternative clutches and actuation systems simply aren't adequate. The broader value of our demonstrations of electroadhesive clutches in several challenging applications is in giving our audience confidence that our solution actually does enhance performance and is practical enough for real-world implementation.

Future work should investigate fundamental studies of the force mechanisms at the interface of the clutch. To understand the relative contributions of friction, Van der Waals, and other force interactions at the interface, the surface roughness and coefficient of friction of the dielectric could be systematically varied and tested. Replacing or augmenting the electric field as the source of normal pressure with stacked weights or an air pressure gradient could give further insight. Changing the size of the ceramic particles in the dielectric could also substantially change the behavior of the clutch. Placing markers on the surface of the clutch and tracking their displacement during loading would give insight regarding the uniformity of loading and optimal geometry. These experiments aimed at understanding the fundamental behavior of the clutch could translate into design changes that achieve substantially higher force or lower clutch weight and voltage.

New future designs using electroadhesive clutches could include variable gear ratio transmissions, variable stiffness transmissions, and adjustable gravity offset systems in both industrial and human environments. The energy recycling actuator could also be incorporated into exoskeletons, prostheses, and walking robots to investigate its feasibility and performance in lightweight mobile devices. Future controls work in both simulation and hardware is warranted to identify and optimize controllers suitable for a variety of applications.

Appendix A

A.1 Control Circuits

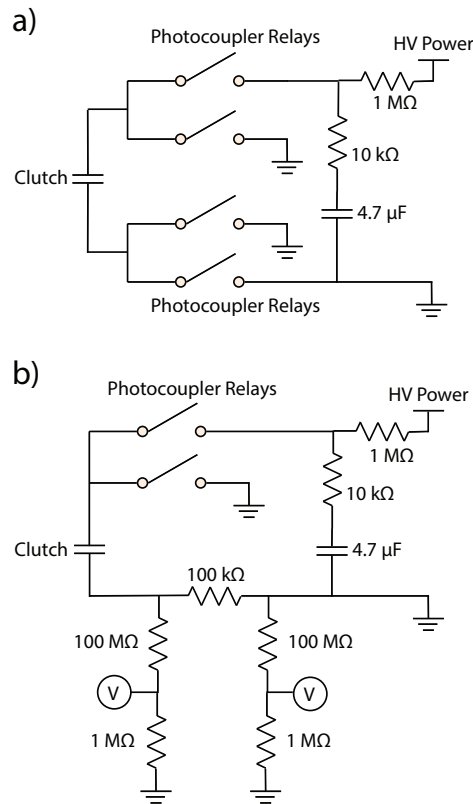


Figure A.1: Circuit Diagrams a) Control circuit for maximum holding force, release, engage, and fatigue tests. b) Control circuit for capacitance and power consumption tests.

The control circuits used for experimental testing are shown in Fig. A.1. Both circuits include a $4.7 \mu\text{F}$ capacitor (400PX4.7MEFCTA8X11.5, Rubycon), which was slowly charged up using the high-voltage power supply (Model PS375, Stanford Research Systems) before

testing began. This capacitor, which has approximately 100 times higher capacitance than the clutch, provided larger instantaneous currents during clutch activation than the power supply is capable of, and smoothed the current draw from the power supply. The maximum holding force, release, engage, and fatigue tests were conducted using the circuit in Fig. A.1a. For the majority of the fatigue tests, the high voltage was provided by a DC high voltage transformer (AG-05 Proportional Converter, EMCO). In both circuits, the photocoupler relays (TLP222G-2, Toshiba) are individually activated to control the voltage applied to each clutch plate. Each pair of relays can be controlled to put the clutch plate at high voltage, ground, or floating states. When a clutch plate changes from high voltage to ground, or vice versa, a 1 ms delay is observed between deactivating one relay and activating the other, in order to prevent shorting, which would occur if the clutch plate was connected to both high voltage and ground simultaneously. The circuit in Fig. A.1b was used to measure clutch capacitance and power consumption. A 100 k Ω shunt resistor was placed in series with the clutch, and two high-impedance voltage dividers were placed on either side to measure the voltage drop. The voltage dividers stepped the voltage down by a factor of approximately 100, to allow voltage measurement using the dSPACE control system. The current loss through the voltage dividers was on the order of microamps, and was compensated for in the current calculations.

A.2 Fatigue Testing Control

For control purposes, the control system measured motor position and clutch force at 1000 Hz, and recorded the averaged force data at peak force for inclusion in the data recording, in order to reduce data file size. The control system also commanded motor velocity to the motor controller. An iterative learning control law was implemented to compensate for break-in and changing slack in the system, and maintained a constant maximum clutch force from cycle to cycle. The commanded motor velocity V was a function of the average of the last

five commanded velocities, a proportional error term, and a damping term, according to

$$V_n = \frac{\sum V_{n-5:n-1}}{5} + k_p * (F_{des} - F_{n-1}) + k_d * (V_{n-1} - V_{n-2}) \quad (\text{A.1})$$

where F_{des} is the desired peak clutch force, k_p is the proportional gain, and k_d is the damping coefficient. In order to prevent position drift, a similar iterative learning controller was implemented to control the return stroke of the free-sliding phase, with a desired ending motor position of 0. On each cycle the clutch was allowed 400 ms to engage before loading, and 300 ms to disengage before the free-sliding phase. This resulted in a full cycle frequency of approximately 0.55 Hz. As a safety limit, the test stopped if the commanded motor velocity during the loading phase surpassed twice the nominal value, which only occurred in cases where the clutch repeatedly slipped and was unable to achieve the desired peak force on multiple consecutive cycles. The clutch was rested for various amounts of time after the test stop was triggered by multiple slips, in order to understand the effect of rest time on the ability to recover functionality. The minimum rest time was 5 seconds, and the clutch was always able to recover functionality after each rest. Cycles where the clutch maximum force was outside the range of 39-41 N were excluded, in order to prevent counting cycles during force ramp-up at the beginning of tests and after slip cycles. This strategy resulted in the exclusion of 0.1% of the total cycles.

A.3 Coefficient of Friction Testing

The coefficient of friction of the Luxprint-on-Luxprint interface was measured by stacking a known weight onto a pair of electrodes and slowly ramping lateral force by hand until a slip occurred. One electrode was held stationary on the table, and a load cell attached to the other electrode measured the force at slip. A thin sheet of rubber was placed between the stationary electrode and the table, and a separate sheet of rubber was placed between the other electrode and a flat metal plate, in order to ensure uniform load distribution. Weights

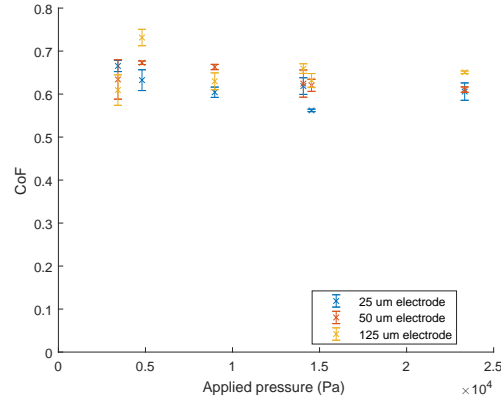


Figure A.2: Coefficient of friction testing. The coefficient of friction is constant across a range of applied pressures and electrode thicknesses.

were then stacked onto the metal plate. The coefficient of friction was determined for each trial using the equation

$$\mu = F_{slip}/F_{normal} \quad (\text{A.2})$$

where μ is the coefficient of friction, F_{slip} is the measured force at slip, and F_{normal} is the weight stacked onto the electrodes. Three pairs of electrodes, each with different electrode thickness, were tested at a range of pressures between 3 kPa and 23 kPa. The coefficient of friction was 0.63 ± 0.04 , and was constant across the whole range of applied pressures (Fig. A.2).

A.4 Custom Circuit Board Layout

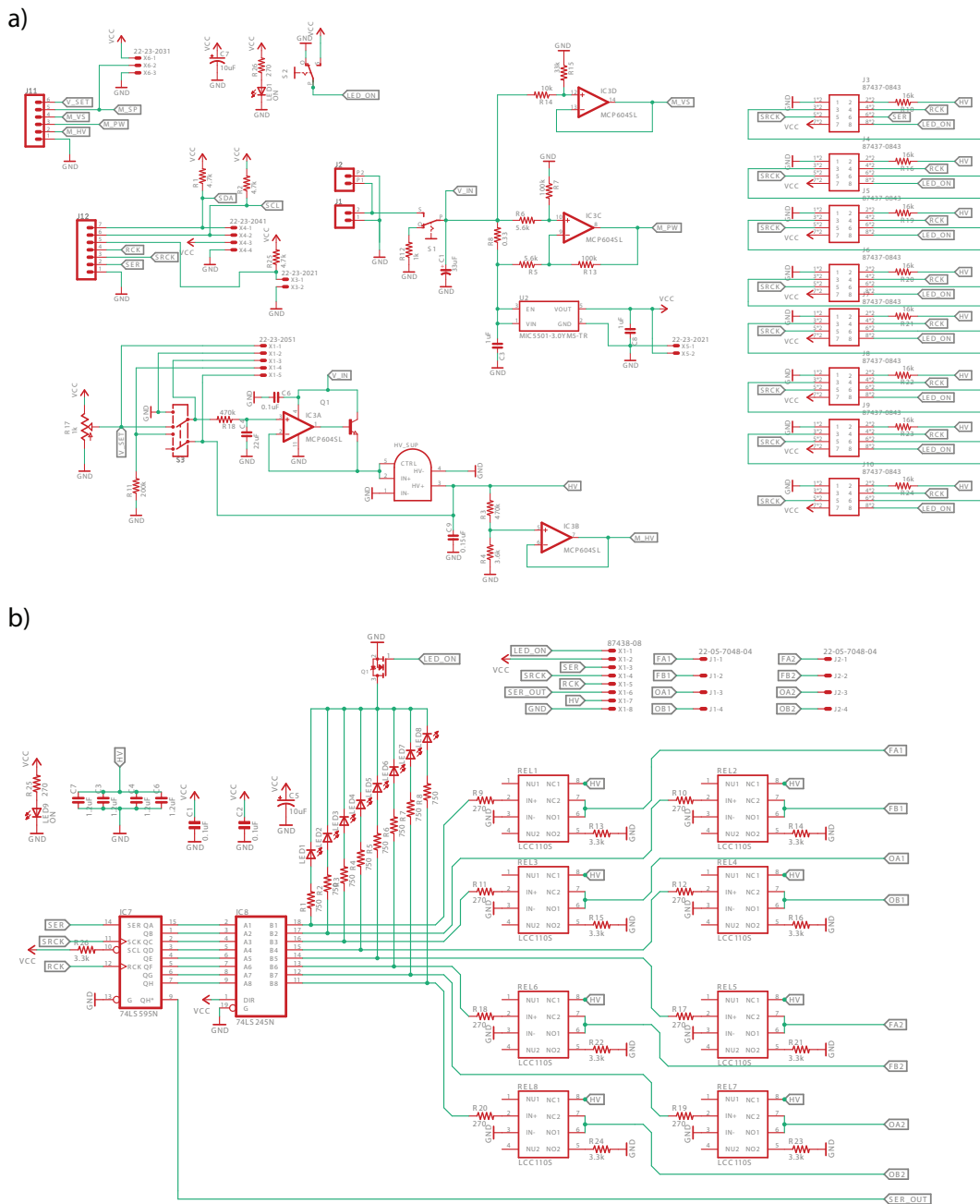


Figure A.3: Custom High Voltage Control Circuit Schematics. a) Custom Motherboard, containing the high voltage transformer and communication routing. b) Custom Daughterboard, containing shift registers, high voltage relays, and buffer capacitors. Figure Credit: Erez Krinsky

Bibliography

- [1] C. C. Kemp, A. Edsinger, and E. Torres-Jara, “Challenges for robot manipulation in human environments [grand challenges of robotics],” *IEEE Robotics & Automation Magazine*, vol. 14, no. 1, pp. 20–29, 2007.
- [2] T. Shiferaw, T. de Vries, and S. Stramigioli, “The safety of domestic robotics: A survey of various safety-related publications,” *IEEE Robotics & Automation Magazine*, vol. 21, pp. 134–142, 2014.
- [3] J. D. Madden, “Mobile robots: motor challenges and materials solutions,” *Science*, vol. 318, no. 5853, pp. 1094–1097, 2007.
- [4] S. Seok, A. Wang, M. Y. Chuah, D. Otten, J. Lang, and S. Kim, “Design principles for highly efficient quadrupeds and implementation on the mit cheetah robot,” in *Proceedings of the IEEE International Conference on Robotics and Automation (ICRA)*, 2013, pp. 3307–3312.
- [5] P. Rocco, “Stability of pid control for industrial robot arms.” *IEEE Transactions on Robotics and Automation*, vol. 12, no. 4, pp. 606–614, 1996.
- [6] S. R. Habibi and R. J. Richards, “Computed-torque and variable-structure multi-variable control of a hydraulic industrial robot,” in *Proceedings of the Institution of Mechanical Engineers, Part I: Journal of Systems and Control Engineering* 205.2, 1991, pp. 123–140.

- [7] J. Singh, B. Singh, S. P. Singh, R. Chaurasia, and S. Sachan, "Performance investigation of permanent magnet synchronous motor drive using vector controlled technique," in *In Power, Control and Embedded Systems (ICPCES), 2012 2nd International Conference on*, 2012, pp. 1–11.
- [8] A. Albu-Schaffer, S. Haddadin, C. Ott, A. Stemmer, T. Wimbock, and G. Hirzinger, "The DLR lightweight robot: design and control concepts for robots in human environments," *Industrial Robot: An International Journal*, vol. 34, no. 5, pp. 376–385, 2007.
- [9] P. Beyl, M. V. Damme, R. V. Ham, B. Vanderborght, and D. Lefeber, "Pleated pneumatic artificial muscle-based actuator system as a torque source for compliant lower limb exoskeletons," *IEEE Transactions on Mechatronics*, vol. 19, no. 3, pp. 1046–1056, 2014.
- [10] B. Verrelst, B. V. Ronald Van Ham, F. Daerden, D. Lefeber, and J. Vermeulen, "The pneumatic biped "Lucy" actuated with pleated pneumatic artificial muscles," *Autonomous Robots*, vol. 18, no. 2, pp. 201–213, 2005.
- [11] F. Daerden and D. Lefeber, "Pneumatic artificial muscles: actuators for robotics and automation," *European journal of mechanical and environmental engineering*, vol. 47, no. 1, pp. 11–21, 2002.
- [12] T. Nakamura and H. Shinohara, "Position and force control based on mathematical models of pneumatic artificial muscles reinforced by straight glass fibers," in *Proceedings of the IEEE International Conference on Robotics and Automation (ICRA)*, 2007, pp. 4361–4366.
- [13] T. Nakamura, N. Saga, and K. Yaegashi, "Development of a pneumatic artificial muscle based on biomechanical characteristics," in *IEEE International Conference on Industrial Technology*, 2003, pp. 729–734.

- [14] D. P. Ferris, J. M. Czerniecki, and B. Hannaford, "An ankle-foot orthosis powered by artificial pneumatic muscles," *Journal of applied biomechanics*, vol. 21, no. 2, pp. 189–197, 2005.
- [15] R. Kornbluh, R. Pelrine, J. Eckerle, and J. Joseph, "Electrostrictive polymer artificial muscle actuators," in *Proceedings of the IEEE International Conference on Robotics and Automation (ICRA)*, 1998, pp. 2147–2154.
- [16] S. G. Wax and R. R. Sands, "Electroactive polymer actuators and devices," *Smart Structures and Materials: Electroactive Polymer Actuators and Devices*, vol. 3669, pp. 2–11, 1999.
- [17] S. Hau, A. York, and S. Seelecke, "High-force dielectric electroactive polymer (DEAP) membrane actuator," *Electroactive Polymer Actuators and Devices*, vol. 9798, p. 97980I, 2016.
- [18] E. Acome, S. K. Mitchell, T. G. Morrissey, M. B. Emmett, C. Benjamin, M. King, M. Radakovitz, and C. Keplinger, "Hydraulically amplified self-healing electrostatic actuators with muscle-like performance," *Science*, vol. 359, no. 6371, pp. 61–65, 2018.
- [19] F. Butera, "Shape memory actuators," *Advanced Materials and Processes*, vol. 166, no. 3, pp. 37–40, 2008.
- [20] J. D. Madden, N. A. Vandesteeg, P. A. Anquetil, P. G. Madden, A. Takshi, R. Z. Pytel, S. R. Lafontaine, P. A. Wieringa, and I. W. Hunter, "Artificial muscle technology: physical principles and naval prospects," *IEEE Journal of oceanic engineering*, vol. 29, no. 3, pp. 706–728, 2004.
- [21] S. Majima, K. Kodama, and T. Hasegawa, "Modeling of shape memory alloy actuator and tracking control system with the model," *IEEE Transactions on Control Systems Technology*, vol. 9, no. 1, pp. 54–59, 2001.

- [22] Inertia-Dynamics, *Flange Mounted Brakes - Type FB*, 2017. [Online]. Available: "<http://www.idicb.com/products/electromagnetic-clutches-and-brakes/brakes/type-fb>"
- [23] Lord, *Lord TFD Steering Units*, 2017. [Online]. Available: "https://www.lord.com/sites/default/files/PB8130_TFDBrochure_2015-10-R2.pdf"
- [24] S. H. Collins, M. B. Wiggin, and G. S. Sawicki, "Reducing the energy cost of human walking using an unpowered exoskeleton," *Nature*, vol. 522, pp. 212–215, 2015.
- [25] M. S. Alkan, H. Gurocak, and B. Gonenc, "Linear magnetorheological brake with serpentine flux path as a high force and low off-state friction actuator for haptics," *Journal of Intelligent Material Systems and Structures*, vol. 24, no. 14, pp. 1699–1713, 2013.
- [26] M. Plooiij, "Lock your robot: A review of locking devices used in robotics," *IEEE Robotics & Automation Magazine*, vol. 22, no. 1, pp. 106–117, 2015.
- [27] E. Rouse, L. Mooney, and H. Herr, "Clutchable series-elastic actuator: Implications for prosthetic knee design," *International Journal of Robotics Research*, vol. 33, no. 13, pp. 1611–1625, 2014.
- [28] W.-J. Wu and P.-C. Lin, "A switchable clutched parallel elasticity actuator," in *Proceedings of the IEEE International Conference on Advanced Intelligent Mechatronics*, 2017, pp. 1173–1178.
- [29] M. Plooiij, M. van Nunspeet, M. Wisse, and H. Vallery, "Design and evaluation of the bi-directional clutched parallel elastic actuator (BIC-PEA)," in *Proceedings of the IEEE International Conference on Robotics and Automation (ICRA)*, 2015.
- [30] J. Geeroms, L. Flynn, R. Jimenez-Fabian, B. Vanderborght, and D. Lefeber., "Ankle-knee prosthesis with powered ankle and energy transfer for CYBERLEGs alpha-

- prototype.” in *Proceedings of the IEEE International Conference on Rehabilitation Robotics (ICORR)*, 2013, pp. 1–6.
- [31] G. Tonietti, R. Schiavi, and A. Bicchi, “Design and control of a variable stiffness actuator for safe and fast physical human/robot interaction,” in *Proceedings of the IEEE International Conference on Robotics and Automation (ICRA)*, 2005, pp. 526–531.
- [32] J.-J. Park, Y.-J. Lee, J.-B. Song, and H.-S. Kim, “Safe joint mechanism based on nonlinear stiffness for safe human-robot collision,” in *Proceedings of the IEEE International Conference on Robotics and Automation (ICRA)*, 2008, pp. 2177–2182.
- [33] J. Newton, J. Morton, J. Clark, and W. S. Oates, “Modeling and characterization of stiffness controlled robotic legs using dielectric elastomers,” *Electroactive Polymer Actuators and Devices*, vol. 8340, p. 83400Z, 2012.
- [34] D. F. Haufle, M. D. Taylor, S. Schmitt, and H. Geyer, “A clutched parallel elastic actuator concept: Towards energy efficient powered legs in prosthetics and robotics,” in *Proceedings of the IEEE International Conference on Biomedical Robotics and Biomechanics (BioRob)*, 2012, pp. 1614–1619.
- [35] A. S. Shafer and M. R. Kermani, “Design and validation of a magneto-rheological clutch for practical control applications in human-friendly manipulation,” in *Proceedings of the IEEE International Conference on Robotics and Automation (ICRA)*, 2011, pp. 4266–4271.
- [36] I. Choi, N. Corson, L. Peiros, E. W. Hawkes, S. Keller, and S. Follmer, “A soft, controllable, high force density linear brake utilizing layer jamming,” *IEEE Robotics and Automation Letters*, vol. 3, no. 1, pp. 450–457, 2018.
- [37] W. Shan, S. Diller, A. Tutcuoglu, and C. Majidi, “Rigidity-tuning conductive elastomer,” *Smart Materials and Structures*, vol. 24, p. 065001, 2015.

- [38] H. Prahlad, R. Pelrine, S. Stanford, J. Marlow, and R. Kornbluh, “Electroadhesive robots - wall climbing robots enabled by a novel, robust, and electrically controllable adhesion technology,” in *Proceedings of the IEEE International Conference on Robotics and Automation (ICRA)*, 2008, pp. 3028–3033.
- [39] J. Guo, K. Elgeneidy, C. Xiang, N. Lohse, L. Justham, and J. Rossiter, “Soft pneumatic grippers embedded with stretchable electroadhesion,” *Smart Materials and Structures*, vol. 27, no. 5, p. 055006, 2018.
- [40] D. Ruffatto III, J. Shah, and M. Spenko, “Increasing the adhesion force of electrostatic adhesives using optimized electrode geometry and a novel manufacturing process,” *Journal of Electrostatics*, vol. 72, pp. 147–155, 2014.
- [41] A. S. Chen and S. Bergbreiter, “A comparison of critical shear force in low-voltage, all-polymer electroadhesives to a basic friction model,” *Smart Materials and Structures*, vol. 26, no. 2, p. 025028, 2017.
- [42] D. M. Aukes, B. Heyneman, J. Ulmen, H. Stuart, M. R. Cutkosky, S. Kim, P. Garcia, and A. Edsinger, “Design and testing of a selectively compliant underactuated hand,” *International Journal of Robotics Research*, vol. 33, no. 5, pp. 721–735, 2014.
- [43] M. E. Karagozler, J. D. Campbell, G. K. Fedder, S. C. Goldstein, M. P. Weller, and B. W. Yoon, “Electrostatic latching for inter-module adhesion, power transfer, and communication in modular robots,” in *Proceedings of the IEEE/RSJ International Conference on Intelligent Robots and Systems (IROS)*, 2007, pp. 2779–2786.
- [44] S. B. Diller, S. H. Collins, and C. Majidi, “The effects of electroadhesive clutch design parameters on performance characteristics,” *Journal of Intelligent Material Systems and Structures*, vol. 29, no. 19, pp. 3804–3828, 2018.
- [45] S. H. Collins, A. Ruina, R. Tedrake, and M. Wisse, “Efficient bipedal robots based on passive-dynamic walkers,” *Science*, vol. 307, no. 5712, pp. 1082–1085, 2005.

- [46] G. Elliott, G. S. Sawicki, A. Marecki, and H. Herr, “The biomechanics and energetics of human running using an elastic knee exoskeleton,” in *Proceedings of the IEEE International Conference on Rehabilitation Robotics (ICORR)*, 2013, pp. 1–6.
- [47] G. Mathijssen, R. Furnemont, T. Verstraten, B. Brackx, J. Premec, R. Jimenez, D. Lefeber, and B. Vanderborght, “+SPEA introduction: drastic actuator energy requirement reduction by symbiosis of parallel motors, springs and locking mechanisms,” in *Proceedings of the IEEE International Conference on Robotics and Automation (ICRA)*, 2016, pp. 676–681.
- [48] A. Girard and H. H. Asada, “A practical optimal control approach for two-speed actuators,” in *Proceedings of the IEEE International Conference on Robotics and Automation (ICRA)*, 2016, pp. 4572–4577.
- [49] T. R. Hunt, C. J. Berthelette, and M. B. Popovic, “Linear one-to-many (OTM) system,” in *Proceedings of the IEEE International Conference on Technologies for Practical Robot Applications*, 2013, pp. 1–6.
- [50] E. W. Hawkes, D. L. Christensen, M. T. Pope, and M. R. Cutkosky, “One motor, two degrees of freedom through dynamic response switching,” in *Proceedings of the IEEE International Conference on Robotics and Automation (ICRA)*, 2016, pp. 969–975.
- [51] M. I. Awad, D. Gan, J. Thattamparambil, C. Stefanini, J. Dias, and L. Seneviratne, “Novel passive discrete variable stiffness joint (pDVSJ): Modeling, design, and characterization,” in *Proceedings of the IEEE International Conference on Robotics and Biomimetics (ROBIO)*, 2016, pp. 1808–1813.
- [52] C. Rossa, J. Lozada, and A. Micaelli, “Design and control of a dual unidirectional brake hybrid actuation system for haptic devices,” *IEEE Transactions on Haptics*, vol. 7, no. 4, pp. 442–453, 2014.

- [53] M. Sakaguchi, J. Furusho, and N. Takesue, "Passive force display using ER brakes and its control experiments," in *Proceedings of the IEEE International Conference on Virtual Reality*, 2001, pp. 7–12.
- [54] K. Boku and T. Nakamura, "Development of 3-DOF soft manipulator with ER fluid clutches," *Journal of Intelligent Material Systems and Structures*, vol. 21, no. 15, pp. 1563–1567, 2010.
- [55] J. Furusho, M. Sakaguchi, N. Takesue, and K. Koyanagi, "Development of ER brake and its application to passive force display," in *Proceedings of the International Conference on Electrorheological Fluids and Magnetorheological Suspensions*, 2002, pp. 57–62.
- [56] Y. Shan, M. Philen, A. Lotfi, S. Li, C. Bakis, C. D. Rahn, and K. Wang, "Variable stiffness structures utilizing fluidic flexible matrix composites," *Journal of Intelligent Material Systems and Structures*, vol. 20, no. 4, pp. 443–456, 2009.
- [57] J. Guo, T. Bamber, J. Singh, D. Manby, P. A. Bingham, L. Justham, J. Petzing, J. Penders, and M. Jackson, "Experimental study of a flexible and environmentally stable electroadhesive device," *Applied Physics Letters*, vol. 111, no. 25, p. 251603, 2017.
- [58] Y. Kakinuma, T. Aoyama, and H. Anzai, "Development of high-performance ERG based on the principle of electro-adhesive effect," *Journal of Intelligent Material Systems and Structures*, vol. 21, no. 15, pp. 1501–1508, 2010.
- [59] T. F. Dupont, *Mylar Polyester Film Product Information*, 2017. [Online]. Available: "http://usa.dupontteijinfilms.com/wp-content/uploads/2017/01/Mylar_Physical_Properties.pdf"
- [60] F. Tian, Q. Lei, X. Wang, and Y. Wang, "Effect of deep trapping states on space charge suppression in polyethylene/ZnO nanocomposite," *Applied Physics Letters*, vol. 99, no. 14, p. 142903, 2011.

- [61] A. M. Pourrahimi, R. T. Olsson, and M. S. Hedenqvist, "The role of interfaces in polyethylene/metal-oxide nanocomposites for ultrahigh-voltage insulating materials," *Advanced Materials*, vol. 30, no. 4, p. 1703624, 2018.
- [62] M. D. Bartlett, A. B. Croll, D. R. King, B. M. Paret, D. J. Irschick, and A. J. Crosby, "Looking beyond fibrillar features to scale gecko-like adhesion," *Advanced Materials*, vol. 24, no. 8, pp. 1078–1083, 2012.
- [63] M. D. Bartlett and A. J. Crosby, "Scaling normal adhesion force capacity with a generalized parameter," *Langmuir*, vol. 29, no. 35, pp. 11 022–11 027, 2013.
- [64] SEPAC, *RFTC Series Rotating Field Tooth Clutch*, 2017. [Online]. Available: "<https://sepac.com/products/view/rotating-field-tooth-clutch/#>"
- [65] R. Van Ham, T. G. Sugar, B. Vanderborght, K. W. Hollander, and D. Lefeber, "Compliant actuator designs," *IEEE Robotics & Automation Magazine*, vol. 16, no. 3, pp. 81–94, 2009.
- [66] S. Diller, C. Majidi, and S. Collins, "A lightweight, low-power electroadhesive clutch and spring for exoskeleton actuation," in *Proceedings of the IEEE International Conference on Robotics and Automation (ICRA)*, 2016, pp. 682–689.
- [67] B. Vanderborght, A. Albu-Schaffer, A. Bicchi, E. Burdet, D. G. Caldwell, R. Carloni, M. G. Catalano, O. Eiberger, W. Friedl, G. Ganesh, and M. Garabini, "Variable impedance actuators: A review," *Robotics and Autonomous Systems*, vol. 61, no. 12, pp. 1601–1614, 2013.
- [68] D. Leach, F. Gunther, N. Maheshwari, and F. Iida, "Linear multimodal actuation through discrete coupling," *IEEE Transactions on Mechatronics*, vol. 19, no. 3, pp. 827–839, 2014.

- [69] M. Plooij, W. Wolfslag, and M. Wisse, “Clutched elastic actuators,” *IEEE Transactions on Mechatronics*, vol. 22, no. 2, pp. 739–750, 2017.
- [70] A. Ramezani, J. W. Hurst, K. A. Hamed, and J. W. Grizzle, “Performance analysis and feedback control of ATRIAS, a three-dimensional bipedal robot,” *Journal of Dynamic Systems, Measurement, and Control*, vol. 136, no. 2, p. 021012, 2014.
- [71] C. Hubicki, J. Grimes, M. Jones, D. Renjewski, A. Sprowitz, A. Abate, and J. Hurst, “ATRIAS: Design and validation of a tether-free 3D-capable spring-mass bipedal robot,” *International Journal of Robotics Research*, vol. 35, no. 12, pp. 1497 – 1521, 2016.
- [72] M. Johnson, M. Johnson, B. Shrewsbury, S. Bertrand, T. Wu, D. Duran, M. Floyd, P. Abeles, D. Stephen, N. Mertins, A. Lesman, and J. Carff, “Team IHMC’s lessons learned from the DARPA Robotics Challenge trials,” *Journal of Field Robotics*, vol. 32, no. 2, pp. 192–208, 2015.
- [73] T. McGeer, “Passive dynamic walking,” *International Journal of Robotics Research*, vol. 9, no. 2, pp. 62–82, 1990.
- [74] S. Seok, A. Wang, D. Otten, and S. Kim, “Actuator design for high force proprioceptive control in fast legged locomotion,” in *Proceedings of the IEEE/RSJ International Conference on Intelligent Robots and Systems (IROS)*, 2012, pp. 1970–1975.
- [75] T. Koolen, S. Bertrand, G. Thomas, T. D. Boer, T. Wu, J. Smith, J. Engelsberger, and J. Pratt, “Design of a momentum-based control framework and application to the humanoid robot Atlas,” *International Journal of Humanoid Robotics*, vol. 13, no. 1, p. 1650007, 2016.
- [76] A. Mazumdar, S. J. Spencer, C. Hobart, J. Salton, M. Quigley, T. Wu, S. Bertrand, J. Pratt, and S. P. Buerger, “Parallel elastic elements improve energy efficiency on the

- STEPPR bipedal walking robot,” *IEEE Transactions on Mechatronics*, vol. 22, no. 2, pp. 898–908, 2017.
- [77] W. van Dijk and H. Van der Kooij, “XPED2: A passive exoskeleton with artificial tendons,” *IEEE Robotics & Automation Magazine*, vol. 21, no. 4, pp. 56–61, 2014.
- [78] M. Cestari, D. Sanz-Merodio, J. C. Arevalo, and E. Garcia, “ARES, a variable stiffness actuator with embedded force sensor for the ATLAS exoskeleton,” *Industrial Robot: An International Journal*, vol. 41, no. 6, pp. 518–526, 2014.
- [79] G. A. Pratt and M. M. Williamson, “Series elastic actuators,” in *Proceedings of the IEEE/RSJ International Conference on Intelligent Robots and Systems (IROS)*, 1995, pp. 399–406.
- [80] J. Zhang and S. H. Collins, “The passive series stiffness that optimizes torque tracking for a lower-limb exoskeleton in human walking,” *Frontiers in Neurorobotics*, vol. 11, p. 68, 2017.
- [81] R. C. Browning, J. R. Modica, R. Kram, and A. Goswami, “The effects of adding mass to the legs on the energetics and biomechanics of walking,” *Medicine & Science in Sports & Exercise*, vol. 39, no. 3, pp. 515–525, 2007.
- [82] C. J. Walsh, K. Endo, and H. Herr, “A quasi-passive leg exoskeleton for load-carrying augmentation,” *International Journal of Humanoid Robotics*, vol. 4, no. 3, pp. 487–506, 2007.
- [83] T. Yakimovich, E. D. Lemaire, and J. Kofman, “Engineering design review of stance-control knee-ankle-foot orthoses,” *Journal of Rehabilitation Research and Development*, vol. 46, no. 2, pp. 257–267, 2009.

- [84] J. A. Blaya and H. Herr, "Adaptive control of a variable-impedance ankle-foot orthosis to assist drop-foot gait," *IEEE Transactions on Neural Systems and Rehabilitation Engineering*, vol. 12, no. 1, pp. 24–31, 2004.
- [85] M. K. Shepherd and E. J. Rouse, "The VSPA foot: A quasi-passive ankle-foot prosthesis with continuously variable stiffness," *IEEE Transactions on Neural Systems and Rehabilitation Engineering*, vol. 25, no. 12, pp. 2375–2386, 2017.
- [86] T. Lenzi, M. Cempini, L. J. Hargrove, and T. A. Kuiken, "Actively variable transmission for robotic knee prostheses," in *Proceedings of the IEEE International Conference on Robotics and Automation (ICRA)*, 2017, pp. 6665–6671.
- [87] M. Kim and S. H. Collins, "Step-to-step ankle inversion/eversion torque modulation can reduce effort associated with balance," *Frontiers in Neurobotics*, vol. 11, p. 62, 2017.
- [88] P. Stegall, D. Zanotto, and S. K. Agrawal, "Variable damping force tunnel for gait training using ALEX III," *IEEE Robotics & Automation Magazine*, vol. 2, no. 3, pp. 1495–1501, 2017.
- [89] R. Unal, S. M. Behrens, R. Carloni, E. E. G. Hekman, S. Stramigioli, and H. F. J. M. Koopman, "Prototype design and realization of an innovative energy efficient transfemoral prosthesis," in *Proceedings of the IEEE International Conference on Biomedical Robotics and Biomechatronics (BioRob)*, 2010, pp. 191–196.
- [90] A. D. Segal, K. E. Zelik, G. K. Klute, D. C. Morgenroth, M. E. Hahn, M. S. Orendurff, P. G. Adamczyk, S. H. Collins, A. D. Kuo, and J. M. Czerniecki, "The effects of a controlled energy storage and return prototype prosthetic foot on transtibial amputee ambulation," *Human Movement Science*, vol. 31, no. 4, pp. 918–931, 2012.
- [91] P. Cherelle, V. Grosu, L. Flynn, K. Junius, M. Moltedo, B. Vanderborght, and D. Lefeber, "The ankle mimicking prosthetic foot 3 - locking mechanisms, actuator

- design, control and experiments with an amputee,” *Robotics and Autonomous Systems*, vol. 91, pp. 327 – 336, 2017.
- [92] J. M. Donelan, Q. Li, V. Naing, J. A. Hoffer, D. J. Weber, and A. D. Kuo, “Biomechanical energy harvesting: Generating electricity during walking with minimal user effort,” *Science*, vol. 319, no. 5864, pp. 807–810, 2008.
- [93] N. Lauzier and C. Gosselin, “Series clutch actuators for safe physical human-robot interaction,” in *Proceedings of the IEEE International Conference on Robotics and Automation (ICRA)*, 2011, pp. 5401–5406.
- [94] J. R. Koller, D. H. Gates, D. P. Ferris, and C. D. Remy, “‘Body-in-the-loop’ optimization of assistive robotic devices: A validation study,” in *Proceedings of the Robotics: Science and Systems Conference*, 2016.
- [95] J. Zhang, P. Fiers, K. A. Witte, R. W. Jackson, K. L. Poggensee, C. G. Atkeson, and S. H. Collins, “Human-in-the-loop optimization of exoskeleton assistance during walking,” *Science*, vol. 356, no. 6344, pp. 1280–1284, 2017.
- [96] Y. Ding, M. Kim, S. Kuindersma, and C. J. Walsh, “Human-in-the-loop optimization of hip assistance with a soft exosuit during walking,” *Science Robotics*, vol. 3, no. 15, p. 10.1126, 2018.
- [97] N. Ulrich and V. Kumar, “Passive mechanical gravity compensation for robot manipulators,” in *Proceedings of the IEEE International Conference on Robotics and Automation (ICRA)*, 1991, pp. 1536–1541.
- [98] M. Vermeulen and M. Wisse, “Intrinsically safe robot arm: Adjustable static balancing and low power actuation,” *International Journal of Social Robotics*, vol. 2, no. 3, pp. 275–288, 2010.

- [99] J. L. Herder, “Energy-free systems: Theory, conception and design of statically balanced spring mechanisms,” Ph.D. dissertation, 2001.
- [100] T. Morita, F. Kuribara, Y. Shiozawa, and S. Sugano, “A novel mechanism design for gravity compensation in three dimensional space,” in *Proceedings of the IEEE International Conference on Advanced Intelligent Mechatronics*, 2003, pp. 163–168.
- [101] G. Endo, H. Yamada, A. Yajima, M. Ogata, and S. Hirose, “A passive weight compensation mechanism with a non-circular pulley and a spring,” in *Proceedings of the IEEE International Conference on Robotics and Automation (ICRA)*, 2010, pp. 3843–3848.
- [102] V. I. Babitsky and A. Shipilov, *Resonant robotic systems*. Berlin, Germany: Springer Science & Business Media, 2012.
- [103] H. Kang, H. Shim, B.-H. Jun, and P.-M. Lee, “Development of leg with arm for the multi-legged seabed robot “CR200”,” in *Oceans*, 2012, pp. 1–4.
- [104] B. Chen, H. Ma, L.-Y. Qin, F. Gao, K.-M. Chan, S.-W. Law, L. Qin, and W.-H. Liao, “Recent developments and challenges of lower extremity exoskeletons,” *Journal of Orthopaedic Translation*, vol. 5, pp. 26–37, 2016.
- [105] K. A. Witte, J. Zhang, R. W. Jackson, and S. H. Collins, “Design of two lightweight, high-bandwidth torque-controlled ankle exoskeletons,” in *Proceedings of the IEEE International Conference on Robotics and Automation (ICRA)*, 2015, pp. 1223–1228.
- [106] B. Quinlivan, S. Lee, P. Malcolm, D. Rossi, M. Grimmer, C. Siviyy, N. Karavas, D. Wagner, A. Asbeck, I. Galiana, and C. Walsh, “Assistance magnitude versus metabolic cost reductions for a tethered multiarticular soft exosuit,” *Science Robotics*, vol. 2, no. 2, 2017.

- [107] J. Zhang, C. C. Cheah, and S. H. Collins, “Experimental comparison of torque control methods on an ankle exoskeleton during human walking,” in *Proceedings of the IEEE International Conference on Robotics and Automation (ICRA)*, 2015, pp. 5584–5589.
- [108] R. W. Jackson and S. H. Collins, “An experimental comparison of the relative benefits of work and torque assistance in ankle exoskeletons,” *Journal of Applied Physiology*, vol. 5, pp. 541–557, 2015.
- [109] P. Malcolm, W. Derave, S. Galle, and D. D. Clercq, “A simple exoskeleton that assists plantarflexion can reduce the metabolic cost of human walking,” *PloS one*, vol. 8, no. 2, 2013.
- [110] L. M. Mooney, E. J. Rouse, and H. M. Herr, “Autonomous exoskeleton reduces metabolic cost of human walking during load carriage,” *Journal of neuroengineering and rehabilitation*, vol. 11, no. 1, p. 80, 2014.
- [111] F. A. Panizzolo, I. Galiana, A. T. Asbeck, C. Siviyy, K. Schmidt, K. G. Holt, and C. J. Walsh, “A biologically-inspired multi-joint soft exosuit that can reduce the energy cost of loaded walking,” *Journal of neuroengineering and rehabilitation*, vol. 13, no. 1, p. 43, 2016.
- [112] A. Balasubramanian, M. Standish, and C. J. Bettinger, “Microfluidic thermally activated materials for rapid control of macroscopic compliance,” *Advanced Functional Materials*, vol. 24, pp. 4860–4866, 2014.
- [113] C. S. Haines, M. Lima, N. Li, G. Spinks, J. Foroughi, J. Madden, S. H. Kim, S. Fang, M. J. de Andrade, F. Goktepe, O. Goktepe, S. Mirvakili, S. Naficy, X. Lepro, J. Oh, M. Kozlov, S. J. Kim, X. Xu, B. Swedlove, G. Wallace, and R. Baughman, “Artificial muscles from fishing line and sewing thread,” *Science*, vol. 343, pp. 868–872, 2014.

- [114] A. Jafari, N. Tsagarakis, B. Vanderborght, and D. Caldwell, “A novel actuator with adjustable stiffness (AwAS),” in *Proceedings of the IEEE / RSJ International Conference on Intelligent Robots and Systems (IROS)*, 2010, pp. 4201–4206.
- [115] G. Mathijssen, D. Lefeber, and B. Vanderborght, “Variable recruitment of parallel elastic elements: Series-parallel elastic actuators (SPEA) with dephased mutilated gears,” *IEEE Transactions on Mechatronics*, vol. 20, pp. 594–602, 2015.
- [116] R. D. Kornbluh, R. Pelrine, H. Prahlah, A. Wong-Foy, B. McCoy, S. Kim, J. Eckerle, and T. Low, “From boots to buoys: promises and challenges of dielectric elastomer energy harvesting,” *Electroactivity in Polymeric Materials*, Springer, pp. 67–93, 2012.
- [117] S. H. Collins and A. D. Kuo, “Recycling energy to restore impaired ankle function during human walking,” *PLoS one*, vol. 5, no. 2, p. e9307, 2010.
- [118] J. A. Lozano, P. Larrañaga, I. Inza, and E. Bengoetxea, *Towards a new evolutionary computation: advances on estimation of distribution algorithms*. Springer, 2006, vol. 192.
- [119] A. Atalay, V. Sanchez, O. Atalay, D. M. Vogt, F. Haufe, R. J. Wood, and C. J. Walsh, “Batch fabrication of customizable silicone-textile composite capacitive strain sensors for human motion tracking,” *Advanced Materials Technologies*, vol. 2, no. 9, p. 1700136, 2017.
- [120] T. Kikuchi, K. Otsuki, J. Furusho, H. Abe, J. Noma, M. Naito, and N. Lauzier, “Development of a compact magnetorheological fluid clutch for human-friendly actuator,” *Advanced Robotics*, vol. 24, no. 10, pp. 1489–1502, 2010.
- [121] O. Baser, M. A. Demiray, A. Bas, E. Kilic, and G. O. Erol, “A linear magnetorheological brake with multipole outer coil structure for high on-state and low off-state force outputs,” *Turkish Journal of Electrical Engineering and Computer Sciences*, vol. 25, no. 5, pp. 3501–3514, 2017.

- [122] Ogura-Industrial-Corp., *OPB-N Electromagnetic Mag-Particle Brake*, 2017. [Online]. Available: "<http://ogura-clutch.com/products.php?category=2&product=88>"
- [123] —, *VBEH / VBSH EM Brake (high torque design)*, 2017. [Online]. Available: "<http://ogura-clutch.com/download.php?item=77&type=1>"